FIRST PRINCIPLES CALCULATIONS ON DIVERSE PROPERTIES OF SOME PEROVSKITE COMPOUNDS

Thesis Submitted for the Award of the Degree of

DOCTOR OF PHILOSOPHY

in

Physics

By

Preeti Kumari

Registration Number: 11900895

Supervised By

Dr. Vipul Srivastava (UID: 23642)

Department of Physics (Professor)

Lovely Professional University, Phagwara,

Punjab, India

LOVELY PROFESSIONAL UNIVERSITY, PUNJAB

2023

DECLARATION

I, hereby declared that the presented work in the thesis entitled "**First principles calculations on diverse properties of some Perovskite compounds**" in fulfilment of degree of **Doctor of Philosophy (Ph. D.)** is outcome of research work carried out by me under the supervision Dr. Vipul Srivastava, working as Professor, in the Department of Physics, School of Chemical Engineering and Physical Sciences of Lovely Professional University, Punjab, India. In keeping with general practice of reporting scientific observations, due acknowledgements have been made whenever work described here has been based on findings of other investigator. This work has not been submitted in part or full to any other University or Institute for the award of any degree.

(Signature of Scholar)

Preeti Kumari

11900895

Department of Physics

School of Chemical Engineering and Physical Sciences

Lovely Professional University,

Punjab, India

CERTIFICATE

This is to certify that the work reported in the Ph. D. thesis entitled **"First principles calculations on diverse properties of some Perovskite compounds**" submitted in fulfillment of the requirement for the reward of degree of **Doctor of Philosophy (Ph.D.)** in the Department of Physics, School of Chemical Engineering and Physical Sciences, is a research work carried out by Preeti Kumari, 11900895, is bonafide record of his/her original work carried out under my supervision and that no part of thesis has been submitted for any other degree, diploma or equivalent course.

(Signature of Supervisor)

Dr. Vipul Srivastava
Professor
Department of Physics,
School of Chemical Engineering and Physical Sciences
Lovely Professional University,
Punjab, India

ABSTRACT

The precise qualities of the materials utilized have a decisive impact on the functionality of every modern technical object. Challenges for basic research in terms of comprehending current materials and creating new ones arise from novel materials based on metals, semiconductors, composites, or nanostructures. Hence, the core of our research is the examination of the special material known as perovskite. With the advancement of our study, several previously unknown unique qualities are being uncovered. As a result, a fundamental understanding of all of these materials is critical not only for exploring novel physics but also for developing innovative materials with varied functionality. Many useful features of these materials include ferromagnetism, colossal magnetoresistance, ferroelectricity, magnetic, optical, electronics, thermoelectric, and many others. These characteristics also have innovative applications because they can be influenced by outside factors like electric field, magnetic field, temperature, pressure, etc. These remarkable qualities lead to a variety of uses for these well-known compounds, including solar cells, memory systems, sensors, magnetic detectors, photovoltaic devices, UV absorbers, spintronics, and spin valve generators. The current study examines various properties of three series of perovskite materials. The first series is based on cerium-based oxide perovskites which include $MgCeO_3$, $SrCeO_3$, $CaCeO_3$, and $BaCeO_3$, and the second one is based on rare earth ferrites, $RFeO_3$ (R = Pr and Nd) and finally, third one is based on rubidium tin-based halide perovskites, $RbSnF_3$, $RbSnCl_3$, $RbSnBr_3$, and $RbSnI_3$. We utilized density functional theory (DFT) and Full potential LAPW to calculate properties like elastic, mechanical, thermophysical, and transport, and WIEN2K is the software program utilized for these calculations. Investigated perovskite structures are crystallized in their cubic phase Pm-3m (221). The compounds' stability is maintained by optimizing the structure under volume compression ranging from -15 to +15% utilizing the exchange-correlation potential; generalized gradient approximation. (GGA), is available in three forms: GGA-PBEsol, GGA-WC, and GGA-PBE. Fabrication of these compounds in the industry is

estimated by calculating formation as well as cohesive energies. Cohesive energy with a negative value ensures the production of these compounds. Together with the GGA, mBJ is used for understanding of electrical behavior of materials. So, for an understanding of electronic characteristics, we have assessed the band structure as well as DOS. Under mBJ, $RFeO_3$ (R = Nd and Pr) exhibited half-metallic behavior in which spin-up channels have shown metallic while spin down has shown semiconducting nature, while $MgCeO_3$, $CaCeO_3$, $SrCeO_3$, $BaCeO_3$ and $RbSnI_3$, $RbSnBr_3$, $RbSnCl_3$, $RbSnF_3$ displayed semiconducting nature. Compounds are optimized structurally in both nonmagnetic (NM) and ferromagnetic phases (FM) to determine whether they are magnetic or not. The cerium-based oxide perovskites and the Rb-Sn-based halide perovskites have demonstrated their stability in the nonmagnetic phase, whereas rare earth ferrites have demonstrated their stability in the spin-polarized phase. Magnetic moments in $RFeO_3$ (R = Nd and Pr) are integral multiples of Bohr magneton. $NdFeO_3$ and $PrFeO_3$ are half-metallic ferromagnets because their two spins exhibit different behaviors. So, total spin polarization is demonstrated by $RFeO_3$ at fermi level.

The materials are moreover subjected to applied force stress to comprehend their mechanical stability. Three different kinds of stress are used to analyze the cubic phase of our compounds and come up with three elastic constants. The IR elast package/Thomas Charpin method is used to perform this calculation. The acquired value of elastic parameters is computed for calculating parameters, including Young's, Shear, Bulk modulus, Poison ratio, Debye temperature, melting temperature, Cauchy pressure, Pugh ratio, and anisotropy. The Pugh's ratio and Cauchy pressure determine whether a compound is brittle or ductile. The compounds under investigation met the requirements for mechanical stability by exhibiting ductile and anisotropic behavior.

Also, we evaluated the thermodynamic properties and demonstrated how they changed as temperature increased while keeping the pressure constant, and vice versa. The relevant thermodynamical parameters including Thermal Expansion Coefficient, Entropy, Specific Heat, Grüneisen Constant, Bulk Modulus, Volume, Debye Temperature are assessed through the QHD model, which is integrated into the

Gibbs2 code. Their thermodynamical stability was assured by all the investigated materials.

Additionally, to assess the potential of the examined compounds for thermoelectric applications, we calculate the thermoelectric characteristics of $MgCeO_3$, $SrCeO_3$, $CaCeO_3$, $BaCeO_3$, $PrFeO_3$, $NdFeO_3$, $RbSnF_3$, $RbSnCl_3$, $RbSnBr_3$, and $RbSnI_3$. Thermoelectric materials have shown their usage in cooling car seats, mobile refrigerators, medical instruments, temperature regulators in lasers, space applications, oil pipelines, and vehicle waste heat recovery. Thermoelectric (TE) technology is premised on transforming waste heat into electric power, which is the idea behind a thermoelectric generator (TEG). A key parameter in estimating the good thermoelectric values for its usage in TEGs is thermoelectric efficiency also called figure of merit (*ZT*). This parameter is depending upon different factors like Seebeck coefficient, and electrical and thermal conductivity. For practical application, its value should be equivalent to or more than unity. Accordingly, we employed the Boltz Trap program, which is focused on the Semiclassical Boltzmann Transport phenomenon, to assess the TE coefficients of these compounds. Thermal conductivity consists of electronic as well as lattice thermal conductivity. The electronic thermal and electrical conductivity, power factor, and Seebeck coefficient, are among the parameters that the Boltz Trap code evaluates. Using the Grüneisen constant and the Debye temperature, the slack technique is used to evaluate the lattice's thermal conductivity. Thermoelectric coefficient's variation corresponding to temperature and chemical potential are also presented within the thesis. The obtained *ZT* for the investigated compounds: Ce-based compound and Rb-Sn-based perovskite are 0.64 ($MgCeO_3$), (0.66) $CaCeO_3$, 0.69 ($SrCeO_3$), 0.7 ($BaCeO_3$), 0.62 ($RbSnCl_3$), 0.60 ($RbSnBr_3$), and 0.77 ($RbSnI_3$) at 1200 K and have shown their thermoelectric efficiency upsurges with temperature. The highest *ZT* values for $PrFeO_3$, $NdFeO_3$, and $RbSnF_3$ equivalent to 0.38 (at 1200 K), 0.05 (at 1200 K), and 0.26 (at 1100 K), respectively, are extremely low and the highest *ZT* value for $RbSnF_3$ is not even at the highest temperature. Ce-based and Rb-Sn-based perovskite have shown a higher value of *ZT* which suggests their capability to be used in thermoelectric power generators. Rare earth ferrites $RFeO_3$ compounds showing half-metallic behavior are capable of application in spintronic devices and spin valve generators. The experimentalist

employs the information obtained throughout our research activity depending on the features of the devices and their intended usage.

ACKNOWLEDGEMENTS

I would like to acknowledge my earnest gratitude to all those persons without their guidance, help, and direction this task could not have been accomplished.

First and foremost, it is delighting me great pleasure to express my heartfelt and profound sense of gratitude to my supervisor Dr. Vipul Srivastava, Professor, Department of Physics, Lovely Professional University, Punjab, India. His valuable efforts, supervision, encouragement, vibrant energy, and dedication toward his work as well as toward his students inspired me throughout my Ph.D. work. I am thankful to Dr. Loviraj Gupta, Pro-vice Chancellor of Lovely Professional University for carrying out my research work. I would like to thank Dr. Kailash Chand Juglan, Head of School, School of Chemical Engineering and Physical Sciences, Dr. Nitin Tondon, Head of Research Department and Dr. Rekha, Head of RDEC for providing me necessary facilities at Lovely Professional University to continue my work. I appreciate Dr. Mukesh Kumar, Dr. Ajit Kumar Srivastava, Dr. Neha, Dr. Naveen Gupta and CDRP members serving as jury members for my end-of-term presentations.

I thanked Dr. Ramesh Sharma, Assistant Professor, Department of Applied Science, Feroze Gandhi Institute of Engineering and Technology, Raebareli, Uttar Pradesh, India for his continuous and endless support and guidance to pursue the current research work. I would like to express my deep sense of gratitude towards Dr. Sajad Ahmad Dar for his constant guidance and support during the research work.

I express my sincere thankfulness to my friend and colleague Navdeep Kaur to be presented every time for her support, guidance, and encouragement with her helping hands, throughout my research work. I would like to thank my friends Navneet Kaur and Pavas Sehgal for their support and help.

I express my thanks to Lovely Professional University for admitting me for pursuing my Ph.D. I owe my sincere thanks to all my family members, especially my mother Premlata, father Kailash Chand, sister Sonia and brother Manoj whose constant support motivated me at every moment of my life. My special thanks go to my fiancé Ritesh Mehta for his unconditional love and support to reach this milestone. Finally,

thanks to all those who directly or indirectly helped me during the tenure of my research work.

TABLE OF CONTENTS

LIST OF TABLES

LIST OF FIGURES

CHAPTER 1

INTRODUCTION

1.1 INTRODUCTION

Combating climate change and global warming is the biggest challenge facing the entire world. For the past, many decades' energy is driven by the burning of fossil fuels like natural gases, oil, and coal which are at their depleting stage. 65% of the whole world including India generates energy from fossil fuels. It was predicted that the share from fossil fuels will be increased to 80% even in 2035 [1]. These non-renewable sources of energy contribute to the power sector, transportation sector, and industrial sector. Fossil fuel combustion causes the release of hazardous gases into the atmosphere. This ultimately traps heat in the atmosphere, raising the Earth's temperature i.e., Global warming. Global warming leads to one more phenomenon i.e., Climate change which results in changing the weather patterns and increasing the sea level across the planet due to the melting of ice of the glaciers. To subside carbon emissions and climate change, UNFCCC's conference of parties has established certain goals. Their target is to cut carbon emissions to 7.6% every year from 2020 to 2030. In this regard, we should look into a new approach for the generation of new kinds of energy resources. A sustainable approach has to be followed to abate these climatic issues.

Renewable energies such as geothermal, tidal, solar, wind, biofuel, and hydro energy are the best option. Over the past ten years, the market for solar and wind energy has spiked more than 20 times. Simultaneously, harvesting green energy presents several difficulties, including location, season, and environmental factors.

Many successes in this field have been demonstrated by material physics. The most needed ones are novel materials that exhibit remarkable behavior and several functions. Perovskites, with their amazing properties, have demonstrated multiple uses in the realm of renewable energy through the solar cell, thermoelectric, and spintronic devices [2-4].

1.2 OVERVIEW OF PEROVSKITES

Perovskite compounds are well-known by researchers all around the globe due to their characteristics of multifunctional properties. These properties include magnetocaloric, colossal magnetoresistance, ferromagnetic, optical, electronic, thermoelectric, etc. [5-8]. With growing numbers of applications, the complete scrutiny of these compounds is necessary. The Perovskite journey began in 1839 when mineralogist Gustav rose found calcium titanate ($CaTiO_3$) in the Ural Mountains and decided to give the name Perovskite, in the honor of Levi Perovski, to similar kinds of structures. In 1920 perovskites were the subject of ground-breaking research by Goldschmidt et al. [9], which aided in the investigation of the minerals. The compounds with general formula "ABX_3" are recognized as "Perovskite" having A & B, different-sized cations & X is either a halide or oxide and B occupies the corner position; A occupies the center position and X occupies the edges of the unit cell. The mineral perovskite, $CaTiO_3$ was the first to contain an atomic configuration of this kind. Perovskite structural arrangement is provided in *Figure 1.1*. In perovskites structure, A is coordinated with 12 oxygen atoms while B is coordinated with 6 oxygen atoms making octahedra at eight corners of the unit cell as shown in figure.

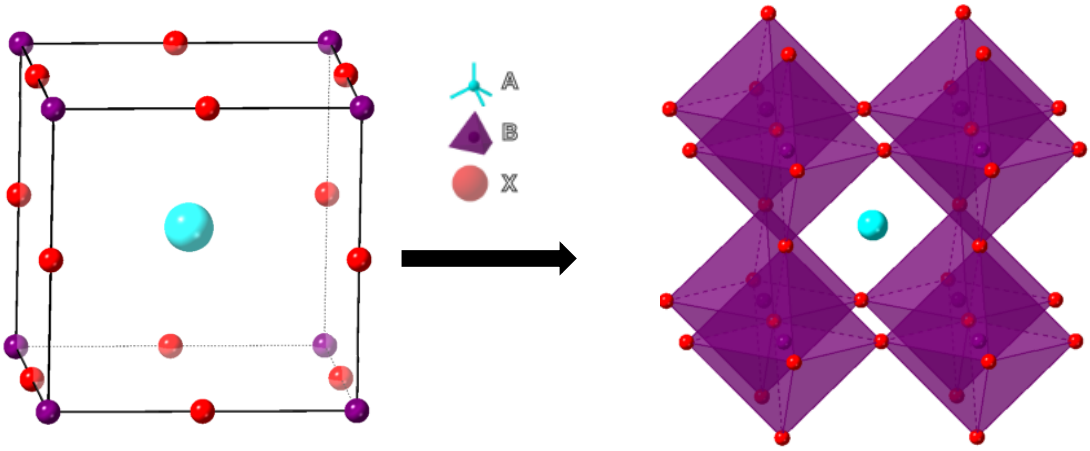

Figure 1.1: Crystal structure of perovskite and octahedral form of perovskite

1.3 TYPES OF PEROVSKTES

Due to their flexibility and ability to inculcate all atoms from the periodic table, numerous perovskite structures can be formed. Types of perovskites are as follows:

Oxide Perovskite: These are the perovskite with the general formula ABO_3. These compounds maintain neutrality by having combined valency of A and B equivalent to 6. Oxide perovskite is further divided into ternary oxide ABO_3 type ($SrTiO_3$, $BaTiO_3$, etc.) where A is having higher radius than that of B and newer complex type $ABxB'_{1-x}O_3$ ($Ba_{0.67}Nd_{0.33}WO_3$, etc.) in which B and B' are elements (not identical) having different oxidation states [9, 10]. There is numerous oxide structure linked to perovskite-based homologous series [11]. Few among those are Ruddlesden popper [12], Dion Jacobson [13], and Aurivillius [14] series. Ternary oxide perovskite is further divided into $A^{2+}B^{4+}O_3$ ($SrCeO_3$, $CaTiO_3$, $BaTiO_3$, etc.), $A^{1+}B^{5+}O_3$ ($KNbO_3$, $CsIO_3$, $AgTaO_3$, etc.), $A^{3+}B^{3+}O_3$ ($LaFeO_3$, $BiMnO_3$, $PrFeO_3$, $NdFeO_3$, etc.) and oxygen cation deficient phase ($CaMnO_{3-z}$, $SiTiO_{3-z}$, etc.).

Halide Perovskite: These perovskites are neutral compounds ABX_3, where X is a univalent anion i.e., chloride, bromide, fluoride ions, etc., and A and B have a combined valency of three. Apart from ABX_3 perovskite structures are found in other forms also such as double perovskite $A_2BB'X_6$, triple perovskite $A_2A'B_2B'X_9$, and layered perovskite A_2BX_4 [15-17].

Here, explaining some special oxide perovskite such as Transition metal oxides (TMOs) and Rare-earth ferrites ($RFeO_3$).

***Transition Metal Oxides*:** TMOs exhibit a variety of shapes and characteristics, making them one of the most intriguing types of materials [18-20]. Bonding between metal and oxygen varies from almost ionic to extremely covalent or metallic. The peculiar character of the outer d-electrons accounts for the strange behavior of TMOs. Varsity in the behavior can be seen from the compound like $LaNiO_3$ showing metallic behavior to compounds like $BaTiO_3$ showing highly insulating characteristics. Moreover, several TMOs such as $La_{1-x}Sr_xVO_3$ can move between these two phases with a change in temperature, pressure, or composition. We have oxides with a diverse range of magnetic properties from ferromagnetism to anti-ferromagnetism. This unique behavior is caused by the overlap of the oxygen atom's *p* orbital and the transition element's *d* orbital. Resultingly, we have a lower bandgap from 1 to 2 eV rather than 5 to 15 eV as found in most metals. The electronic correlation effect also comes into account due to smaller electronic bandgaps. Oxygen polarizability also

affects and takes the O^{1-} state instead of the normal O^{2-} oxidation state. These compounds prefer to be in the $d^{n+1}p^5$ system than in the normal d^np^6 state.

Rare-earth Ferrites ($RFeO_3$): Rare-earth ferrites come under $A^{3+}B^{3+}O_3$ type oxide perovskite. These perovskites are known for their interesting electrical and magnetic properties [21, 22]. Alloys of dysprosium, neodymium, lanthanum, Praseodymium, etc. are capable of application in cement additives coating and paints, storage devices, magneto resistive, magnetocaloric, and CRT tubes [23]. These materials are multiferroics means they exhibit both ferroelectricity and ferromagnetism [24]. An essential ABO_3-type perovskite material is lanthanum orthoferrite ($LaFeO_3$) has a *Pbnm* space group orthorhombic crystal structure where magnetic and ferroelectric ordering seem to coexist [25]. Its absorbance spectra along with Nd/Sm doping with La are shown in the figure below.

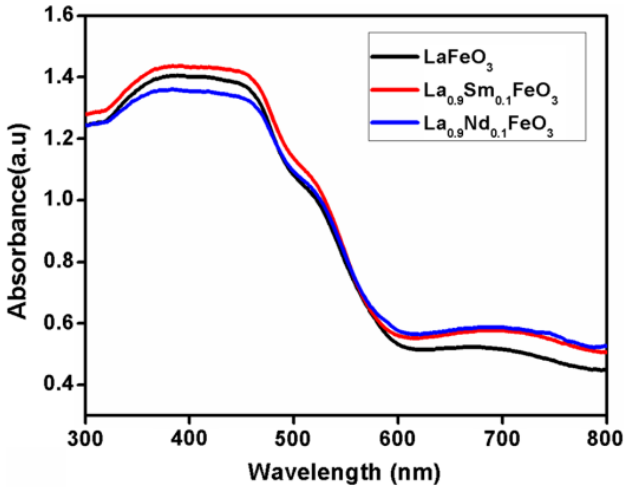

Figure 1.2: Absorbance spectra of $La_x(Sm/Nd)_{1-x}FeO_3$ [26]

The absorption spectra demonstrate significant visible light absorption at 593 nm. The absorption cut-off wavelengths for the lanthanum ferrite samples doped with Sm/Nd were seen to decline at 556/521 nm. Good absorption of visible light by $LaFeO_3$. This supports using them as visible light photocatalysts in optical applications.

1.4 APPLICATION OF PEROVSKITES

1.4.1 Perovskite Solar Cell (PSC)

Solar cells work by turning light energy into electrical energy through the photovoltaic phenomenon. In 2009, Miyasaka *et.al* [27] have fabricated the first

perovskite solar cell namely $CH_3NH_3PbI_3$ and $CH_3NH_3PbBr_3$ with power consumption efficiency (PCE) equivalent to 3.8% and 3.13% as presented in *Figure 1.3*.

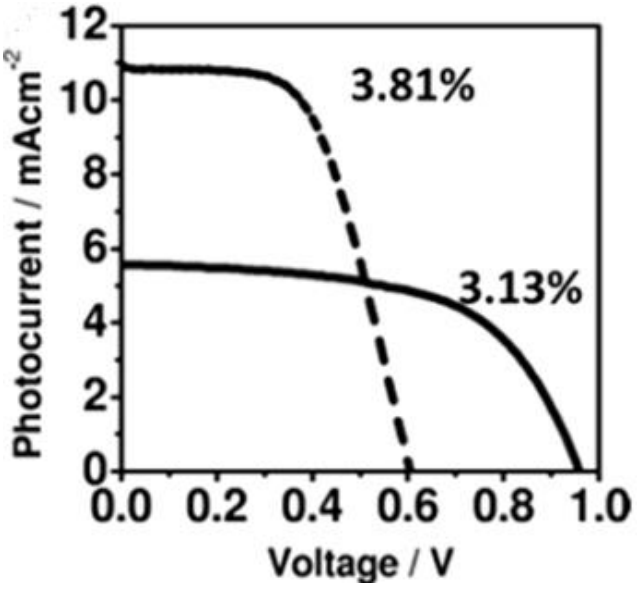

Figure 1.3: Photocurrent vs Voltage plot for PSC for $CH_3NH_3PbI_3/TiO_2$ (dashed line) & $CH_3NH_3PbBr_3/TiO_2$ (solid line) [27]

Lead (Pb) based perovskites have been the subject of the majority of PSC research. In the domain of solar technology, the Pb-PSC has made discernible development. The PCE of Pb-PSC has improved to 25.7% [29], approaching the highest value attained by silicon-based semiconducting solar devices.

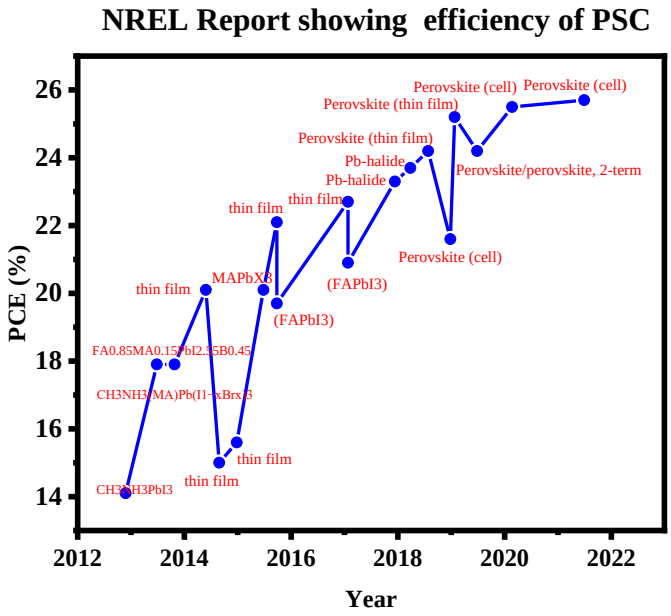

Figure 1.4: NREL report of perovskite solar cell efficiency [29]

NREL Report of PCE of perovskite solar cells has been presented in *Figure 1.4*. In this graph, FA and MA are formamidinium and methylammonium, respectively [28]. This study in the above graph shows the journey of PSCs in increment of efficiency of solar cells which keep on increasing with time. Not only changing the constituents of the compound but also the shape, size, and type affects the efficiency. As mentioned earlier lead Perovskite has shown remarkable increase in PCE.

Converse to lead PSCs, in recent years, perovskite materials without Pb [30-35] were also popular. Pb-based perovskites offer wonderful features, but they are poisonous and structurally unstable, which limits their use in a variety of industries [36]. The Sn-halide perovskites are alternatives to Pb perovskites with the potential to attain high PCE [37]. The stability of the structure for these perovskites is estimated via the Goldschmidt tolerance factor, which varies with ions' size within the compound. While considering the stability point, Pb in lead perovskites can be replaced with Sn^{2+}, Ge^{2+}, Mg^{2+}, etc. [38]. The tin-based perovskites are the first perovskite, substituting the lead as they possess an ionic radius (1.35 Å) identical to that of the Pb (1.49 Å). The Sn-based perovskites have low bandgap & strong carriers' mobility analogous to the Pb perovskites [39]. These compounds have promising optoelectronic properties.

1.4.2 Thermoelectric Materials

One more key concern is the waste heat which produces during the energy conversion process. Almost all processes of converting energy generate waste heat, which is regularly dumped into the environment. Future-oriented solutions must be found to increase process efficiency. Moreover, financial barriers can affect the proper utilization of waste heat. Possible aspects and solutions need to be considered. Certain measures that can be helpful are: Firstly, this waste heat is to be identified and avoided. Secondly, it can be used directly in the chain process and used locally within the environment. And finally, utilize this waste heat and convert it into energy resources via thermoelectric power generators (TEGs).

The technology behind TEGs is the transformation of unused heat into power. As estimated by Cullen and Allwood [40] around 63% of primary energy waste across the world is due to combustion and transfer activities. Lots of heat is generated via

transportation (motor vehicles, radiators, etc.), industrial, commercial, residential, etc. which remain unused. Thermoelectric technology is based on recycling waste heat for its efficient usage. Throughout the 1990s, there was a renewed excitement in thermoelectric technology, sparked by ideas like low-dimensional structures and new bulk materials. A significant parameter that regulates the proficiency of TE materials is known as figure of merit (*ZT*). For their practical application, *ZT* value should be equal to or greater than unity. Significant progress on improving *ZT* is still being made. Thermoelectric materials have shown their usage in cooling car seats, mobile refrigerators, medical instruments, temperature regulators in lasers, space applications, oil pipelines, and vehicle waste heat recovery.

1.4.3 Half Metallicity for Spintronics

Spintronics is the field in the area of material sciences that is associated with electron spin related to the spin degree of freedom. Instead of using a traditional charge current, a spin current is employed for transportation. Consequently, the transfer of information occurs at a higher speed with minimal heat generation. Giant Magnetoresistance (GMR) spikes up the impact of spintronics in modern field applications. The first commercial effect of spintronic has been used in magnetic hard disk drivers. Half metallic (HM) ferromagnets/antiferromagnets are utilized for spintronic applications. In HM materials both spins behave differently i.e., One spin exhibits metallicity, whereas the other exhibits either semiconducting or insulating behaviour. The idea of HM ferromagnets is originally presented in 1983 by de Groot *et.al* [41]. These composites have a magnetic moment which is an integral multiple of Bohr magneton. Some of the half-metallic ferromagnets are $PrMnO_3$ [42], $CeAlO_3$, $PrAlO_3$ [43], etc. Half-metallic antiferromagnets have zero net magnetic moments and have 100% spin polarization.

1.5 LITERATURE REVIEW

Longo, V. *et al.* (1981) [44] in their research work analyzed the X-ray characterization of Cerium-based oxide perovskite $ACeO_3$ where A is Sr, Be. For compound $BaCeO_3$ tetragonal phase is used for studying x-ray diffraction patterns. For different {h k l} values they observed interspacing d_{obs} and compared with d_{cal}

and observed intensity also. Sarma, D. *et al.* (1995) [45] described the electronic structure using local density approximation for La-based compounds $LaMO_3$, where M varies to Mn, Fe, Ni, and Co. Band theory, gives a better understanding of these kinds of compounds as it considers the strong transition metal interactions. Ball, C. J., *et al.* (1998) [46] have examined the structure system of $CaTiO_3/SrTiO_3$. It explains how the amount of Strontium ion in Calcium titanate/strontium titanate affects its phase. Material of composition, $Ca_{1-x}Sr_xO_3$, for $0 \leq x \leq 0.40$ phase is orthorhombic (Pnma); $0.45 \leq x \leq 0.6$ phase is orthorhombic (Bmmb); $0.65 \leq x \leq 0.9$ phase is tetragonal (I4/mcm); $x \geq 0.95$ phase is cubic (Pm3m) at room temperature. As the temperature increases, the phase boundary shift towards smaller content of Sr. Changes in volume resulting from phase transformation is smaller. The greatest shape change occurs for Bmmb/I4/mcm which is 0.3% and would probably be accommodated by micro twining, unlikely to affect the integrity of the specimen. Mete, E. *et al.* (2003) [47] investigated the $SrZrO_3$ and $SrTiO_3$ using DFT within LDA in its cubic phase achieved above 1400 K and 105 K, respectively. The energy band, charge distribution, and density of states are observed and compared. Takuji, M. *et al.* (2005) [48] prepared $SrRuO_3$'s sample to understand its TE behavior. With increasing temperature, electrical resistivity (σ) rises. which is an indication of the metallic nature of $SrRuO_3$. The Seebeck coefficient ($\mathcal{S}$) shows holes are in majority. The thermal conductivity shows positive relation with Madsen, G. *et al.* (2006) [49] developed a program for understanding the thermoelectric parameters of any material. They used smoothed Fourier interpolation of bands for calculating the semi-classical transport coefficient. Boopathy, K. *et al.* (2008) [50] synthesized Pb strontium zirconate. They have studied the Sr doping effect on the properties of lead zirconate. For all the compositions single orthorhombic phase of perovskite is observed. The dielectric properties come identical. Rached, H. *et al.* (2010) [51] presented elastic properties of Fe-based oxide perovskite $XFeO_3$ where X= Ba, Sr using FP-LMTO and LSDA methods. Both materials show metallic behavior. The magnetic moment of iron is more than {Sr, Ba}, and Oxygen contribution is negligible. $SrFeO_3$ is ductile while $BaFeO_3$ is brittle. Both compounds have high bulk modulus. Kumar, S., *et al.* (2014) [52] presented the transport properties of $SrTiO_3$ doped with Niobium oxide nanolayers. It is fabricated by layer-by-layer deposition of $LaAlO_3$ substrates. On

decreasing the thickness ratio of layer, σ and $\mathcal{S}$ increase. An irreversible change was observed at a high temperature (950 K) because of a change in phase from NbO (cubic) to Nb_2O_5 (orthorhombic). For stable operation, the T $\not>$ 950 K evades diffusion of the O layer from Strontium titanate to NbO interlayers which affects the stability of the superlattice and further result in the deterioration of σ and a sharp increase in $\mathcal{S}$. Tariq, S., *et al.* (2015) [53] have evaluated the structural, electronic, elastic characteristics of $CaTiO_3$ (1580 K) in cubic phase using GGA approximation with density functional theory under various temperatures and pressure. As pressure increases from 0 GPa to 120 GPa, the E_g switches from indirect to direct E_g. Bond length, lattice constant decrease as the pressure increases. On analysis of charge density, we infer that there is a strong ionic bond of Ca-Ti/O and a weak bond of O and Ti atoms under ambient pressure. At pressure 120 GPa bond between O and Ti is strong covalent while others remain as earlier. The perovskite is antiferromagnetic in nature. Elastic parameter increases with pressure. Shanmugapriya, K. *et al.* (2017) [54] studied the electronic and transport properties of $SrTiO_3$. Investigation of electronic performance was done by using DFT with plane wave pseudo-potential mechanism. XC function is GGA with PBE. Investigation of transport properties was done using BoltzTrap code with MWLF. The band structure graph shows indirect band gap occurs at (Γ-R) symmetry. σ, κ, ZT, and $\mathcal{S}$ were plotted w.r.t to chemical potential. Minimum electrical conductivity and thermal conductivity held between threshold 11 and 12.4 eV. The maximum value of electrical conductivity is beyond these threshold values. Jia, T. *et al.* (2017) [55] worked on evaluating lattice κ using elastic parameters. From elastic constants; lattice κ evaluated theoretically and matches with quasiharmonic phonon calculation and experimental values. Dar, S. *et al.* (2018) [56] proposed a theoretical investigation on $SrPuO_3$ perovskite. They worked on understanding the electronic, mechanical, and thermodynamic behavior of the above-mentioned perovskite. For this, they used the density functional theory with GGA, mBJ, GGA+U (onsite coulombic repulsion) used as XC function. In the case of spin-up, the compound act as a metal, and for spin down acts as a semiconductor. The largest magnetic moment is equal to 4μB with the major contributor being Pu. α decreases with pressure. Its value under ambient conditions was 2.60×10^{-5} /K. Thermodynamic parameters were evaluated using Quasi harmonic model for various

ranges of temperature and pressure. Elastic constant, bulk moduli, shear modulus, young modulus, etc also reported in this work. Marbouh, N. *et al.* (2019) [57] examined the Dirac semi-metallic $SrIrO_3$ compound. The first principle calculations were done employing DFT with FP-LAPW as incorporated in Wein2k's code. PBEsol with or without spin-orbital coupling correction (SOC) is used as an exchange-correlation potential. From elastic performances, it found that the material was stable and ductile. The electronic property reveals its semi-metallic nature while the thermodynamic property shows the material to be n-type. Results are matched with experimental data also. Sabir, B. *et al.* (2019) [58] predicted the behavior of orthorhombic structures by studying their structural stability and optical and thermoelectric parameters. FP-LAPW + lo method was used. WC-cohen, GGA+U approximation were used for finding the physics of three compounds i.e., $LaFeO_3$, $LaMnO_3$, $LaCrO_3$. Their band profile is different for the spin up and down. $LaMnO_3$ behaves metallic for spin up and semiconductor with a bandgap of 2.2eV for spin down. $LaFeO_3$ exhibits metallic behavior for a spin down and a semiconducting with 2.3 eV E_g for a spin up. $LaCrO_3$ has semiconducting character for both spins. The phonon dispersion curve showed positive values indicating that these materials are stable in the orthorhombic phase. Optical and thermoelectric properties were also evaluated. The negative value of the Seebeck coefficient depicts major charge carriers are electrons. The structure displays value of reflectivity to be smaller making it suitable for fabrication even in a harsh radiation environment. A high value of the dielectric constant and refractive index was reported. Material can be used as anodes for solar cells. Dar, S. *et al.* (2019) [59] investigated the double perovskite Ba_2InTaO_6. They worked on the optimization of the structure as well as an emphasis on developing a theoretical understanding of the properties of the compound. DFT calculation was done with Gradient generalized approximation, mBJ. For post-DFT calculation, they used the Boltzmann transport phenomenon. The compound was found to be semiconducting and direct band gap. Elastic and mechanical study shows that the material was stable, ductile, and anisotropic. Faghihnasiri, M. *et al.* (2020) [60] worked on Cs_2AgBiX_6. Phase transition and mechanical properties predicted using DFT as inbuilt in Quantum espresso. They found a pseudo-cubic phase in each cubic phase and found the ps-cubic phase to be more stable. Cubic and pseudocubic

phases for $Cs_2AgBiBr_6$ can be achieved at room temperature while for Cs_2AgBiI_6, it required more energy for phase transition. Radius of the halogen atom affects the value of the elastic constant for both phases. They also evaluated young's modulus using Perdew Burke Ernzerhof sol approximation. The young's modulus for $Cs_2AgBiBr_6$ shows a maximum value at 20.62 GPa in (111) direction, which matches with the experimental result. Khan, K. *et.al* (2021) [61] analyzed the study of electro-optical properties of $ASnX_3$. Converting from Cl to Br causes an E_g reduction, which has also shown an improvement in absorption coefficient. Rahman, M. *et.al* (2022) [62] work for lead-free perovskite such as $RbSnX_3$ for photovoltaic applications. using CASTEP package. Doping also affects the TE parameters like $Sr_{0.9}La_{0.1}TiO_3$ shows 0.21 ZT [63, 64]. ZT was found to increase in $SrTiO_3$ doping with La to Dy elements [64] Similar studies on various other perovskites like Mn-based $AMnO_3$ with A-site dopant (A = In, Sn, Sb, Pb, Bi) [65-67] and rare earth elements [68, 69] were also reported. An n-type doped $BaSnO_3$ was considered by Liu, J. *et al.* [70] using the DFT [71] in combination of Boltzmann theory [49]. The authors concluded that $BaSnO_3$ was found to be a robust material for thermoelectric uses on account of its ZT value (0.65) at 1200 K. Some Co-based perovskites like $RCoO_3$ with R= Pr, Ho, Nd, Tb, Sm, Gd, Dy [72-74] were also investigated concerning their thermoelectric behavior experimentally. Moreover, reports of comparable research on other substances [75-79]. A few rare earth (B-site) perovskites have recently undergone investigations like $BaNpO_3$ [80], $BaPuO_3$ [81], $BaAmO_3$ [82], $BaCmO_3$ [83], $BaZrO_3$ and $BaCeO_3$ [84], $BaBkO_3$ [85], $SrAmO_3$ [86], and $SrPuO_3$ [87].

1.6 AIMS AND OBJECTIVES

The objective of the research is to use computational and quantum mechanical treatment using first-principles density functional theory (DFT). A WIEN2K package in the framework of DFT would be used to investigate Perovskite compounds such as Perovskite oxides, Perovskite halides, and double Perovskite compounds. The materials would be investigated by considering the following objectives:

1. The optimization of the structure would be done by estimating total energy by considering appropriate approximations such as GGA, GGA+U, mBJ, etc. as an exchange-correlation function.

2. The electronic band profile, combined, and partial density of states will be studied.
3. Further, mechanical performances in terms of elastic constant and thermodynamic variables like Debye temperature, entropy, heat capacity, thermal expansion coefficient, etc. will also be estimated.
4. Examination of thermoelectric effects like Seebeck coefficient, thermal conductivity, the figure of merit, electrical conductivity, and power factor using semiclassical Boltzmann transport theory will also be done.

1.7 MOTIVATION AND FUTURE POSSIBILITIES

A recent strong motivation for the investigation of these properties of perovskites is the possibility of the emergence of novel physical phenomena and their potential applications in the design and fabrication of less expensive, more innovative, and more efficient optoelectronic devices. Perovskites have already gained immense interest in the photovoltaic solar cell but majorly used perovskite are hybrid organic-inorganic based on lead (Pb). Lead-based perovskites continually confront a wide range of commercial obstacles to be used on a big scale owing to the toxicity of Lead and structural instability. Finding safe and non-toxic perovskites is decisive for the continued production of PSCs. Hydrophobic moieties, multi-cation substitution, and carbon encapsulation can all help to reduce the halide perovskites' instability issue. The substitution of Pb with non-toxic elements is the also option to lessen the toxicity of perovskite products. The Sn-halide perovskites are alternatives to Pb perovskites The tin-based perovskites are the first perovskite, substituting the lead as they possess an ionic radius (1.35 Å) identical to that of the Pb (1.49 Å). The Sn-based perovskites have a low bandgap and strong carriers' mobility analogous to the Pb perovskites. These compounds have promising optoelectronic properties.

The investigation of alternative tin-based perovskites as potential substitutes for lead-based perovskites in optoelectronic devices represents a recent advancement. Tin-based perovskites have gained attention due to their similar ionic radius to lead, low bandgap, and strong carrier mobility, making them promising candidates for applications like photovoltaic solar cells. The development of these non-toxic alternatives addresses the toxicity and structural instability associated with lead-based

perovskites, potentially paving the way for safer and more environmentally friendly optoelectronic devices.

The findings of our research contribute valuable information to experimentalists working in the field. Our study equips researchers with the knowledge necessary to synthesize these compounds and integrate them into energy-related applications. By sharing insights into the properties, stability-enhancing techniques, and alternative element substitutions, our research paves the way for the practical utilization of perovskite materials. It could have a profound impact on the development of sustainable energy technologies and the transition towards safer and more efficient optoelectronic devices.

1.8 THESIS OUTLINE

The thesis titled "**First principles calculations on diverse properties of some Perovskite compounds**" is a comprehensive study of various properties of some oxide as well as halide perovskite. The six chapters that make up this thesis are briefly summarized as follows:

The first chapter began with a general introduction and includes some information regarding the Perovskite structure and its various types. Perovskite applications such as solar cells, TEGs, and Spintronics are also covered. Additionally, a literature review, the aim and objective of the current work, and the motivation for the current effort are described.

The second chapter covers density functional theory and exchange-correlation functions including LDA, GGA, and mBJ. To foster correlated effects, Hubbard approximation LDA/GGA/mBJ+U is also incorporated. We have talked about different basis sets for solving the Schrödinger equation for systems with numerous electrons. Lastly, ab initio methods for calculating thermoelectric, elastic, mechanical, and thermodynamic characteristics.

The third chapter provides information regarding electrical, structural, elasto-mechanical, thermodynamic, and TE properties of the perovskite $MgCeO_3$, $CaCeO_3$, $SrCeO_3$, and $BaCeO_3$ using the FPLAPW approach as instigated in the WIEN2K

algorithm. XC: PBE, PBEsol, WC, and mBJ are used for calculating band structure. The Quasi Harmonic Debye model is used for thermodynamic calculations, the IR elast package for elastic and mechanical calculations, and the Boltzmann transport phenomena for thermoelectric calculations.

The fourth Chapter provides information regarding structural, electrical, magnetic, thermodynamic, and thermoelectric properties using DFT via WIEN2K code for $RFeO_3$ (R=Nd, Pr).

Similarly, the fifth Chapter covers all the above properties for $RbSnCl_3$, $RbSnI_3$, $RbSnF_3$, and $RbSnBr_3$.

Finally, the entire thesis is summarized in the sixth Chapter, along with the conclusion and the future applications of the compounds.

REFERENCES

1. Komiyama, R. "Energy outlook to 2035 in Asia and its pathways towards a low carbon energy system." *World Energy Congress* (2010).
2. Tang, H., He, S. and Peng, C. "A short progress report on high-efficiency perovskite solar cells." *Nanoscale Research Letters* 12, no. 1 (2017): 1-8.
3. Docampo, P., Ball, J.M., Darwich, M., Eperon, G.E. and Snaith, H.J. "Efficient organometal trihalide perovskite planar-heterojunction solar cells on flexible polymer substrates." *Nature Communications* 4, no. 1 (2013): 2761.
4. Masi, S., Colella, S., Listorti, A., Roiati, V., Liscio, A., Palermo, V., Rizzo, A. and Gigli, G. "Growing perovskite into polymers for easy-processable optoelectronic devices." *Scientific Reports* 5, no. 1 (2015): 7725.
5. Stoumpos, C.C., Malliakas, C.D., Peters, J.A., Liu, Z., Sebastian, M., Im, J., Chasapis, T.C., Wibowo, A.C., Chung, D.Y., Freeman, A.J. and Wessels, B.W. "Crystal growth of the perovskite semiconductor $CsPbBr_3$: a new material for high-energy radiation detection." *Crystal Growth & Design* 13, no. 7 (2013): 2722-2727.
6. Li, L., Liu, X., He, C., Wang, S., Ji, C., Zhang, X., Sun, Z., Zhao, S., Hong, M. and Luo, J. "A potential Sn-based hybrid perovskite ferroelectric semiconductor." *Journal of the American Chemical Society* 142, no. 3 (2020): 1159-1163.
7. He, T., Huang, Q., Ramirez, A.P., Wang, Y., Regan, K.A., Rogado, N., Hayward, M.A., Haas, M.K., Slusky, J.S., Inumara, K. and Zandbergen, H.W. "Superconductivity in the non-oxide perovskite $MgCNi_3$." *Nature* 411, no. 6833 (2001): 54-56.
8. Dar, S.A., Srivastava, V. and Sakalle, U.K. "Ab initio high pressure and temperature investigation on cubic $PbMoO_3$ perovskite." *Journal of Electronic Materials* 46 (2017): 6870-6877.
9. Bhalla, A.S., Guo, R. and Roy, R. "The perovskite structure—a review of its role in ceramic science and technology." *Materials Research Innovations* 4, no. 1 (2000): 3-26.

10. Galasso, F.S. *Structure, properties and preparation of perovskite-type compounds: international series of monographs in solid state physics.* Vol. 5. Elsevier, 2013.
11. Assirey, E.A.R. "Perovskite synthesis, properties and their related biochemical and industrial application." *Saudi Pharmaceutical Journal* 27, no. 6 (2019): 817-829.
12. Schaak, R.E. and Mallouk, T.E. "Prying apart Ruddlesden− Popper phases: exfoliation into sheets and nanotubes for assembly of perovskite thin films." *Chemistry of Materials* 12, no. 11 (2000): 3427-3434.
13. Uma, S., Raju, A.R. and Gopalakrishnan, J. "Bridging the Ruddlesden–Popper and the Dion–Jacobson series of layered perovskites: Synthesis of layered oxides, A_{2-x} $La_2Ti_{3-x}Nb_xO_{10}$ (A= K, Rb), exhibiting ion exchange." *Journal of Materials Chemistry* 3, no. 7 (1993): 709-713.
14. Tsunoda, Y., Sugimoto, W. and Sugahara, Y. "Intercalation behavior of n-alkylamines into a protonated form of a layered perovskite derived from aurivillius phase $Bi_2SrTa_2O_9$." *Chemistry of Materials* 15, no. 3 (2003): 632-635.
15. Merz, W.J. "Switching time in ferroelectric $BaTiO_3$ and its dependence on crystal thickness." *Journal of Applied Physics* 27, no. 8 (1956): 938-943.
16. Mackenzie, A.P., Julian, S.R., Diver, A.J., McMullan, G.J., Ray, M.P., Lonzarich, G.G., Maeno, Y., Nishizaki, S. and Fujita, T. "Quantum oscillations in the layered perovskite superconductor Sr_2RuO_4." *Physical Review Letters* 76, no. 20 (1996): 3786.
17. Asano, H., Hayakawa, J. and Matsui, M. "Preparation and properties of triple perovskite $La_{3-3x}Ca_{1+3x}Mn_3O_{10}$ ferromagnetic thin films." *Applied Physics Letters* 71, no. 6 (1997): 844-846.
18. Rao, C.N.R. "Transition metal oxides." *Annual Review of Physical Chemistry* 40, no. 1 (1989): 291-326.
19. Goodenough, J.B. *Magnetism and the chemical bond.* Vol. 1. Interscience publishers, 1963.
20. Rao, C.N.R., and Jagannatha G. *New directions in solid state chemistry.* Cambridge University Press, 1997.

21. Khomskii, D.I. "Multiferroics: Different ways to combine magnetism and ferroelectricity." *Journal of Magnetism and Magnetic Materials* 306, no. 1 (2006): 1-8.
22. Mikami, M, and Nakamura S. "Electronic structure of rare-earth sesquioxides and oxysulfides." *Journal of Alloys and Compounds* 408 (2006): 687-692.
23. Dilawar, N., Mehrotra, S., Varandani, D., Kumaraswamy, B.V., Haldar, S.K. and Bandyopadhyay, A.K. "A Raman spectroscopic study of C-type rare earth sesquioxides." *Materials Characterization* 59, no. 4 (2008): 462-467.
24. Schmid, H. "Multi-ferroic magnetoelectrics." *Ferroelectrics* 162, no. 1 (1994): 317-338.
25. Acharya, S., Mondal, J., Ghosh, S., Roy, S.K. and Chakrabarti, P.K. "Multiferroic behavior of lanthanum orthoferrite ($LaFeO_3$)." *Materials Letters* 64, no. 3 (2010): 415-418.
26. RameshKumar, R., Ramachandran, T., Natarajan, K., Muralidharan, M., Hamed, F. and Kurapati, V. "Fraction of rare-earth (Sm/Nd)-lanthanum ferrite-based perovskite ferroelectric and magnetic nanopowders." *Journal of Electronic Materials* 48 (2019): 1694-1703.
27. Kojima, A., Teshima, K., Shirai, Y. and Miyasaka, T. "Organometal halide perovskites as visible-light sensitizers for photovoltaic cells." *Journal of the American Chemical Society* 131, no. 17 (2009): 6050-6051.
28. Jena, A.K., Kulkarni, A. and Miyasaka, T. "Halide perovskite photovoltaics: background, status, and future prospects." *Chemical Reviews* 119, no. 5 (2019): 3036-3103.
29. NREL, Best research-cell efficiency chart | photovoltaic research | NREL Best Research-Cell Efficiency Chart, 2022.
30. Yang, Z., Rajagopal, A., Chueh, C.C., Jo, S.B., Liu, B., Zhao, T. and Jen, A.K.Y. "Stable low-bandgap Pb–Sn binary perovskites for tandem solar cells." *Advanced Materials* 28, no. 40 (2016): 8990-8997.
31. Yu, Y., Zhao, D., Grice, C.R., Meng, W., Wang, C., Liao, W., Cimaroli, A.J., Zhang, H., Zhu, K. and Yan, Y. "Thermally evaporated methylammonium tin triiodide thin films for lead-free perovskite solar cell fabrication." *RSC Advances* 6, no. 93 (2016): 90248-90254.

32. Yokoyama, T., Cao, D.H., Stoumpos, C.C., Song, T.B., Sato, Y., Aramaki, S. and Kanatzidis, M.G. "Overcoming short-circuit in lead-free $CH_3NH_3SnI_3$ perovskite solar cells via kinetically controlled gas–solid reaction film fabrication process." *The Journal of Physical Chemistry Letters* 7, no. 5 (2016): 776-782.
33. Yang, Z., Rajagopal, A., Jo, S.B., Chueh, C.C., Williams, S., Huang, C.C., Katahara, J.K., Hillhouse, H.W. and Jen, A.K.Y. "Stabilized wide bandgap perovskite solar cells by tin substitution." *Nano Letters* 16, no. 12 (2016): 7739-7747.
34. Jung, M.C., Raga, S.R. and Qi, Y. "Properties and solar cell applications of Pb-free perovskite films formed by vapor deposition." *RSC Advances* 6, no. 4 (2016): 2819-2825.
35. Zhang, M., Lyu, M., Yun, J.H., Noori, M., Zhou, X., Cooling, N.A., Wang, Q., Yu, H., Dastoor, P.C. and Wang, L. "Low-temperature processed solar cells with formamidinium tin halide perovskite/fullerene heterojunctions." *Nano Research* 9, no. 6 (2016): 1570-1577.
36. Babayigit, A., Ethirajan, A., Muller, M. and Conings, B. "Toxicity of organometal halide perovskite solar cells." *Nature Materials* 15, no. 3 (2016): 247-251.
37. Benkabou, M.H., Harmel, M., Haddou, A., Yakoubi, A., Baki, N., Ahmed, R., Al-Douri, Y., Syrotyuk, S.V., Khachai, H., Khenata, R. and Voon, C.H. "Structural, electronic, optical and thermodynamic investigations of $NaXF_3$ (X= Ca and Sr): first-principles calculations." *Chinese Journal of Physics* 56, no. 1 (2018): 131-144.
38. Hoefler, S.F., Trimmel, G. and Rath, T. “Progress on Lead-free Metal Halide Perovskites for Photovoltaic Applications: A review.” *Monatshefte für Chemie - Chemical Monthly* 148 (2017): 795−826.
39. Stoumpos, C.C., Malliakas, C.D. and Kanatzidis, M.G. “Semiconducting Tin and Lead Iodide Perovskites with Organic Cations: Phase Transitions, High Mobilities, and Near-Infrared Photoluminescent Properties.” *Inorganic Chemistry* 52 (2013): 9019−903.
40. Cullen, J.M. and Allwood, J.M. "Theoretical efficiency limits for energy conversion devices." *Energy* 35, no. 5 (2010): 2059-2069.

41. De Groot, R.A., Mueller, F.M., van Engen, P.V. and Buschow, K.H.J. "New class of materials: half-metallic ferromagnets." *Physical Review Letters* 50, no. 25 (1983): 2024.
42. Bouadjemi, B., Bentata, S., Abbad, A., Benstaali, W. and Bouhafs, B. "Half-metallic ferromagnetism in $PrMnO_3$ perovskite from first principles calculations." *Solid State Communications* 168 (2013): 6-10.
43. Butt, M.K., Yaseen, M., Iqbal, J., Altowyan, A.S., Murtaza, A., Iqbal, M. and Laref, A. "Structural, electronic, half–metallic ferromagnetic and optical properties of cubic $MAlO_3$ (M= Ce, Pr) perovskites: a DFT study." *Journal of Physics and Chemistry of Solids* 154 (2021): 110084.
44. Longo, V., Ricciardiello, F. and Minichelli, D. "X-ray characterization of $SrCeO_3$ and $BaCeO_3$." *Journal of Materials Science* 16 (1981): 3503-3505.
45. Sarma, D.D., Shanthi, N., Barman, S.R., Hamada, N., Sawada, H. and Terakura, K. "Band Theory for Ground-State Properties and Excitation Spectra of Perovskite $LaMO_3$ (M= Mn, Fe, Co, Ni)." *Physical Review Letters* 75, no. 6 (1995): 1126.
46. Ball, C.J., Begg, B.D., Cookson, D.J., Thorogood, G.J. and Vance, E.R. "Structures in the system $CaTiO_3/SrTiO_3$." *Journal of Solid State Chemistry* 139, no. 2 (1998): 238-247.
47. Mete, E., Shaltaf, R. and Ellialtıoğlu, Ş. "Electronic and structural properties of a 4 d perovskite: cubic phase of $SrZrO_3$." *Physical Review* B 68, no. 3 (2003): 035119.
48. Maekawa, T., Kurosaki, K., Muta, H., Uno, M. and Yamanaka, S. "Thermoelectric properties of perovskite type strontium ruthenium oxide." *Journal of Alloys and Compounds* 387, no. 1-2 (2005): 56-59.
49. Madsen, G.K. and Singh, D.J. "BoltzTraP. A code for calculating band-structure dependent quantities." *Computer Physics Communications* 175, no. 1 (2006): 67-71.
50. Boopathy, K., Samson Nesaraj, A. and Rajendran, V. "Self-propagating combustion synthesis of $Pb_{1-x}Sr_xZrO_3$ ($0 \leq x \leq 0.20$) ceramics and their dielectric properties." *Bulletin of Materials Science* 31, no. 2 (2008).

51. Rached, H., Rached, D., Rabah, M., Khenata, R. and Reshak, A.H. "Full-potential calculation of the structural, elastic, electronic and magnetic properties of $XFeO_3$ (X= Sr and Ba) perovskite." *Physica B: Condensed Matter* 405, no. 17 (2010): 3515-3519.
52. Kumar, S.S., Hedhili, M.N., Cha, D., Tritt, T.M. and Alshareef, H.N. "Thermoelectric properties of strontium titanate superlattices incorporating niobium oxide nanolayers." *Chemistry of Materials* 26, no. 8 (2014): 2726-2732.
53. Tariq, S., Ahmed, A., Saad, S. and Tariq, S. "Structural, electronic and elastic properties of the cubic $CaTiO_3$ under pressure: A DFT study." *AIP Advances* 5, no. 7 (2015): 077111.
54. Shanmugapriya, K., Palanivel, B. and Murugan, R. "Electronic and thermoelectric properties of $SrTiO_3$." *Current Smart Materials* 2, no. 1 (2017): 73-79.
55. Jia, T., Chen, G. and Zhang, Y. "Lattice thermal conductivity evaluated using elastic properties." *Physical Review B* 95, no. 15 (2017): 155206.
56. Dar, S.A., Srivastava, V., Sakalle, U.K., Rashid A., and Pagare, G. "First-principles investigation on electronic structure, magnetic, mechanical and thermodynamic properties of $SrPuO_3$ perovskite oxide." *Materials Research Express* 5, no. 2 (2018): 026106.
57. Marbouh, N., Khodja, M.D., Boudali, A., Chibani, S. and Bentayeb, A. "Structural, mechanical, electronic structure and thermoelectric properties of Dirac semimetallic $SrIrO_3$ compound: a first-principles study." *Computational Condensed Matter* 21 (2019): e00420.
58. Sabir, B., Murtaza, G. and Khalil, R.A. "Ab-initio prediction of structure stability, electromagnetic, optical and thermoelectric behavior of orthorhombic $LaXO_3$ (X= Cr, Mn, Fe): For device application." *Journal of Molecular Graphics and Modelling* 94 (2020): 107482.
59. Dar, S.A., Sharma, R., Srivastava, V. and Sakalle, U.K. "Investigation on the electronic structure, optical, elastic, mechanical, thermodynamic and thermoelectric properties of wide band gap semiconductor double perovskite Ba_2InTaO_6." *RSC Advances* 9, no. 17 (2019): 9522-9532.

60. Faghihnasiri, M., Beheshtian, J., Shayeganfar, F. and Shahsavari, R. "Phase transition and mechanical properties of cesium bismuth silver halide double perovskites (Cs_2AgBiX_6, X= Cl, Br, I): a DFT approach." *Physical Chemistry Chemical Physics* 22, no. 10 (2020): 5959-5968.
61. Khan, K., Sahariya, J. and Soni, A. "Structural, electronic and optical modeling of perovskite solar materials $ASnX_3$ (A= Rb, K; X= Cl, Br): first principle investigations." *Materials Chemistry and Physics* 262 (2021): 124284.
62. Rahman, M.H., Jubair, M., Rahaman, M.Z., Ahasan, M.S., Ostrikov, K.K. and Roknuzzaman, M. "$RbSnX_3$ (X= Cl, Br, I): promising lead-free metal halide perovskites for photovoltaics and optoelectronics." *RSC Advances* 12, no. 12 (2022): 7497-7505.
63. Liu, J., Wang, C.L., Su, W.B., Wang, H.C., Zheng, P., Li, J.C., Zhang, J.L. and Mei, L.M. “Enhancement of thermoelectric efficiency in oxygen-deficient $Sr_{1-x}La_xTiO_{3-\delta}$ ceramics.” *Applied Physics Letters* 95, no. 16 (2009): 162110.
64. Muta, H., Kurosaki, K. and Yamanaka, S. “Thermoelectric performances of rare earth doped $SrTiO_3$.” *Journal of Alloys and Compounds* 350, no. 1-2 (2003): 292-295.
65. Ohtaki, M., Koga, H., Tokunaga, T., Eguchi, K. and Arai, H. “Electrical transport performances and high-temperature thermoelectric performance of $(Ca_{0.9}M_{0.1})MnO_3$ (M= Y, La, Ce, Sm, In, Sn, Sb, Pb, Bi).” *Journal of Solid State Chemistry* 120, no. 1 (1995): 105-111.
66. Xu, G., Funahashi, R., Matsubara, I., Shikano, M. and Zhou, Y. “High-temperature Thermoelectric Performances of the $Ca_{1-x}Bi_xMnO_3$ System.” *Journal of Materials Research* 17, no. 5 (2002): 1092-1095.
67. Hashimoto, S.I. and Iwahara, H. “Study on the structural and electrical performances of $Sr_{1-x}Ce_xMnO_{3-\alpha}$(x= 0.1, 0.3) perovskite oxide.” *Materials Research Bulletin* 35, no. 14-15 (2000): 2253-2262.
68. Flahaut, D., Mihara, T., Funahashi, R., Nabeshima, N., Lee, K., Ohta, H. and Koumoto, K. “Thermoelectrical performances of A-site substituted $Ca_{1-x}Re_xMnO_3$ system.” *Journal of Applied Physics* 100, no. 8 (2006): 084911.

69. Nakatsugawa, H., Kubota, M. and Saito, M. “Thermoelectric and Magnetic Performances of $Pr_{1-x}Sr_xMnO_3$ ($0.1 \leqq x \leqq 0.7$).” *Materials Transactions* 56, no 6 (2015): 864-871.
70. Li, J., Ma, Z., Sa, R. and Wu, K. “Improved thermoelectric power factor and conversion efficiency of perovskite barium stannate.” *RSC Advances* 7, no. 52 (2017): 32703-32709.
71. Hohenberg, P. and Kohn, W. “Inhomogeneous electron gas.” *Physical Review* 136, no. 3B (1964): B864.
72. Moon, J.W., Seo, W.S., Okabe, H., Okawa, T. and Koumoto, K. “Ca-doped $RCoO_3$ (R= Gd, Sm, Nd, Pr) as thermoelectric materials.” *Journal of Materials Chemistry* 10, no. 9 (2000): 2007-2009.
73. Moon, J.W., Seo, W.S., Okabe, H., Okawa, T. and Koumoto, K. “Influence of ionic size of rare-earth site on the thermoelectric performances of $RCoO_3$-type perovskite cobalt oxides.” *Materials Science and Engineering: B* 85, no. 1 (2001): 70-75.
74. Hashimoto, H., Kusunose, T. and Sekino, T. “Influence of ionic sizes of rare earths on thermoelectric performances of perovskite-type rare earth cobalt oxides $RCoO_3$ (R= Pr, Nd, Tb, Dy).” *Journal of Alloys and Compounds* 484, no. 1-2 (2009): 246-248.
75. Kaur, T., Kumar, S., Bhat, B.H., Want, B. and Srivastava, A.K. "Effect on dielectric, magnetic, optical and structural properties of Nd–Co substituted barium hexaferrite nanoparticles." *Applied Physics A* 119, no. 4 (2015): 1531-1540.
76. Kaur, T., Kaur, B., Bhat, B.H., Kumar, S. and Srivastava, A.K. "Effect of calcination temperature on microstructure, dielectric, magnetic and optical properties of $Ba_{0.7}La_{0.3}Fe_{11.7}Co_{0.3}O_{19}$ hexaferrites." *Physica B: Condensed Matter* 456 (2015): 206-212.
77. Mukherjee, R. "Electrical, thermal and elastic properties of methylammonium lead bromide single crystal." *Bulletin of Materials Science* 43, no. 1 (2020): 1-5.
78. Sharma, J, Kumar, A., Kumar, S., and Srivastava, A.K. "Investigation of structural and magnetic properties of Tb–Ni-doped bismuth ferrite nanoparticles by auto-combustion method." *Applied Physics A* 123, no. 8 (2017): 1-9.

79. Sharma, J., Bhat, B.H., Kumar, A., Kumar, S., Kaur, T., Want, B., and Srivastava, A.K. "Magnetic and dielectric properties of Ce–Co substituted $BiFeO_3$ multiferroics." *Materials Research Express* 4, no. 3 (2017): 036104.
80. Dar, S.A., Khandy, S.A., Islam, I., Gupta, D.C., Sakalle, U.K., Srivastava, V. and Parrey, K. "Temperature and pressure dependent electronic, mechanical and thermal properties of f-electron based ferromagnetic barium neptunate." *Chinese Journal of Physics* 55, no. 5 (2017): 1769-1779.
81. Dar, S.A., Srivastava, V., Sakalle, U.K. and Pagare, G. "Insight into structural, electronic, magnetic, mechanical, and thermodynamic properties of actinide perovskite $BaPuO_3$." *Journal of Superconductivity and Novel Magnetism* 31, no. 10 (2018): 3201-3208.
82. Dar, S.A., Srivastava, V., Sakalle, U.K., Ahmad Khandy, S. and Gupta, D.C. "A DFT study on structural, electronic mechanical and thermodynamic properties of 5f-electron system $BaAmO_3$." *Journal of Superconductivity and Novel Magnetism* 31 (2018): 141-149.
83. Dar, S.A., Srivastava, V., Sakalle, U.K. and Parey, V. "Ferromagnetic phase stability, magnetic, electronic, elasto-mechanical and thermodynamic properties of $BaCmO_3$ perovskite oxide." *Journal of Electronic Materials* 47 (2018): 3809-3816.
84. Yamanaka, S., Fujikane, M., Hamaguchi, T., Muta, H., Oyama, T., Matsuda, T., Kobayashi, S.I. and Kurosaki, K. "Thermophysical properties of $BaZrO_3$ and $BaCeO_3$." *Journal of Alloys and Compounds* 359, no. 1-2 (2003): 109-113.
85. Nabi, M., Bhat, T.M. and Gupta, D.C. "Magneto-Electronic, Thermodynamic, and Thermoelectric Properties of 5 f-Electron System $BaBkO_3$." *Journal of Superconductivity and Novel Magnetism* 32 (2019): 1751-1759.
86. Dar, S.A., Srivastava, V., Sakalle, U.K. "A first-principles calculation on structural, electronic, magnetic, mechanical, and thermodynamic properties of $SrAmO_3$." *Journal of Superconductivity and Novel Magnetism* 30, no. 11 (2017): 3055-3063.
87. Dar, S.A., Srivastava, V., Sakalle, U.K., Rashid, A., Pagare, G. First-principles investigation on electronic structure, magnetic, mechanical and thermophysical

performances of $SrPuO_3$ perovskite oxide. *Materials Research Express* 5, no. 2 (2018): 026106.

CHAPTER 2

METHODOLOGY

2.1 INTRODUCTION

The invention of the computer changes the aspect of dealing with the challenges of life. The world has excellent processing power, which is always expanding. The world's expanding computer power also made it impossible for material science to withstand it. Over time, many computational models have been put forth, and a brand-new field of study known as computational material science has emerged. It is currently relatively easy to choose a material for use in devices that need to have clearly defined physical features thanks to computational methods. Additionally, working with specific materials in the lab can be dangerous and time-consuming for material researchers, which can be significantly lowered through material screening using computing. It not just explores the fundamental materials but also explores the characterization and optimization of innovative materials. Due to this, less time and money are now needed to find the right supplies. As a result, computational approaches that can ascertain pertinent physical aspects of materials such as their chemical composition, crystal structure, and optical, thermoelectrical, and thermodynamic properties are highly sought after in both industrial and academic research.

Density functional theory (DFT) [1, 2] is a successful quantum mechanical approach to solving the equation of many electrons and nuclei systems, also known as the Schrödinger equation (S.E). This approach has been followed by large numbers of researchers across the globe to understand the behavior of materials in different physical situations. It not only deals with bulk materials but also with thin films and doped materials. DFT has aided in the theoretical prediction of the applicability of novel materials with ideal physical properties and an understanding of experimental results. Theoretical data and experimental data agree with one other.

This chapter provides brief information about the DFT, Born Oppenheimer approximation, Kohn-Sham equation, Variational principle, and approximation

methods' approach to solving many body problems and the methodology used in solving elastic, thermodynamic, and thermoelectric behavior of materials.

2.2 DENSITY FUNCTIONAL THEORY

The crystal structure consists of unit cells, the smallest/ fundamental of crystal, having atoms and molecules. We must search for the materials' ground state energies to define their qualities. This concept of theory based on density is first introduced by fermi and Thomas [3, 4]. Later in 1964, W. Kohn, L.J. Sham, and P. Hohenberg found the solution of many bodies system by implication of variational principle with a density as variable [5]. It demonstrates the system's precise ground state by just looking at the ground state density. This served as the basis for developing a useful tool in virtual systems that transformed the time-consuming task of handling multiple bodies Schrödinger equations into relatively straight forward one-particle equations. In this regard, DFT [1, 2] has been chosen to be the best approach to deal with research problems in material sciences. Further, DFT help in finding several properties like band structure, stable crystal phase, effective mass, exciton binding energy, elasticity, mechanical, optical, thermodynamics, thermoelectric, etc.

2.2.1 Wave Function Approach

In contrast to the various electron wave functions $\psi(r_1, r_2, r_3, ...)$, this theory is based on electron density distribution ($\rho(r)$). Solids consist of many electrons which are surrounded by nuclei and Schrödinger equation

$$\hat{H}\,\psi = E\psi \tag{2.1}$$

where ψ is the eigenstates of Hamiltonian and $\hat{H}$ is Hamiltonian operator. Each of these eigenstates is associated with eigenvalue E. For multiple electron systems interacting with each other as well as with multiple nuclei, Hamiltonian is represented as

$$\hat{H} = -\frac{\hbar^2}{2m_e}\sum_i \nabla_i^2 - \frac{\hbar^2}{2}\sum_j \frac{\nabla_j^2}{M_j} + \frac{1}{8\pi\epsilon}\sum_{i\neq j}\frac{e^2}{|r_i - r_j|} + \frac{1}{8\pi\epsilon}\sum_{i\neq j}\frac{e^2 Z_i Z_j}{|R_i - R_j|} - \frac{1}{4\pi\epsilon}\sum_{i\neq j}\frac{Z_j e^2}{|R_j - r_i|} \tag{2.2}$$

Hamiltonian operator consists of five terms which are defined in the order of kinetic energy (K.E) of each electron and nucleus, Coulombic interaction (C.I) among electrons, Coulombic interaction among nuclei, and Coulombic interaction between

electron and nuclei, respectively [6]. The exact solution of the above equation is a practically impossible task for systems having more than a few electrons. For nearly a century, many brilliant minds have worked for the solution of Schrödinger equation for practical materials. In this regard, certain approximations and techniques are needed.

2.2.2 Born Oppenheimer Approximation (BOA)

BOA provides the remedy to decouple electronic and ionic parts in the Hamiltonian equation. It is based on the fact that the electron mass is 1800 times less than the proton or neutron mass in a nucleus. Therefore, electrons are highly responsive to the changes in the surroundings as compared to neutrons and protons present in the nucleus and attained their ground state configuration very quickly. Subsequently, the K.E of nuclei is almost zero owing to their lower velocity, and Coulombic interaction among nuclei is considered to be constant [7]. This indicates that compared to nuclei, electrons' movement is faster. In the typical time scale of nuclear motion, it is plausible to assume that electrons react immediately and return to their stable configuration. The nuclei are essentially totally confined around a single location in this sense. Therefore, the physical system can be split into electronic and nuclear parts.

$$\psi = \psi_e(r_1, r_2, r_3, \ldots . r_n; R_{1,}, R_2, R_3, \ldots . R_N)\psi_n(R_{1,}, R_2, R_3, \ldots . R_N) \qquad (2.3)$$

Where ψ_e is the wave function (ψ) of an electron having electronic as well as nuclei positions and ψ_n is the wave function of the nucleus depends only on nuclei position. Born Oppenheimer approximation results in vanishing second and fourth terms of *equation (2.2)*. Therefore, the equation reduces to

$$\widehat{H_e} = -\frac{\hbar^2}{2m_e}\sum_i \nabla_i^2 + \frac{1}{8\pi\epsilon}\sum_{i\neq j}\frac{e^2}{|r_i - r_j|} + \frac{1}{4\pi\epsilon}\sum_{i\neq j}\frac{Z_j e^2}{|R_j - r_i|} \qquad (2.4)$$

$$\hat{H}_e\psi_e = E_e\psi_e \qquad (2.5)$$

Electronic properties of the solid, focus on solving *equation (2.4)*. Solving the above equation for a large system is not an easy task attributable to the e^--e^- repulsion term. The Hamiltonian of the equation cannot be determined unless we know the positions r_i of electrons and position r_i cannot be determined unless we know the Hamiltonian for electrons ($\hat{H}_e$). To solve this puzzle, self-consistent field approach was anticipated.

2.2.3 Self-Consistent Field (SCF) Approach

SCF approach has been followed to solve the Schrödinger equation of many electrons system. According to SCF, one has to first guess trial charge density, then solve Schrödinger equation to calculate wave function. Further, construct potential from the computed wave function. Schrödinger equation has been solved iteratively unless convergence criteria are met. The flow chart showing the algorithm of the SCF phenomenon is as follows [8].

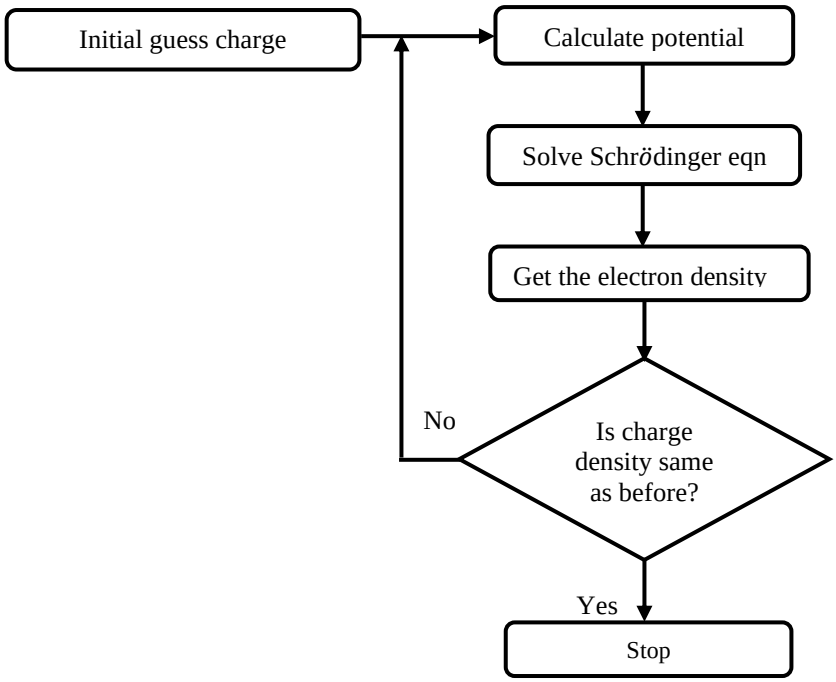

Figure 2.1: Flowchart of SCF approach

2.2.4 Hartee-Fock Approximation

Hartee proposed a theory in 1948 in which ψ & E of the multielectron system are approximated. In this approximation, the ψ of N electron system $\psi(\mathbf{r_i})$ is considered to be the product of individual electron's wave functions $\phi_i(\mathbf{r}_i)$. This product is known as Hartee product and is given as [9]

$$\psi(r_i) = \phi_1(\mathbf{r}_1).\phi_2(\mathbf{r}_2).\phi_3(\mathbf{r}_3) \dots \dots \phi_N(\mathbf{r}_N) \quad (2.6)$$

Starting with the wave function and invoking the variational principle, $\hat{H}_e$ is minimized to get the solution for individual electrons.

$$(H_i + V_H)\,\phi_i(\mathbf{r_i}) = \varepsilon_i\phi_i(\mathbf{r}_i) \quad (2.7)$$

where H_i, Hamiltonian of i^{th} independent electron which is given as follows

$$H_i = -\frac{\hbar^2}{2m}\nabla_i^2 - \frac{1}{4\pi\epsilon}\sum_j \frac{Z_j e^2}{|\mathbf{R}_j - \mathbf{r}_j|} \tag{2.8}$$

and Hartee Potential V_H is given as

$$V_H = \frac{1}{8\pi\epsilon}\sum_{j\neq i}\int d^3\mathbf{r}_j' \frac{|\phi_j(\mathbf{r}_j')|^2 e^2}{|\mathbf{r}_i - \mathbf{r}_j'|} \tag{2.9}$$

The solution of the above equations can be achieved with the implication of the SCF approach which starts with guessing the trial wave function $\phi_i(\mathbf{r}_i)$.

The simplification provided in *equation (2.9)* doesn't consider the case in which particles are fermions and doesn't follow the Pauli exclusion principle which says that ψ must be antisymmetric during an exchange of fermions [10]. This is remedied by Hartee Fock's (HF) hypothesis, which states that a slater determinant of N single e^- wavefunctions that includes spin coordinates approaches the exact N body.

$$\psi(r_i, \sigma_i) = \frac{1}{\sqrt{N!}}\begin{vmatrix} \phi_1(\mathbf{r}_1, \boldsymbol{\sigma}_1) & \phi_2(\mathbf{r}_1, \boldsymbol{\sigma}_1) & \cdots & \phi_N(\mathbf{r}_1, \boldsymbol{\sigma}_1) \\ \phi_1(\mathbf{r}_2, \boldsymbol{\sigma}_2) & \phi_2(\mathbf{r}_2, \boldsymbol{\sigma}_2) & \cdots & \phi_N(\mathbf{r}_2, \boldsymbol{\sigma}_2) \\ \vdots & \vdots & \ddots & \vdots \\ \phi_1(\mathbf{r}_N, \boldsymbol{\sigma}_N) & \phi_2(\mathbf{r}_N, \boldsymbol{\sigma}_N) & \cdots & \phi_N(\mathbf{r}_N, \boldsymbol{\sigma}_N) \end{vmatrix} \tag{2.10}$$

This determinant ensures the Pauli exclusion principle as well as exchange symmetry. Thus, by trial wavefunction $\psi(\mathbf{r}_i, \boldsymbol{\sigma}_i)$ and invoking the variational method, H_e is minimized to get the solution for individual electrons [11]. Now, the HF equation expresses as follows

$$\begin{aligned} \epsilon_i\phi_i(\mathbf{r}, \sigma) &= (H_i + V_H)\,\phi_i(\mathbf{r}, \boldsymbol{\sigma}) \\ &+ \frac{1}{8\pi\epsilon}\sum_{k,\sigma'}\delta_{\boldsymbol{\sigma},\boldsymbol{\sigma}'}\int d^3\mathbf{r}'\left\{\frac{\phi_k{}^*(\mathbf{r}', \boldsymbol{\sigma}')\phi_i(\mathbf{r}', \boldsymbol{\sigma})e^2}{|\mathbf{r} - \mathbf{r}'|}\right\}\phi_k{}^*(\mathbf{r}', \boldsymbol{\sigma}) \end{aligned} \tag{2.11}$$

Here, the HF theory solely considers the Fermi correlation and excludes the correlation effect brought on by the C.I between the electrons. Therefore, we need to go beyond HF theory for evaluating the exact ground state.

2.2.5 DFT Approach

Although the SE's solution could be seen as the fundamental problem in quantum physics, it's crucial to realize that for any given coordinate set, solution cannot be explicitly viewed. In principle, the measurable quantity is probability. Density $\rho(r)$ is a closely related measurable quantity. Moreover, the wavefunction of N electrons has 3N electron coordinates while density is the only function of 3 coordinates. This

physically observable quantity density contains all information regarding solids just like wavefunction and can be measured from the current technology of XRD, TEM, AFM, and STM. The density of a solid is given as

$$\rho(r) = \int \psi^*(\mathbf{r}_i, \boldsymbol{\sigma}_i)\, \psi(\mathbf{r}_i, \boldsymbol{\sigma}_i)\, d\mathbf{r}_i \tag{2.12}$$

2.2.6 Hohenberg and Kohn Theorem

Two key theorems and a set of equations provided by P. Hohenberg and W. Kohn form the basis of DFT. [5].

The first theorem states that "ground state energy (E) from S.E is a unique functional of density (ρ) i.e., $E[\rho(\mathbf{r})]$. E and external potential (V_{ex}) have a one-to-one mapping. V_{ex} is uniquely resolved through ρ. This also states as ρ can uniquely determine all the properties including E as well as ψ".

To demonstrate the above theorem, we will look at two potentials $V_{ex}^{(1)}(\mathbf{r})$ and $V_{ex}^{(2)}(\mathbf{r})$ have ground-state functions $\psi^{(1)}$ and $\psi^{(2)}$, respectively and both have same density $\rho(\mathbf{r})$. External potentials result in two distinct Hamiltonian $\hat{H}^{(1)}$ and $\hat{H}^{(2)}$.

$$E^{(1)} = \langle \psi^{(1)} | \hat{H}^{(1)} | \psi^{(1)} \rangle < \langle \psi^{(2)} | \hat{H}^{(1)} | \psi^{(2)} \rangle \tag{2.13}$$

Also,

$$\langle \psi^{(2)} | \hat{H}^{(1)} | \psi^{(2)} \rangle = \langle \psi^{(2)} | \hat{H}^{(2)} | \psi^{(2)} \rangle + \langle \psi^{(2)} | \hat{H}^{(1)} - \hat{H}^{(2)} | \psi^{(2)} \rangle \tag{2.14}$$

$$= E^{(2)} + \int \left(V_{ex}^{(1)}(\mathbf{r}) - V_{ex}^{(2)}(\mathbf{r}) \right) \rho(\mathbf{r})\, d^3\mathbf{r} \tag{2.15}$$

Considering *equations (2.13)* and *(2.15)*, we can rewrite them as

$$E^{(1)} < E^{(2)} + \int \left(V_{ex}^{(1)}(\mathbf{r}) - V_{ex}^{(2)}(\mathbf{r}) \right) \rho(\mathbf{r})\, d^3\mathbf{r} \tag{2.16}$$

These labels (1) and (2) can be easily exchangeable. So, equation (2.16) can be rewritten as follows

$$E^{(2)} < E^{(1)} + \int \left(V_{ex}^{(2)}(\mathbf{r}) - V_{ex}^{(1)}(\mathbf{r}) \right) \rho(\mathbf{r})\, d^3\mathbf{r} \tag{2.17}$$

Adding *equations (2.16)* and *(2.17)* resulted into

$$E^{(1)} + E^{(2)} < E^{(2)} + E^{(1)} \tag{2.18}$$

Above equation contradicts our starting statement of the proof. This concludes the proof that two unique V_{ex} cannot create the same $\rho(\mathbf{r})$, i.e., V_{ex} is uniquely specified by $\rho(\mathbf{r})$.

Before discussing Hohenberg and Kohn's second theorem. Let me explain the variational principle briefly.

Variational Principle: "The energy calculated from a predicted ψ is an upper bound to the true ground state energy E_0". The true ground state is attained by full minimization of E corresponding to all allowed N e^- ψs.

$$E_0(\psi_0) = \min_\psi E(\psi) = \min_\psi \langle \psi | \hat{T}_e + \hat{V}_{ee} + \hat{V}_{en} | \psi \rangle \tag{2.19}$$

Where $\hat{T}_e$ is electron K.E's operator, $\hat{V}_{ee}$ is the potential energy among e^- and $\hat{V}_{en}$ is the potential energy between electrons and nuclei. Also, the Variational Principle

$$E(\psi) \geq E_0 \tag{2.20}$$

This means unless ψ corresponds to ψ_0, the energy is greater than that of the ground state.

According to the **second theorem**, "the actual electron density that corresponds to the complete solution of the S.E is the one that minimizes the energy of overall functional". This is the variational principle in action, but with density rather than the wave function.

$$E_0[\rho_0] = \min_\rho E[\rho] = \min_\rho T[\rho] + E_{ee}[\rho] + E_{en}[\rho] \tag{2.21}$$

$$E_{HK}[\rho] = T[\rho] + E_{ee}[\rho] + \int V_{ext}[\mathbf{r}]\rho(\mathbf{r})d^3\mathbf{r} \tag{2.22}$$

In the above equation the third term is system dependent while for the first two terms, we define a new functional known as Hohenberg Kohn (HK) density functional $F_{HK}[\rho]$ given as

$$F_{HK}[\rho] = E_{ee}[\rho] + T[\rho] \tag{2.23}$$

So,

$$E_{HK}[\rho] = \int V_{ext}[\mathbf{r}]\rho(\mathbf{r})d^3\mathbf{r} + F_{HK}[\rho] \tag{2.24}$$

$F_{HK}[\rho]$ functional is universally valid for any arbitrary many electrons system. This functional seems to be just like any other formulation but is very important. There wouldn't have been a need for approximations if it had been precisely known.

To prove the second HK theorem, we study $\rho^{(1)}(\mathbf{r})$ corresponds to $V_{ex}^{(1)}(\mathbf{r})$. After considering what was said above, it can be concluded that the H-K functional is equivalent to the Hamiltonian's expectation value in the specific ground state with a $\psi^{(1)}$.

$$E^{(1)} = E_{HK}[\rho^{(1)}] = \langle \psi^{(1)} | \hat{H}^{(1)} | \psi^{(1)} \rangle \quad (2.25)$$

Another density $\rho^{(2)}(\mathbf{r})$ corresponding to a wave function $\psi^{(2)}$. Thus,

$$E^{(2)} = \langle \psi^{(2)} | \hat{H}^{(1)} | \psi^{(2)} \rangle > E^{(1)} = \langle \psi^{(1)} | \hat{H}^{(1)} | \psi^{(1)} \rangle \quad (2.26)$$

Therefore *equation (2.24)* estimated the correct density $\rho_0(\mathbf{r})$ is surely lesser than the value of *equation (2.26)* evaluated for other densities.

The second HK theorem is also known as density variational principle. HK functional $F_{HK}[\rho]$ gives the lowest energy if and only if the density is the true $\rho(\mathbf{r})$.

2.2.7 Kohn-Sham Equation

Kohn and Sham developed modern DFT [6], and Kohn was bestowed with the 1998 Nobel Prize. The total energy of a solid consisting of interacting electrons is given as

$$E_e[\rho] = T_{ee}[\rho] + V_{ee}[\rho] + V_{en}[\rho] \quad (2.27)$$

$$E_e[\rho] = T_s[\rho] + V_H[\rho] + V_{en}[\rho] + \left\{ \underbrace{T_{ee}[\rho] - T_s[\rho]}_{E_C} \right\} + \left\{ \underbrace{V_{ee}[\rho] - V_H[\rho]}_{E_X} \right\} \quad (2.28)$$

where T_{ee} is the K.E of interacting electrons (e^-) in a solid, T_s is the K.E of non-interacting e^-s, V_{ee} & V_{en} are the potential energies due to e^--e^- interactions and electron-ion interactions, respectively, V_H is the Hartee potential. E_C and E_X are the correlation and exchange energies, respectively. The major involvement to the total energy comes from $T_s[\rho]$, $V_H[\rho]$, and $V_{en}[\rho]$.

$$E_{XC} = E_X + E_C \quad (2.29)$$

E_{XC} is the exchange-correlation energy that gives a minor contribution to total energy but is a very significant term for providing an exact description of the solids. Hamiltonian corresponding to the above equation, known as Kohn-Sham Hamiltonian is given as

$$\hat{H}_{KS} = \hat{T}_S + \hat{V}_{KS} \quad (2.30)$$

where $\hat{V}_{KS}$ is the Kohn-Sham potential given as

$$\hat{V}_{KS} = (\hat{V}_H + \hat{V}_{en} + \hat{V}_{XC}) \quad (2.31)$$

$\hat{V}_{XC}$ is the exchange-correlation potential

$$\hat{V}_{XC} = \frac{\delta E_{XC}}{\delta \rho} \quad (2.32)$$

This leads to the set of eigenvalues (ε_i) equations are known as Kohn-Sham equations:

$$\hat{H}_{KS}\phi_i(\mathbf{r}) = \varepsilon_i\phi_i(\mathbf{r}) \tag{2.33}$$

where, $\phi_i(\mathbf{r})$ the quasiparticle ψ of N lowest energy states. Density $\rho(\mathbf{r})$ of N number of particles for the non-interacting system is given as:

$$\rho(\mathbf{r}) = \sum_{i=1}^{N} \phi_i^*(\mathbf{r})\phi_i(\mathbf{r}) \tag{2.34}$$

$$N = \int \rho(\mathbf{r})d^3\mathbf{r} \tag{2.35}$$

Equations (2.30), (2.31), and *(2.33)* are well-known Kohn-Sham equations.

2.2.8 Exchange-Correlation (XC) Potential

Quantum mechanical systems can only be studied using the DFT technique if one is aware of XC energy, E_{XC}, and potential functional V_{XC} (*equation (2.32)*), which cannot be computed correctly. In this regard, we have briefly covered a few approximations that have been used to characterize XC energy and potential functionals such as Local Density Approximation (LDA), Generalized Gradient Approximation (GGA), etc. in the sections that follow.

2.2.8.1 Local Density Approximation (LDA)

The simplest XC functional is LDA introduced by Kohn-Sham [4, 5]. LDA is defined as a system of interacting electron gas in which the energy of XC of each small volume is equal to uniform homogenous e^- gas with the same density. LDA depends only on one variable i.e., electron density. Exchange correlation energy for LDA is given as

$$E_{XC}^{LDA}[\rho(\mathbf{r})] = \int \varepsilon_{XC}^{hom}(\rho(\mathbf{r}))\rho(\mathbf{r})d^3\mathbf{r} \tag{2.36}$$

$$\frac{\delta E_{XC}^{LDA}[\rho(\mathbf{r})]}{\delta\rho(r)} = \frac{d\left[\varepsilon_{XC}^{hom}\rho(\mathbf{r})\right]}{d\rho(\mathbf{r})} \tag{2.37}$$

$\varepsilon_{XC}^{hom}(\rho(\mathbf{r}))$ is XC energy for each e^-. LDA ignores the effect of inhomogeneities in electron density and this XC energy in LDA is local. LDA is appropriate only for non-spin polarized materials but not for magnetic materials' having more than one minimum of energy. For the spin-polarized system, LDA was modified to work for both spin up $\rho^{\uparrow}(\mathbf{r})$ as well as spin down $\rho^{\downarrow}(\mathbf{r})$ density which is named, local spin density approximation (LSDA) given as follows

$$E_{XC}^{LSDA}[\rho^{\uparrow}(\mathbf{r}),\rho^{\downarrow}(\mathbf{r})\,] = \int \varepsilon_{XC}^{hom}(\rho^{\uparrow}(\mathbf{r}),\rho^{\downarrow}(\mathbf{r}))\rho(\mathbf{r})d^3\mathbf{r} \tag{2.38}$$

$$= \int \left[\varepsilon_X^{hom}\left(\rho^{\uparrow}(\mathbf{r}),\rho^{\downarrow}(\mathbf{r})\right) + \varepsilon_C^{hom}(\rho^{\uparrow}(\mathbf{r}),\rho^{\downarrow}(\mathbf{r}))\right]\rho(\mathbf{r})d^3\mathbf{r} \tag{2.39}$$

Total XC energy is:

$$\varepsilon_{XC}^{hom}(\rho) = \varepsilon_X^{hom}(\rho) + \varepsilon_C^{hom}(\rho) \tag{2.40}$$

Exchange energy per e^- for a homogenous e^- system is given as

$$\varepsilon_X^{hom}(\rho) = -\frac{3}{4}\left(\frac{3}{\pi}\right)^{\frac{1}{3}}\rho(\mathbf{r})^{\frac{1}{3}} \tag{2.41}$$

$$\rho = \left(\frac{4\pi}{3}\mathbf{r}_S\right)^{-1} \tag{2.42}$$

Homogenous correlation energy is difficult to estimate and is done by extremely accurate quantum Monte Carlo simulations [12].

According to LDA, exchange for the homogeneous electron gas having the same density as the location where the exchange is to be estimated.

$$E_{XC}^{LDA}[\rho] = -\frac{3}{4}\left(\frac{3}{\pi}\right)^{\frac{1}{3}}\int \rho(\mathbf{r})^{\frac{4}{3}}d^3\mathbf{r} \tag{2.43}$$

Despite being a very straightforward approximation, LDA has surprisingly produced experimental results for a variety of substances that are not as homogeneous as an electron gas. The LDA overestimates the exchange component and underestimates the correlation component, which can be explained by systematic error cancelling in the solid [13]. LDA has a significant drawback in that it cannot estimate the long-range Vander Waal interactions. Many efforts have been put forward to establish practical formulas to evaluate these interactions [14]. The crystal cohesive and molecule binding energies are both greatly overestimated (by around 20%), and it is unable to adequately characterize a strongly correlated system.

2.2.8.2 Generalised Gradient Approximation (GGA)

To improve the XC energy functional per electron, is to not only include homogeneity of electron density $\rho(\mathbf{r})$ at point $\mathbf{r}$ but also non-homogeneity of electron density [15, 16]. In GGA, XC energy considers local density along with their gradients i.e., $\nabla\rho(\mathbf{r})$. GGA provides more accurate results matching to the experimental data as compared to LDA. Generalized form of XC energy for GGA functional.

$$E_{XC}^{GGA}[\rho^{\uparrow}(\mathbf{r}), \rho^{\downarrow}(\mathbf{r})\,] = \int \varepsilon_{XC}\left(\rho^{\uparrow}(\mathbf{r}), \left|\nabla\rho^{\uparrow}(\mathbf{r})\right|, \rho^{\downarrow}(\mathbf{r}), \left|\nabla\rho^{\downarrow}(\mathbf{r})\right|\right) \rho(\mathbf{r}) d^3\mathbf{r} \quad (2.44)$$

$$= \int \varepsilon_{XC}^{hom}(\rho)\, F_{XC}\left(\rho^{\uparrow}(\mathbf{r}), \left|\nabla\rho^{\uparrow}(\mathbf{r})\right|, \rho^{\downarrow}(\mathbf{r}), \left|\nabla\rho^{\downarrow}(\mathbf{r})\right|\right)\ \rho(\mathbf{r}) d^3\mathbf{r} \quad (2.45)$$

where, F_{XC} is dimensionless and $\varepsilon_{XC}^{hom}(\rho)$ is the XC energy for non-polarized gas.

$$E_{XC}^{GGA}[\rho] = E_X^{GGA}[\rho] + E_C^{GGA}[\rho] \quad (2.46)$$

In which Correlation energy in GGA is given as

$$E_C^{GGA}\left[\rho^{\uparrow}, \rho^{\downarrow}\right] = \int \left\{\varepsilon_C^{hom}(r_s, \zeta) + H(r_s, t, \zeta)\right\} \rho(\mathbf{r}) d^3\mathbf{r} \quad (2.47)$$

Where r_s is the Seitz radius, relative spin polarisation $\zeta = (\rho^{\uparrow} - \rho^{\downarrow})/(\rho^{\uparrow} + \rho^{\downarrow})$, and $\rho = 3/4\pi r_s^3 = k_F^3/3\pi^2$.

$$H(r_s, t, \zeta) = \frac{me^4\phi^3\gamma}{\hbar^2} \ln\left\{1 + \frac{\beta}{\gamma} t^2 \left(\frac{1 + At^2}{1 + At^2 + A^2t^4}\right)\right\} \quad (2.48)$$

$$A = \frac{\beta}{\gamma}\left\{e^{\left(-\frac{\varepsilon_C^{hom}\hbar^2}{\gamma\phi^3 me^4}\right)} - 1\right\}^{-1} \quad (2.49)$$

where dimensionless gradient quantity: $t = \frac{|\nabla\rho|}{2\phi k_s \rho}$, spin scaling factor $\phi(\zeta) = \frac{1}{2}\left[(1+\zeta)^{\frac{2}{3}} + (1-\zeta)^{\frac{2}{3}}\right]$, and Thomas-Fermi screening wave number $k_s = \frac{2e}{\hbar}\sqrt{\frac{k_F m}{\pi}}$ having k_F fermi momentum. β and γ are constant having value 0.066725 ($t \to 0$) and 0.031091 (for uniform density scaling and $\zeta = 0$, $t \to \infty$), respectively.

Exchange energy in GGA for uniform density scaling can be represented as

$$E_X^{GGA}[\rho] = \int \varepsilon_X^{hom}(\rho)\, F_X(s)\, \rho(\mathbf{r}) d^3\mathbf{r} \quad (2.50)$$

GGA has gained attention due to its accurate and average computational results. There are many GGA functional developed so far. Some GGAs are PW91 [17] by Perdew and Wang, PBE [18] by Perdew, Becke and Johnson, RPBE [19] by Hammer et.al, WC [20] by WC and Cohen, PBEsol [21] by Perdew *et al.* $F_X(s)$ in PBE-GGA is given as

$$F_X^{PBE}(s) = 1 + 0.804 - \frac{0.804}{1 + \frac{0.21951}{0.804} s^2} \quad (2.51)$$

Where s is dimensionless density gradient [19] and k_F is fermi momentum.

$$s = \frac{|\nabla\rho(\mathbf{r})|}{2k_F\rho(\mathbf{r})} \quad (2.52)$$

Since GGA functional consider both electron density and its variation over space, this approximation is found to be effective for solid and molecules. But GGA is unable to explain the Vander Waal interactions and it fails for strongly correlated systems.

2.2.8.3 Modified Becke Johnson (mBJ)

Till far we have studied LDA and GGA exchange functional. The vast majority of calculations are evaluated through LDA and GGA as they produce results that are accurate enough to predict experimental data and simultaneously, they follow a cheaper computational approach. LDA is based on the exchange or fermi hole function enthused by the uniform gas model. This model fails to reproduce important features of the exact solution [22, 23]. Later corrections to these models were improved by many authors [23-27] and each of these models suffer inadequacies. The model of Becke [24, 25] allows negative exchange-hole values while Perdew, Ziegler and Tschinke [26, 27, 23] model is analytically discontinuous. The implication of LDA and GGA for studying the electronic behavior of solids is not synchronous with experimental results. It gives value which is severely undervalued or even absent for some cases [28]. In general, the derivative discontinuity (Δ_{XC}) of the XC potential causes the E_g evaluates from the eigen-value spectrum to deviate from the genuine E_g when using an orbital-independent potential [22, 23]. Optimized exchange potential (OEP) technique to exact exchange potential results in better values of bandgap but with strong underestimation and overestimation [24-27]. OEP lies above the slater exchange potential. This discrepancy is solved by Becke and Johnson (BJ) [29] in which slater potential is added to $\Delta V_{X\sigma}$ (correction term to average and actual exchange potential). BJ potential is given as

$$V_{X\sigma}^{BJ} = V_{X\sigma}^{slater} + \Delta V_{X\sigma} \tag{2.53}$$

$$\Delta V_{X\sigma} = \frac{1}{\pi}\sqrt{\frac{5}{12}}\sqrt{\frac{2t_\sigma(\mathbf{r})}{\rho_\sigma(\mathbf{r})}} \tag{2.54}$$

where, electron density, $\rho_\sigma(\mathbf{r}) = \sum_{i=1}^{N}\left|\phi_{i,\sigma}\right|^2$ and K.E density, $t_\sigma(\mathbf{r}) = \frac{1}{2}\sum_{i=1}^{N}\left|\nabla\phi_{i,\sigma}\right|^2$. BJ potential continues to underestimate band gaps, implying that more progress is required. So, Tran and Blaha in 2009 proposed modified BJ (TB-

mBJ) [30] exchange potential which yield more accurate results. mBJ potential uses Becke-Roussel (BR) potential [31] is given as

$$V_{X\sigma}^{BJ} = cV_{X\sigma}^{BR} + (3c - 2)\Delta V_{X\sigma} \tag{2.55}$$

$$V_{X\sigma}^{BR} = -\frac{1}{b_\sigma(\mathbf{r})}\left\{1 - e^{-X_\sigma(\mathbf{r})} - \frac{1}{2}X_\sigma(\mathbf{r})e^{-X_\sigma(\mathbf{r})}\right\} \tag{2.56}$$

$X_\sigma(\mathbf{r})$ is evaluated from electron density and kinetic electronic density and then b_σ form the following equation.

$$b_\sigma(\mathbf{r}) = \sqrt[3]{\frac{X_\sigma^3 e^{-X_\sigma(\mathbf{r})}}{8\pi\rho_\sigma}} \tag{2.57}$$

c is the system-dependent parameter depends on density as follows

$$c = A + B\sqrt{\frac{1}{V_{cell}}\int \frac{1}{2}\left(\frac{|\boldsymbol{\nabla}\rho^{\uparrow}(\mathbf{r})|}{\rho^{\uparrow}(\mathbf{r})} + \frac{|\boldsymbol{\nabla}\rho^{\downarrow}(\mathbf{r})|}{\rho^{\downarrow}(\mathbf{r})}\right) d^3\mathbf{r}} \tag{2.58}$$

Here, V_{cell}; cell volume, A & B; free parameters. TB-mBJ's results are in agreement with the expensive hybrid functional method. Although this method provides more accurate bandgaps for semiconductors and insulators, there are some cases (Cu_2O or itinerant metals) where it didn't perform well. Therefore, Koller *et al.* [32] in 2012 further improve the mBJ potential by reoptimizing parameters A and B and considering position-dependent $c_{loc}(r)$ instead of constant value.

2.2.8.4 Hubbard Approximation U

Hubbard approximation, named after John Hubbard describes the transition between conducting and insulating systems [33]. Hubbard's term is denoted by U which is used in DFT calculations. This term improves the prediction of electron localization and hence correctly predicts the band behavior of Mott insulators. Mott insulators are expected to follow the general criteria of conductors but they are insulators. This happens due to strong electronic-electronic interactions which don't consider in conventional band theories. Mott transition (transition from metal to insulator) is considered in Hubbard model. LDA/GGA/mBJ approximation failed in strongly correlated systems. These materials usually contain rare-earth / transition metal ions in which 3*d* or 4*f* shells are partly occupied. To treat this type of system, orbital-dependent interaction should be considered in addition to LDA/ GGA/mBJ. (DFT+U) [34] is computationally inexpensive in which U (coulomb potential) is applied only to

localized electrons (3*d* or 4*f*). Therefore, for implementation of the above model, localized electrons are separated from non-localized electrons (*s*, *p*) and Hubbard term $\left(\frac{1}{2}\sum_{i\neq j} n_i n_j\,,\ \text{where n is the d orbital occupacies}\right)$ is applied only to localized electrons. Total energy functional within DFT+U method can be expressed as follows

$$E_{total}^{DFT+U}[\rho^{\sigma}, n^{\sigma}] = E_{total}^{DFT}[\rho^{\sigma}] + E^{U}[n^{\sigma}] - E^{dc}[n^{\sigma}] \tag{2.59}$$

$E_{total}^{DFT}[\rho^{\sigma}]$, total energy functional in DFT (LDA/GGA/mBJ). $E^{U}[n^{\sigma}]$ contains $e^{-}e^{-}$ interaction can be given as

$$E^{U}[n^{\sigma}] = \frac{1}{2}\sum_{m,\sigma}\langle m, m''|V_{ee}|m', m'''\rangle n^{\sigma}_{mm'}\ n^{\sigma}_{m''m'''} - (\langle m, m''|V_{ee}|m', m'''\rangle - \langle m, m''|V_{ee}|m''', m'\rangle) n^{\sigma}_{mm'} n^{\sigma}_{m''m'''} \tag{2.60}$$

V_{ee} is the screened coulomb interaction and m and σ represent the magnetic quantum number and spin index for *d* and *f* electrons, respectively. Finally, last term in *equation (2.59)* is written to avoid double counting because of inclusion of Hubbard parameter and $E^{dc}[n^{\sigma}]$ can be written as

$$E^{dc}[n^{\sigma}] = \frac{1}{2}Un(n-1) - \frac{1}{2}J[n^{\uparrow}(n^{\uparrow}-1) + n^{\downarrow}(n^{\downarrow}-1)] \tag{2.61}$$

where J is exchange parameter, $n=n^{\uparrow}+n^{\downarrow}$, and U is screened coulomb potential.

2.2.9 Basis Set

For solving the Schrödinger equation for a single electron in time as proposed Kohn-Sham in *equations (2.31)* and *(2.33)*. We have to perform the last task of choosing basis set $\{f_{\alpha}\}$ for ϕ_i wave function as shown in below equation.

$$\phi_i = \sum_{\alpha} C_{i,\alpha}\, f_{\alpha}(\mathbf{r}) \tag{2.62}$$

The coefficient $C_{i,\alpha}$ can be solved by Raleigh-Ritz variational principle. $f_{\alpha}(\mathbf{r})$ are known functions suggested by many researchers. Some basis sets are linear muffin-tin orbital (LMTO), a linear combination of atomic orbital (LCAO) [35-37], cellular (Wigner-Sitz) method [38], Plane waves basis [39], Pseudopotentials [40], Augmented Plane wave method (APW) [41, 42], linearized APW (LAPW) [36],

APW+ local orbitals (APW+lo) [43], etc. In the present work, we have considered only those methods which are implemented in WIEN2K programming software [44] i.e., APW, LAPW, and APW+lo.

2.2.9.1 APW

APW method was introduced by Slater [42] which separates unit cell space into interstitial region (I) and muffin-tin sphere (MTS) (II) around electron as shown in *Figure 2.1*. ψ is extended as plane wave basis in interstitial region while expanded as spherical harmonics in muffin-tin spheres. For optimal processing efficiency, they are chosen to be as large as possible without overlapping. Since the number of plane waves required to attain convergence increases as the size of MT increases from *sp* to *d* to *f* elements, So, the radius of MT spheres is considered to be 10 to 20% larger for *d* elements than *s-p* elements and even larger for f elements.

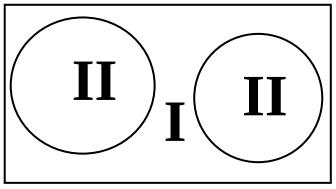

Figure 2. 2: Partitioned space into regions I) interstitial II) MT sphere

Basis function corresponding to these regions are

$$\phi(\mathbf{r},E)=\begin{cases}\frac{1}{\sqrt{\Omega}}\sum_{\mathbf{G}} c_{\mathbf{G}} e^{i(\mathbf{k}+\mathbf{G})} & \mathbf{r} > s_R \\ \sum_{l,m} A_{lm} u_l(r,E_l) Y_{lm}(\hat{r}) & \mathbf{r} \le s_R\end{cases} \tag{2.63}$$

where, **G** and **k** lattice translational and wave vector, respectively, Ω is the unit cell volume, Y_{lm} are spherical harmonics, s_R radius of atomic spheres and u_l are the solutions of radial Schrodinger equation at energy E_l for particular atom.

$$\left\{-\frac{d^2}{dr^2}+\frac{l(l+1)}{r^2}+V(\mathbf{r})-E_l\right\} r u_l(\mathbf{r})=0 \tag{2.64}$$

Coefficients A_{lm} can be determined from boundary condition that ϕ_i is continuous across the MT boundary.

$$A_{lm}=\frac{4\pi i^l}{\sqrt{\Omega}u_l(s_R)}\sum_{\mathbf{G}} c_{\mathbf{G}}\, j_l(|\mathbf{k}+\mathbf{G}|s_R)\, Y_{lm}^*(\mathbf{k}+\mathbf{G}) \tag{2.65}$$

According to the above equation, A_{lm} can be obtained from energy parameter E_l and $c_{\mathbf{G}}$ (Plane wave coefficient). Unfortunately, the APWs are exclusively energy-based solutions inside the spheres. This demonstrates the absence of variational freedom to let wave function changes as the band energy varies from E_l. The) appears $u_l(s_R)$ in the denominator of the expression of A_{lm}, which is an asymptote problem $(1/u_l(s_R))$. For some values of E_l on the sphere boundary, there may be a case where $u_l(s_R)$ is equal to zero. Other than these, the partial waves' slope is discontinuous at the sphere's boundary.

2.2.9.2 LAPW Method

Anderson [37] developed the linearized APW method (LAPW) in 1975 to address problems observed in the APW method. In this method basis function inside MT sphere contains not only $u_l(r, E_l)Y_{lm}(\hat{r})$ but also its derivative and basis function outside MT sphere is identical to the one used in APW method. Basis function in LAPW is presented as

$$\phi(\mathbf{r}, E) = \begin{cases} \frac{1}{\sqrt{\Omega}} \sum_{\mathbf{G}} c_{\mathbf{G}} e^{i(\mathbf{k}+\mathbf{G})} & \mathbf{r} > s_R \\ \sum_{l,m} A_{lm} u_l(\mathbf{r}, E_l) Y_{lm}(\hat{r}) + B_{lm} \dot{u}_l(\mathbf{r}, E_l) Y_{lm}(\hat{r}) & \mathbf{r} \leq s_R \end{cases} \quad (2.66)$$

Where $B_{lm}$are coefficients of energy derivative terms and derivative part $\dot{u}_l(r, E_l)$ satisfy the radial Schrodinger equation

$$\left\{ -\frac{d^2}{dr^2} + \frac{l(l+1)}{r^2} + V(\mathbf{r}) - E_l \right\} \mathbf{r}\dot{u}_l(\mathbf{r}) = \mathbf{r}u_l(\mathbf{r}) \quad (2.67)$$

Now LAPW has extra variational independence inside MT spheres than APW. If E_l differs slightly from band energy, radial function can be determined through following equation.

$$u_l(r, \epsilon) = u_l(r, E_l) + (\epsilon - E_l)\dot{u}_l(r, \epsilon) + O[(\epsilon - E_l)^2] \quad (2.68)$$

The third term gives errors in wavefunction and quadratic of energy difference. Error in band energy will be fourth order difference in energy $(\epsilon - E_l)^4$ which is very small. So, LAPW method gives precise value of energy bands in single diagonalization while APW requires one diagonalization for each band. Asymptote problem is also solved in LAPW. LAPW basis function is more accurate for valence states close to linearization energy E_l i.e., One linearisation energy corresponding to every quantum number l. But it didn't work well in case of semi-core states having quantum number one less than valence states.

2.2.9.3 Local Orbitals

In order to improve linearization energy corresponding to semi-core states, Singh [45] introduced the concept of insertion of local orbitals in LAPW basis. Local orbitals (LO) are independent of wave **k** and lattice translation **G** vector but depend on particular atom with quantum number l. LOs are defined only in MT region but zero in interstitial region and given as

$$\phi_{lm}^{LO}(\mathbf{r}) = \begin{cases} 0 & \mathbf{r} > s_R \\ \sum_{l,m}\{A_{lm}u_l(r,E_{1,l}) + B_{lm}\dot{u}_l(r,E_{1,l}) + C_{lm}u_l(r,E_{2,l})\}Y_{lm}(\hat{r}) & \mathbf{r} \le s_R \end{cases} \quad (2.69)$$

Basis function for LOs consists of two dissimilar energies and one energy derivative. $A_{lm}$and B_{lm} can be derived from normalization of orbital wave function ϕ_{lm}^{LO} and considering its value and slope to be zero at surface boundary S_R. C_{lm} can be fixed to some value. Therefore, LAPW+LO can accurately describe valence electrons and semi-core electrons.

LAPW+LO solves the problem of energy dependence in APW method but it requires large basis set. APW+LO [45] combines the pros of APW and LAPW+LO. Now basis set is of smaller size plus independent of energy. Their corresponding basis function is as follows.

$$\phi_{lm}^{LO}(\mathbf{r}) = \begin{cases} 0 & \mathbf{r} > s_R \\ \sum_{l,m}\{A_{lm}u_l(r,E_{1,l}) + B_{lm}\dot{u}_l(r,E_{1,l})\}Y_{lm}(\hat{r}) & \mathbf{r} \le s_R \end{cases} \quad (2.70)$$

Here, A_{lm} and B_{lm} are independent of **k** and **G**.

2.2.9.4 FP-LAPW

Weinert in 1981 [46] solve the Poisson equation without shape approximation. It is founded on the idea of sphere's boundary value problem and multipole potentials and it efficiently and precisely provides the solution for Poisson equation. Full potential-LAPW method follows the same approach to solve the problem of non-spherical potential. In FP-LAPW, V_{KS} potential and charge density $\rho(\mathbf{r})$ are considered as spherical harmonics times radial functions in MT region and considered as plane-waves in interstitial region.

$$V_{KS}(\mathbf{r}) = \begin{cases} \sum_{lm} V_{lm}(\mathbf{r})\, Y_{lm}(\hat{r}) & \mathbf{r} \le s_R \\ \sum_{\mathbf{G}} V_{\mathbf{G}} e^{i\mathbf{G}\mathbf{r}} & \mathbf{r} > s_R \end{cases} \tag{2.71}$$

$$\rho(\mathbf{r}) = \begin{cases} \sum_{lm} \rho_{lm}(\mathbf{r})\, Y_{lm}(\hat{r}) & \mathbf{r} \le s_R \\ \sum_{\mathbf{G}} \rho_{\mathbf{G}} e^{i\mathbf{G}\mathbf{r}} & \mathbf{r} > s_R \end{cases} \tag{2.72}$$

2.2.9.5 Relativistic Treatment

Relativistic effects can be taken into account for valence states using either a scalar relativistic approach [47] or the second variational method with spin-orbit coupling (SOC) [48, 49]. Core states receive a complete relativistic treatment [50]. SOC is relativistic effect due to spin and orbital angular momentum which results in splitting of energy levels. SOC is more pronounced in heavy elements. Relativistic correction takes place in the region of the atomic sphere, and this effect grows with increasing atomic number. Hamiltonian is:

$$H = -\frac{\hbar^2}{2m}\nabla^2 + V_{eff} + H_{SO} \tag{2.73}$$

$$H_{SO} = \frac{\hbar}{2Mc^2}\frac{1}{\mathbf{r}}\frac{dV}{d\mathbf{r}}\begin{pmatrix} \boldsymbol{\sigma}\mathbf{l} & 0 \\ 0 & 1 \end{pmatrix} \tag{2.74}$$

where $M = m + \frac{(E-V)}{2c^2}$, H_{SO} is the Hamiltonian of spin-orbit and σ is Pauli spin matrix. The inclusion of relativity is different for valence and core electrons. Since dealing with core states are fully relativistic, the one part with which we concern about is valence orbitals. These orbitals are treated with scalar relativistic approximation. In first step, eigenvalue problem is solved on scalar relativistic basis separately for both spin-up and spin-down without considering SOC part but contains all other kinematic parts. In the second step new eigen value problem (with SOC) is solved using eigen functions obtained in the first stage. For evaluating matrix, scalar relativistic Hamiltonian is used and it only contributes to diagonal matrix elements through eigen values. In H_{SO} eigen functions are smaller than the original basis set which leads to eigen value problem of smaller dimension. Second variational method increases the flexibility of calculations by neglecting the matrix elements of H_{SO} between states

differing by more than prescribed energy. Another approach is to choose subset levels from eigenfunctions and apply the effect of SOC within these subsets only.

2.3 LIMITATION OF DFT

DFT is based on computational method for estimating various properties of the materials and widely used in domain of physics, chemistry and materials science. Despite of its wide usage in various field, it has certain limitations.

1. DFT relies on the exchange-correlation functional, which provides an approximation for the unknown electron exchange and correlation energies. There are various exchange-correlation approximations, and no single functional can account for all systems and attributes with equal accuracy. Choosing the ideal functional for a particular system might be difficult.
2. Strongly correlated electron systems, such as transition metal complexes, high-temperature superconductors, and systems with localized electrons, are difficult for DFT to adequately represent. Traditional DFT functionals frequently underestimate the effects of correlation, which results in inaccurate predictions of the properties of magnetism and electronics.
3. Van der Waals interactions, which are critical in systems like molecule adsorption, intermolecular interactions, and multilayer materials, are not fully accounted for by conventional DFT functionals. The binding energies and structures that come from this restriction might be incorrect.
4. DFT frequently makes inaccurate predictions about the electronic characteristics of semiconductors and insulators by underestimating band gaps in these materials. Predictions of optoelectronic characteristics and electronic transport behaviors may be impacted by this problem.
5. DFT computations are typically carried out on materials models with finite sizes. The system's surface energies, adsorption energies, and phonon spectra may be altered as a result of these finite-size effects by artificial interactions between periodic replicas of the system.
6. Calculations for the DFT are normally done at air pressure and zero Kelvin. This limitation restricts the study of materials at finite temperatures and under extreme pressure conditions.

7. DFT frequently has trouble correctly predicting excited states and optical characteristics like spectra of absorption and emission. Although time-dependent DFT (TDDFT) makes an effort to remedy this, the outcomes may still depend on the functionals used.
8. DFT can nonetheless be fairly expensive for big systems or complicated calculations, despite being less computationally taxing than many higher-level quantum chemistry techniques. High-level DFT computations might demand a lot of processing power.

Despite these drawbacks, DFT is nevertheless an effective method for learning about the electronic structure and characteristics of the materials. By utilizing more sophisticated functionals, hybrid techniques, adjustments for dispersion interactions, and fusing DFT results with experimental data, researchers frequently attempt to overcome these constraints.

2.4 WIEN2K

Solving of Kohn-Sham *equation (2.33)* and implementation of above approximations requires computational quantum mechanical approach. The above-mentioned problem is to be solved iteratively as shown in *Figure 2.1*. Present thesis work is performed on WIEN2K software package [16]. WIEN2K programs are written in FORTAN90 and runs on Linux/Unix operating system and have many modules that are connected with scripts of C-shell. The detailed chart of the processes is presented in *Figure 2.3.* FP-LAPW is the basis for calculations in WIEN2K programming [51]. Before initialization of main program, series of small programs run. It started with generation of case.struct file in subdirectory of case. Initialization of the programs started with init_lapw shell script which consists of running SETRTMT (setting RMTs), NN (Calculating nearest neighbour and further determines atomic radius), SGROUP (check space group of the structure), SYMMETRY (creates space group symmetry operations and LM expansion for the lattice harmonics), LSTART (perform atomic calculations and produces free atomic densities), KGEN (k points generation), DSTART (makes a starting density by superposition of free densities generated in LSTART). Self- consistent field started with starting density then LAPW0 calculates total potential from density which consists of coulombic V_C as well as XC potential

V_{XC}. This allows for the setup of the overlap and Hamiltonian matrices. In a DFT computation, the associated eigenvalue problem requires the most work, and k-mesh decides the number of eigenvalue problems is to be solved. LAPW1 calculates valence bands [52], LAPW2 computes a new valence density added with core density generated in LCORE. Output and input density mixed in MIXER and create NEW density [53, 56]. If NEW density matches with the old (input) density SCF is converged and SCF cycle is stopped otherwise it move to next SCF cycle with NEW density.

Below diagram nicely explains the SCF cycle executed within WIEN2K. Simulating big systems on common technology has significantly improved as a result of increased computer power, disc space, and falling costs. Most intensive parts of calculations i.e., LAPW1 and LAPW2 can be run in parallel mode. The programme can be performed in a fine-grain or coarse-grain method. WIEN2K utilizes DFT for investigation of electronic properties of the system. The Full Potential-LAPW approach, which is used to select the basis set, potential, and density, is part of the WIEN2K programming framework. There are certain convergence criteria which need to be fulfilled. Magnitude of largest **K,** K_{MAX} ($|\mathbf{k}+\mathbf{G}|_{MAX}$) and Radius of smallest MT sphere (R_{MT}) and are the two cut-off parameters which governs the convergence of the basis set. So, their multiple ($R_{MT}.K_{MAX}$) is to be set within 6-9 range. The number of angular momenta that can be expanded into spherical harmonics in each MT sphere is capped at $l_{MAX} \approx R_{MT}K_{MAX}$. Since WIEN2k provides the most accurate findings [55], we are motivated to use it to carry out our calculations.

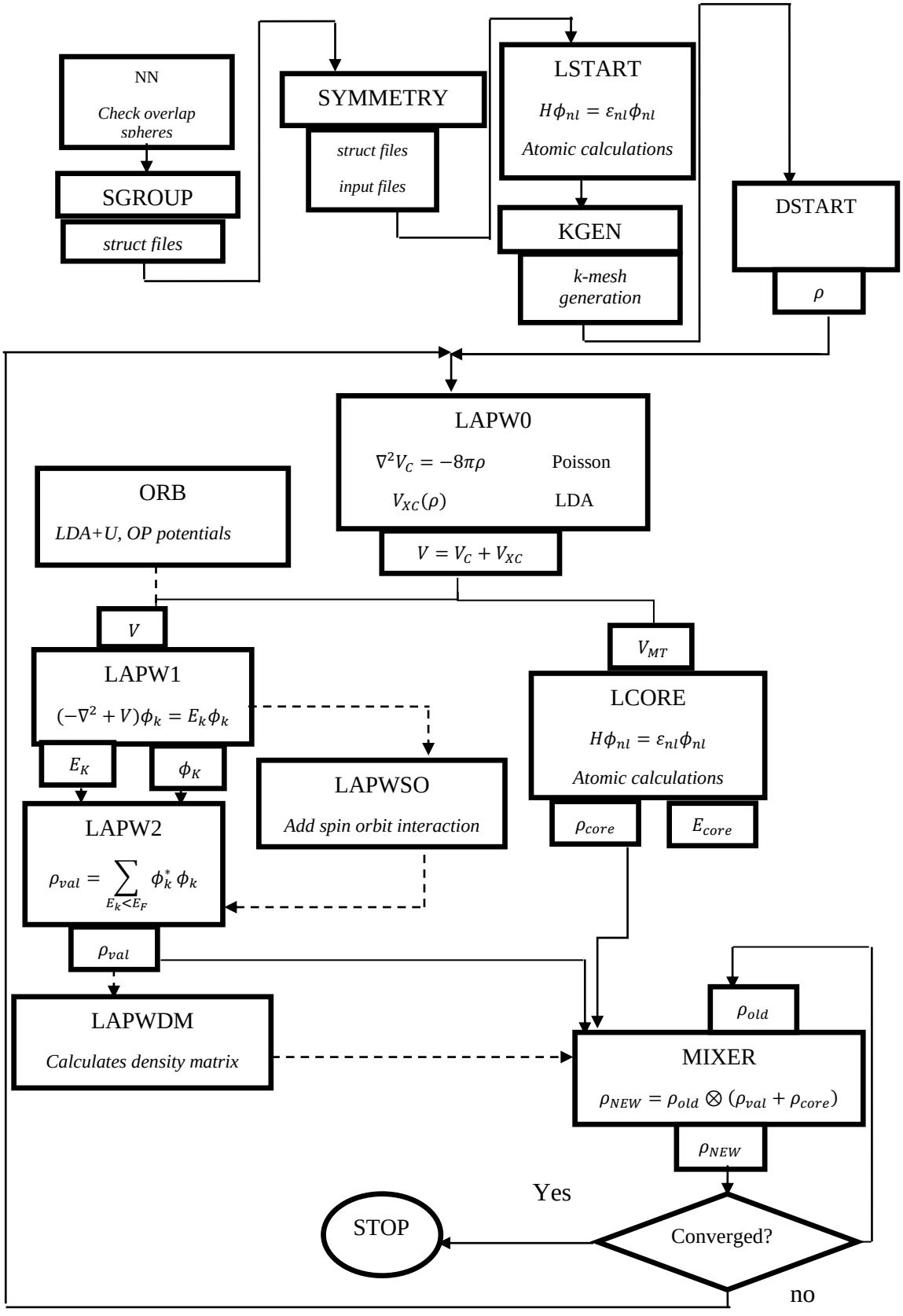

Figure 2.3: Flowchart of programs in WIEN2K

2.5 ELASTIC AND MECHANICAL PROPERTIES

Elastic constants are crucial properties of a material, and accurate methods are needed for their ab initio calculation. As a result, an ab initio method's accuracy in calculating elastic constants acts as an important primary criterion. Elastic constants are essential in describing a material's qualities and demonstrating how it will react to outside forces. The relationship amid large-scale and atomic world is established by these elastic constants. The uses of elastic characteristics in science, medicine, and engineering make understanding them extremely important. There are two different methods to calculate these parameters: first one is stress theorem developed by Neilson [56] and other one is energy-based approach developed by Stadler [57]. For our calculations, we have followed energy-based approach as incorporated in Thomas-Charpin [58] and IR-elast package [59] interfaced with WIEN2K.

In the context of Hooke's law, the energy of strained system by a Taylor series expansion for tiny distortion can be expressed as

$$E(V,\delta) = E(V_o,0) + V_0\left[\sum_{i=1}^{6}\tau_i\delta_i + \frac{1}{2}\sum_{i=1}^{6}\sum_{j=1}^{6}C_{ij}\delta_i\delta_j + O(\delta^3)\right] \tag{2.75}$$

In the above equation, V_0 is the unstrained volume, δ is the small strain provided to an unstrained lattice, τ_i is related to the stress of the cubical system.

2.4.1 Thomas Charpin Package

The elastic parameters are evaluated using the well-known Hooke's law wherein strain and stress are directly associated with each other through elasticity constant. In case of cubical system, exist elastic constants are C_{11}, C_{12}, and C_{44}. To obtain these parameters strain method is used in which a small strain is provided into an unstrained lattice.

Three different distortions are imposed for evaluating C_{11}, C_{12}, and C_{44}. These strains and distortions include the volume-conserving tetragonal, equation of state (eos) and rhombohedral strain. Thomas Charpin [58] asserts that the initial step employs the equation of state to calculate $C_{11} + 2C_{12}$ and additional bulk modulus (B).

$$C_{11} + 2C_{12} = 3B \tag{2.76}$$

Volume conservative tetragonal strain as follows:

$$\begin{bmatrix} \delta & 0 & 0 \\ 0 & \delta & 0 \\ 0 & 0 & \frac{1}{(1+\delta)^2} - 1 \end{bmatrix} \tag{2.77}$$

where, $\delta = (1+\tau)^{-\frac{1}{3}} - 1$, τ is the strain tensor. Energy expression due to tetragonal strain tensor

$$\mathrm{E}(\delta) = \mathrm{E}(0) + 3(\mathrm{C}_{11} - \mathrm{C}_{12}) + \mathrm{V}_0\delta^2 + \mathrm{O}(\delta^3) \tag{2.78}$$

Volume conservative rhombohedral strain tensor is as follows:

$$\delta \begin{bmatrix} 1 & 1 & 1 \\ 1 & 1 & 1 \\ 1 & 1 & 1 \end{bmatrix} \tag{2.79}$$

which transforms the total energy to

$$\mathrm{E}(\delta) = \mathrm{E}(0) + \frac{1}{6}(\mathrm{C}_{11} + 2\mathrm{C}_{12} + 4\mathrm{C}_{44}) + \mathrm{V}_0\delta^2 + \mathrm{O}(\delta^2) \tag{2.80}$$

The elastic constant C_{44} is evaluated through rhombohedral strain

$$C_{44} = \frac{1}{4}\left(\frac{3}{2V_o}\frac{d^2E}{d\delta^2}\bigg|_{\delta=0} - C_{11} - 2C_{12}\right) = \frac{1}{4}\left(\frac{3}{2V_o}\frac{d^2E}{d\delta^2}\bigg|_{\delta=0} - 3B\right) \tag{2.81}$$

If we use the *equation (2.76)* to drive elastic constants, errors in calculating B using an eos added to calculations of elastic constants may accumulate. However, in IRelast package calculates elastic constants by Taylor series expansion without applying the aforementioned relation. As a result, these errors are not included in the results. As a result, refer to the calculations as zero-bulk errors.

2.4.2 IR-elast Package

According to *equation (2.75)*, elastic constants can be determined by taking double derivative of polynomial fit $\mathrm{E}(\mathrm{V}, \delta)$ at zero strain.

$$\mathrm{C}_{ij} = \frac{1}{\mathrm{V}_0}\left[\frac{\partial^2 \mathrm{E}}{\partial\delta_i\delta_j}\right]_{\delta=0} \tag{2.82}$$

In a 3 x 3 matrix, R is a lattice vector of unstrained cubical system, and I is the identity matrix. So, lattice vector in strained system can be defined as

$$\mathrm{R}' = \mathrm{R} \times \mathrm{D} \tag{2.83}$$

where, D is the deformed matrix for a small stain δ i.e., $\mathrm{D} = \mathrm{I} + \delta$.

$$D = \begin{pmatrix} 1+\delta_{xx} & \frac{\delta_{xy}}{2} & \frac{\delta_{xz}}{2} \\ \frac{\delta_{yx}}{2} & 1+\delta_{yy} & \frac{\delta_{yz}}{2} \\ \frac{\delta_{zx}}{2} & \frac{\delta_{zy}}{2} & 1+\delta_{zz} \end{pmatrix} \quad (2.84)$$

x, y, and z are the cartesian indices. Voigt notation is frequently useful when attempting to minimize the number of indices. Voigt notation replaces xx, yy, zz with 1, 2, 3, respectively and xy (and yx) as 4, zy (and yz) as 5 and zx (and xz) as 6. So, D can be rewritten as

$$D = \begin{pmatrix} 1+\delta_1 & \frac{\delta_4}{2} & \frac{\delta_6}{2} \\ \frac{\delta_4}{2} & 1+\delta_2 & \frac{\delta_5}{2} \\ \frac{\delta_6}{2} & \frac{\delta_5}{2} & 1+\delta_3 \end{pmatrix} \quad (2.85)$$

IR elast package calculates the cubical elastic constants C_{11}, C_{12}, and C_{44}, by providing three different strained (D_1, D_2, D_3) to the lattice. Volume conserving orthorhombic distortion D_1 is given as

$$D_1 = \begin{pmatrix} 1+\delta & 0 & 0 \\ 0 & 1-\delta & 0 \\ 0 & 0 & \frac{1}{1-\delta^2} \end{pmatrix} \quad (2.86)$$

Lattice parameter in a- direction is changed by D_2 is given as

$$D_2 = \begin{pmatrix} 1+\delta & 0 & 0 \\ 0 & 1+\delta & 0 \\ 0 & 0 & 1+\delta \end{pmatrix} \quad (2.87)$$

And D_3, volume conserving monoclinic distortion is

$$D_3 = \begin{pmatrix} 1 & \delta & 0 \\ \delta & 1 & 0 \\ 0 & 0 & \frac{1}{1-\delta^2} \end{pmatrix} \quad (2.88)$$

And energy corresponding to these distortions, respectively, are as follows

$$E(V,\delta) = E(V_o,0) + V_0[(C_{11}-C_{12})\delta^2 + O(\delta^4)] \quad (2.89)$$

$$E(V,\delta) = E(V_o,0) + V_0\left[(\tau_1+\tau_2+\tau_3)\delta + \frac{3}{2}(C_{11}+2C_{12})\delta^2 + O(\delta^3)\right] \quad (2.90)$$

$$E(V,\delta) = E(V_o,0) + V_0[2C_{44}\delta^2 + O(\delta^4)] \quad (2.91)$$

2.4.3 Mechanical Properties

Elastic parameters are used to estimate mechanical parameters like young (*Y*), shear (*G*), bulk (*B*) modulus, Anisotropy (*A*), Poisson ratio (*v*), and Debye temperature (θ_D). Using Hill's average scheme [60] consists of average of Voigt [61] and Reuss [62], these mechanical parameters are given in the following equations. The stiffness of the material is described by the shear modulus defined in equations (2.93 to 2.95), where according to the Hills, *G*, G_V, and G_R are the average, Voigt, and Reuss shear modulus, respectively.

$$G_V = \frac{1}{5}(C_{11} - C_{12} + 3\, C_{44}) \tag{2.92}$$

$$G_R = \frac{5(C_{11} - C_{12})\, C_{44}}{3(C_{11} - C_{12}) + 4\, C_{44}} \tag{2.93}$$

$$G = \frac{G_V + G_R}{2} \tag{2.94}$$

The bulk modulus relation given in equation (2.95) relates to how much the material is resistive to the change in the volume, while young's modulus depends on *B* and *G* according to equation (2.96).

$$B = B_V = B_R = \frac{C_{11} + 2\, C_{12}}{3} \tag{2.95}$$

$$Y = \frac{9BG}{(3B + G)} \tag{2.96}$$

$$\nu = \frac{3\, B - 2\, G}{2\, (3\, B + G)} \tag{2.97}$$

$$A = \frac{2C_{44}}{C_{11} - C_{12}} \tag{2.98}$$

Xing Liu *et al.* [63] have proposed the possibility of computation of θ_D using mechanical parameters. It reflects thermodynamic properties and their association with parameters like specific heat, longitudinal velocity, transverse velocity, and the thermal expansion coefficient of the solids.

$$\theta_D = \frac{h}{K_B}\left[\frac{3q}{4\pi V_a} \right]^{\frac{1}{3}} v_m \tag{2.99}$$

$$v_m = \left[\frac{1}{3}\left(\frac{2}{{v_t}^3} + \frac{1}{{v_l}^3} \right) \right]^{-\frac{1}{3}} \tag{2.100}$$

$$v_t = \left(\frac{G}{\rho}\right)^{\frac{1}{2}} \tag{2.101}$$

$$v_l = \left(\frac{3B + 4G}{3\rho}\right)^{\frac{1}{2}} \tag{2.102}$$

Debye temperature's equation comprises Planck's constant (h), number of elements in the compound (q), Boltzmann's constant (K_B), density (ρ), the atomic volume of a unit cell (V_a), transverse (v_t), average (v_m), and longitudinal sound velocity (v_l).

2.6 THERMODYNAMIC PROPERTIES

In the present thesis, thermodynamic behaviour of the solids has been studied by implementation of Quasi-Harmonic Debye (QHD) model as incorporated in Gibbs programming [64-66]. Thermodynamic results obtained from the QHD at low and intermediate temperature are quite reliable. Gibbs free energy ($G^*(V;P,T)$) determines how a solid behaves in terms of its geometry and phase stability at a specific pressure and temperature. $G^*(V;P,T)$ has been minimised corresponding to volume (V) at constant temperature (T) and pressure (P).

$$\left[\frac{\partial G^*(V;P,T)}{\partial V}\right]_{P,T} = 0 \tag{2.103}$$

By solving above equation, thermal eos can be obtained.

$$G^*(V;P,T) = F_{Vib}(\theta_D(V);T) + P(V) + E(V) \tag{2.104}$$

where θ_D is Debye temperature and E is total energy. F_{Vib}, vibrational Helmholtz free energy given as

$$F_{Vib}(\theta_D(V);T) = NK_BT\left[\frac{9\theta_D}{8T} + 3\ln\left(1 - e^{-\frac{\theta_D}{T}}\right) - D\left(\frac{\theta_D}{T}\right)\right] \tag{2.105}$$

$$D(y) = \frac{3}{y^3}\int_0^y \frac{z^3}{e^z - 1}\, dz \tag{2.106}$$

where $D\left(\frac{\theta_D}{T}\right)$ is Debye integral and K_B is the Boltzmann's constant.

The expression presented θ_D given below

$$\theta_D = \frac{h}{k}\sqrt{\frac{B_s}{M}}\left[6\pi^2 V^{1/2} n\right]^{1/3} f(\nu) \tag{2.107}$$

where M is molecular mass, ν is Poisson's ratio and B_S is adiabatic bulk modulus. The adiabatic bulk modulus has been approximated as,

$$B_s \approx B(V) = V\left(\frac{d^2E(V)}{dV^2}\right) \tag{2.108}$$

The function f(ν) is defined as,

$$f(\nu) = \left\{3\left[2\left(\frac{2}{3}\frac{1+\nu}{1-2\nu}\right)^{3/2} + \left(\frac{1}{3}\frac{(1+\nu)}{(1-\nu)}\right)^{3/2}\right]^{-1}\right\}^{1/3} \tag{2.109}$$

The isothermal bulk modulus (B_T), heat capacity at constant volume (C_V), entropy (S), Grüneisen constant (γ) and thermal expansion coefficient (α) are then calculated using the standard thermodynamic relations shown below.

$$B_T(p,T) = \left[V\left(\frac{\partial^2 G^*(V;p,T)}{\partial V^2}\right)_{p,T}\right]_{V_{opt(p,T)}} \tag{2.110}$$

$$C_V = 3nK_B\left(4D\left(\frac{\theta_D}{T}\right) - \frac{3\theta_D/T}{e^{\frac{\theta_D}{T}} - 1}\right) \tag{2.111}$$

$$S = 3nK_B\left(4D\left(\frac{\theta_D}{T}\right) - 3\ln\left(1 - e^{\frac{-\theta_D}{T}}\right)\right) \tag{2.112}$$

$$\gamma = \frac{d\ln\theta_D}{d\ln V} \tag{2.113}$$

$$\alpha = \frac{\gamma C_V}{B_T V} \tag{2.114}$$

2.7 THERMOELECTRIC PROPERTIES

In the search for thermoelectric (TE) materials, estimation of thermoelectric behaviour of the compounds is necessary. TE materials are advantageous in generation of electricity and air conditioning. TE technology is long-lived and environment-friendly. TE power generator converts waste heat into electricity. The effectiveness of converting heat to voltage and vice versa can be measured by a dimensionless factor, which also has extremely low thermal conductivity (κ) and extremely high electrical conductivity (σ). This factor is named as Figure of merit denoted as *ZT* and mathematically written as

$$ZT = \frac{\mathcal{S}^2\sigma}{\kappa} \tag{2.115}$$

In the above equation, $\mathcal{S}$ is known as Seebeck coefficient. Thermal conductivity refers to the material's ability for heat conduction due to electrons as well as phonons (lattice vibrations). Thermal conductivity due to electron and lattice vibration is represented as κ_e and κ_l. So,

$$\kappa = \kappa_e + \kappa_l \tag{2.116}$$

Parameters such as $\mathcal{S}$, κ_e, σ are calculated using Boltzmann transport theory (BTT) [67-69] via BoltzTrap code [70] and κ_l via Slack method [71-73].

2.6.1 Boltzmann Transport Theory

BTT can establish relation between macroscopic and microscopic world. Macroscopic quantities like diffusion coefficient, mobility, conductivity can be derived from microscopic model. For understanding of transport characteristics of materials, distribution function of an electron gas must be known. The distribution would provide information on how electrons are dispersed in momentum space and energy space, allowing us to analyse all of the transport aspects. We are aware that the distribution function is just the Fermi-Dirac (FD) function at equilibrium. FD function for electron in state k with energy ϵ_k is as follows

$$f_k^0 = \frac{1}{1 + e^{\frac{\epsilon_k - \mu}{K_B T}}} \tag{2.117}$$

where μ is chemical potential. The Boltzmann theory starts by attempting to ascertain how $f_k^0(\mathbf{r})$ varies over time. The alteration in the electron distribution in **k**-space (**k** is wave vector) and **r**-space (**r** is position vector) can be attributed to three different factors.

1. Diffusion of electrons by temperature or gradients.

2. influence of external field given as $\mathbf{F}_{\text{ext}} = \hbar \frac{\partial \mathbf{k}}{\partial t}$.

3. Scattering of electrons due to lattice defects as they move from one k state to other.

Partial time derivative of FD function

$$\frac{\partial f}{\partial t} = \left(\frac{\partial f}{\partial t}\right)_{\text{diffusion}} + \left(\frac{\partial f}{\partial t}\right)_{\text{external field}} + \left(\frac{\partial f}{\partial t}\right)_{\text{scattering}} \tag{2.118}$$

When an electron is subjected to external field, it will change its state from (**r**, **k**, t) to (**r**-**v**dt, **k**-**k̇**dt, t-dt); **v** is velocity of carrier, then diffusion and acceleration of electron take place. This is drift term, expressed in the following equation.

$$\left(\frac{\partial f}{\partial t}\right)_{drift} = \frac{f(\mathbf{r} - \mathbf{v}dt, \mathbf{k} - \dot{\mathbf{k}}dt, t - dt)}{dt} - \frac{f(\mathbf{r}, \mathbf{k}, t)}{dt} \tag{2.119}$$

Using Taylor expansion first term is as follows

$$f(\mathbf{r} - \mathbf{v}dt, \mathbf{k} - \dot{\mathbf{k}}dt, t - dt) = f(\mathbf{r}, \mathbf{k}, t) - \left(\dot{\mathbf{k}}\frac{\partial f}{\partial \mathbf{k}} + \mathbf{v}\frac{\partial f}{\partial \mathbf{r}} + \frac{\partial f}{\partial t}\right)dt \tag{2.120}$$

Putting above equation in (2.120)

$$\left(\frac{\partial f}{\partial t}\right)_{drift} = -\left[\frac{1}{\hbar}(\mathbf{F_{ext}}.\nabla_k f) + \mathbf{v}.\nabla_r f + \frac{\partial f}{\partial t}\right] \tag{2.121}$$

Under steady state conditions there is no net change in distribution. So (2.119) is equal to zero. Therefore,

$$\left(\frac{\partial f}{\partial t}\right)_{drift} = \left(\frac{\partial f}{\partial t}\right)_{scattering} \tag{2.122}$$

Further,

$$\frac{\partial f}{\partial t} = -\frac{1}{\hbar}(\mathbf{F_{ext}}.\nabla_k f) - \mathbf{v}.\nabla_r f + \left(\frac{\partial f}{\partial t}\right)_{scattering} \tag{2.123}$$

The above equation is known as Boltzmann transport equation (BTE). First term related to the variation of distribution function with momentum. Second term here is diffusion term which will become zero when distribution function is spatially homogenous. Last term is related to probability of electron scattering which make BTE solution difficult. Next step is to simplify the scattering (collision) part using relaxation time approximation (RTA).

The system will become out of equilibrium if an external force is introduced. The collision term will result in scattering events that bring the system back to equilibrium if this external force is eliminated. The collision term is considered to have the following shape in the RTA.

$$\left(\frac{\partial f}{\partial t}\right)_{scattering} = \frac{f_0(\mathbf{k}) - f(\mathbf{k})}{\tau(\mathbf{k})} \tag{2.124}$$

where, τ is the collision time and non-equilibrium distribution function $f(\mathbf{k})$ relaxes to the local equilibrium distribution function $f_0(\mathbf{k})$ over the time scale τ. Therefore equation (2.124) becomes

$$\frac{\partial f}{\partial t} = -\frac{1}{\hbar}(\mathbf{F_{ext}}.\nabla_k f) - \mathbf{v}.\nabla_r f + \frac{f_0(\mathbf{k}) - f(\mathbf{k})}{\tau(\mathbf{k})} \tag{2.125}$$

In fact, a system returning to equilibrium from a steady but non-equilibrium state (t = 0) will meet the following equation in the absence of any outside forces.

$$\frac{\partial f}{\partial t} = -\frac{f(\mathbf{k}) - f_0(\mathbf{k})}{\tau(\mathbf{k})} \tag{2.126}$$

Adding f_0 in the derivative (since $\frac{\partial f_0}{\partial t} = 0$) above equation reduces to

$$\frac{\partial(f(\mathbf{k}) - f_0(\mathbf{k}))}{\partial t} = -\frac{f(\mathbf{k}) - f_0(\mathbf{k})}{\tau(\mathbf{k})} \tag{2.127}$$

Solution of the above differential equation is as follows

$$f(\mathbf{k}, \mathbf{t}) = f_0(\mathbf{k}) + \ (f(\mathbf{k}, 0) - f_0(\mathbf{k}))e^{-\frac{t}{\tau(\mathbf{k})}} \tag{2.128}$$

2.6.2 Transport Coefficients

Evaluation of thermoelectric parameters is necessary for understanding the thermoelectric behaviour of the material. Electric current J_i, in the presence of thermal gradient ΔT, electric field **E** and magnetic field **B** is presented as

$$J_i = \sigma_{ij}E_j + \vartheta_{ij}\nabla_j T + \sigma_{ijk}E_j B_k + \cdots \tag{2.129}$$

$$\vartheta_{ij} = \mathcal{S}_{i\alpha}\sigma_{\alpha j} \tag{2.130}$$

$\sigma_{\alpha j}$ and $\mathcal{S}_{i\alpha}$ are electrical conductivity and Seebeck coefficient, respectively.

At microscopic level, electric density is as follows

$$J = e\sum_{\mathbf{k}} f(\mathbf{k})\nu(\mathbf{k}) \tag{2.131}$$

group velocity $\nu(\mathbf{k}) = \frac{1}{\hbar}\frac{\partial \epsilon_{\mathbf{k}}}{\partial \mathbf{k}}$. In the absence of magnetic field and thermal gradient, under stationary state distribution function is given as

$$f(\mathbf{k}) = f_0(\mathbf{k}) + e\left(-\frac{\partial f_0}{\partial \epsilon}\right)\tau(\mathbf{k})\nu(\mathbf{k}).\mathbf{E} \tag{2.132}$$

Putting above equation in J term

$$J = e\sum_{\mathbf{k}} f_0(\mathbf{k})\nu(\mathbf{k}) + e^2\sum_{\mathbf{k}}\left(-\frac{\partial f_0}{\partial \epsilon}\right)\tau(\mathbf{k})\nu(\mathbf{k})\nu(\mathbf{k}).\mathbf{E} \tag{2.133}$$

By comparing equations (2.130) and (2.133), we get conductivity as

$$\sigma(\mathbf{k})_{=} e^2\sum_{\mathbf{k}}\left(-\frac{\partial f_0}{\partial \epsilon}\right)\tau(\mathbf{k})\nu(\mathbf{k})\nu(\mathbf{k}) \tag{2.134}$$

$$\sigma(\mathbf{k})_{=}\sum_{\mathbf{k}}\left(-\frac{\partial f_0}{\partial \epsilon}\right)\sigma(\mathbf{k}) \tag{2.135}$$

Conductivity tensors having a specific energy $\boldsymbol{\epsilon}$ is presented as

$$\sigma_{\alpha\beta}(\epsilon) = \frac{1}{N}\sum_{i,\mathbf{k}}\sigma_{\alpha\beta}(i.\mathbf{k})\frac{\delta(\epsilon - \epsilon_{i.\mathbf{k}})}{d\epsilon} \tag{2.136}$$

N, number of **k** points sampled. Thermoelectric coefficients in a unit cell volume Ω are calculated through the integration of conductivity distribution over chemical potential μ and *T*.

$$\sigma_{\alpha\beta}(T;\mu) = \frac{1}{\Omega}\int \sigma_{\alpha\beta}(\epsilon)\left(-\frac{\partial f_{\mu}(T;\epsilon)}{\partial\epsilon}\right)d\epsilon \tag{2.137}$$

$$\vartheta_{\alpha\beta}(T;\mu) = \frac{1}{e\Omega T}\int \sigma_{\alpha\beta}(\epsilon)(\epsilon-\mu)\left(-\frac{\partial f_{\mu}(T;\epsilon)}{\partial\epsilon}\right)d\epsilon \tag{2.138}$$

$$\mathcal{S}_{\alpha\beta} = (\sigma^{-1})_{i\alpha}\vartheta_{j\beta} \tag{2.139}$$

$$\kappa^{0}_{\alpha\beta}(T;\mu) = \frac{1}{e^{2}\Omega T}\int \sigma_{\alpha\beta}(\epsilon)(\epsilon-\mu)^{2}\left(-\frac{\partial f_{\mu}(T;\epsilon)}{\partial\epsilon}\right)d\epsilon \tag{2.140}$$

$\kappa^{0}_{\alpha\beta}(T;\mu)$ is the electronic thermal conductivity.

Boltztrap code is used for evaluating transport coefficient of the materials. This code uses Fourier expansion of BTE under constant RTA. The necessary derivatives are computed using the interpolated band structure to assess transport qualities.

2.6.3 Lattice Thermal Conductivity

Lattice thermal conductivity refers to the ability of a solid to conduct heat through the vibration of its lattice ions. Lattice thermal conductivity κ_l is evaluated through the Slack model [71]. A high *ZT* contributes to an extremely low κ_l. Slack provides the model to find out the κ_L using Debye temperature and Grüneisen parameter γ.

$$\kappa_l = \frac{0.849\times 3\sqrt[3]{4}}{20\pi^{3}\left(1-\frac{0.514}{\gamma}+\frac{0.228}{\gamma^{2}}\right)}\left(\frac{K_B\theta_D}{\hbar}\right)^{3}\frac{\overline{M}\,\delta}{\gamma^{2}Tn^{\frac{2}{3}}} \tag{2.141}$$

$$\kappa_l = A_{\gamma}\frac{\overline{M}\,\delta{\theta_D}^{3}}{\gamma^{2}Tn^{\frac{2}{3}}} \tag{2.142}$$

$$A_{\gamma} = \frac{2.43\times 10^{-8}}{1-\frac{0.514}{\gamma}+\frac{0.228}{\gamma^{2}}} \tag{2.143}$$

Above equations [71-74] represent the formula for the estimation of κ_l (in $Wcm^{-1}K^{-1}$), which consists of $\overline{M}$, average atomic mass (in a.m.u), δ^3, volume per atom (in Å). A_γ is related to the Grüneisen parameter expressed in Eq. 20, given by Julian [72] and later modified by Leibfried and Schlomann [73].

REFERENCES

1. Hohenberg, P., and Kohn, W. "Inhomogeneous electron gas." *Phys. Rev*. 136 (1964): B864.
2. Steckel, J.A. and Sholl, D. *Density Functional Theory*. John Wiley & Sons, Ltd, Hoboken, 2009.
3. Fermi, E. "Statistical method to determine some properties of atoms." *Rend. Accad. Naz. Lincei* 6, no. 602-607 (1927): 5.
4. Thomas, L.H. "The calculation of atomic fields." *In Mathematical proceedings of the Cambridge philosophical society*, vol. 23, no. 5, pp. 542-548. Cambridge University Press, 1927.
5. Kohn, W., and Sham, J.L. "Self-consistent equations including exchange and correlation effects." *Physical Review* 140, no. 4A (1965): A1133.
6. Slater, J.C. *Quantum theory of atomic structure*. No. 530.12 S53. 1960.
7. Born, M., and Oppenheimer, R. "On the quantum theory of molecules." *In Quantum Chemistry: Classic Scientific Papers*, pp. 1-24. 2000.
8. March, N.H. Self-Consistent Fields in Atoms (*Pergamon Press* 1975).
9. Slater, J.C. "Wave Functions in a Periodic Potential", *Phys. Rev*., 51 (1937): 846-851.
10. Slater, J.C. "Quantum Theory of Molecular and Solids." *The self-Consistent Field for Molecular and solids* 4 (1974).
11. Slater, J.C. "A Simplification of the Hartree-Fock Method", *Phys. Rev* 81 (1951): 385-390.
12. Ortiz, G. and Ballone, P. "Correlation energy, structure factor, radial distribution function, and momentum distribution of the spin-polarized uniform electron gas." *Physical Review B* 50 (1994): 1391-1405.
13. Vosko, S.H., Wilk, L. and Nusair, M. "Accurate spin-dependent electron liquid correlation energies for local spin density calculations: a critical analysis." *Canadian Journal of Physics* 58 (1980): 1200-1211.
14. Dobson, J.F., White, A. and Rubio, A. "Asymptotics of the dispersion interaction: analytic benchmarks for van der Waals energy functionals." *Physical Review Letters* 96, no. 7 (2006): 073201.

15. Jones, R.O. "Introduction to density functional theory and exchange-correlation energy functionals." *Computational Nanoscience: Do It Yourself* 31 (2006): 45-70.
16. Blaha, P., Schwarz, K., Tran, F., Laskowski, R., Madsen, G.K. and Marks, L.D. "WIEN2k: An APW+ lo program for calculating the properties of solids." *The Journal of Chemical Physics* 152, no. 7 (2020): 074101.
17. Perdew, J.P. and Wang, Y. "Accurate and simple analytic representation of the electron-gas correlation energy." *Physical Review B* 45, no. 23 (1992): 13244.
18. Perdew, J.P., Burke, K. and Ernzerhof, M. "Generalized gradient approximation made simple." *Physical Review Letters* 77, no. 18 (1996): 3865.
19. Hammer, B.H.L.B., Hansen, L.B. and Nørskov, J.K. "Improved adsorption energetics within density-functional theory using revised Perdew-Burke-Ernzerhof functionals." *Physical Review B* 59, no. 11 (1999): 7413.
20. Wu, Z. and Cohen, R.E. "More accurate generalized gradient approximation for solids." *Physical Review B* 73, no. 23 (2006): 235116.
21. Perdew, J.P., Ruzsinszky, A., Csonka, G.I., Vydrov, O.A., Scuseria, G.E., Constantin, L.A., Zhou, X. and Burke, K. "Restoring the density-gradient expansion for exchange in solids and surfaces." *Physical Review Letters* 100, no. 13 (2008): 136406.
22. Sahni, V., Bohnen, K.P. and Harbola, M.K. "Analysis of the local-density approximation of density-functional theory." *Physical Review A* 37, no. 6 (1988): 1895.
23. Tschinke, V. and Ziegler, T. "On the shape of spherically averaged Fermi-hole correlation functions in density functional theory. 1. Atomic systems." *Canadian Journal of Chemistry* 67, no. 3 (1989): 460-472.
24. Becke, A. D. "Hartree–Fock exchange energy of an inhomogeneous electron gas." *International Journal of Quantum Chemistry* 23, no. 6 (1983): 1915-1922.
25. Becke, A. D. "On the large-gradient behavior of the density functional exchange energy." *The Journal of Chemical Physics* 85, no. 12 (1986): 7184-7187.
26. Perdew, J.P. "Accurate density functional for the energy: Real-space cutoff of the gradient expansion for the exchange hole." *Physical Review Letters* 55, no. 16 (1985): 1665.

27. Perdew, J.P. "Density-functional approximation for the correlation energy of the inhomogeneous electron gas." *Physical Review B* 33, no. 12 (1986): 8822.
28. Heyd, J., Peralta, J.E., Scuseria, G.E. and Martin, R.L. "Energy band gaps and lattice parameters evaluated with the Heyd-Scuseria-Ernzerhof screened hybrid functional." *The Journal of Chemical Physics* 123, no. 17 (2005): 174101.
29. Becke, A.D. and Johnson, E.R. "A simple effective potential for exchange." *The Journal of Chemical Physics* 124, no. 22 (2006): 221101.
30. Tran, F. and Blaha, P. "Accurate band gaps of semiconductors and insulators with a semilocal exchange-correlation potential." *Physical Review Letters* 102, no. 22 (2009): 226401.
31. Becke, A.D., and Roussel, M.R. "Exchange holes in inhomogeneous systems: A coordinate-space model." *Physical Review A* 39, no. 8 (1989): 3761.
32. Koller, D, Tran, F. and Blaha P. "Improving the modified Becke-Johnson exchange potential." *Physical Review B* 85, no. 15 (2012): 155109.
33. Hubbard, J. "Electron correlations in narrow energy bands." *Proceedings of the Royal Society of London. Series A. Mathematical and Physical Sciences* 276, no. 1365 (1963): 238-257.
34. Anisimov, V.I., Aryasetiawan, F. and Lichtenstein, A.I. "First-principles calculations of the electronic structure and spectra of strongly correlated systems: the LDA+ U method." *Journal of Physics: Condensed Matter* 9, no. 4 (1997): 767.
35. Bloch, F. "Quantum mechanics of electrons in crystal lattices." *Z. Phys* 52 (1928): 555-600.
36. Andersen, O.K. "Linear methods in band theory." *Physical Review B* 12, no. 8 (1975): 3060.
37. Andersen, O.K., and Jepsen, O. "Explicit, first-principles tight-binding theory." *Physical Review Letters* 53, no. 27 (1984): 2571.
38. Wigner, Eugene, and Frederick Seitz. "On the constitution of metallic sodium." Physical Review 43, no. 10 (1933): 804.
39. Ashcroft, Neil W., and N. David Mermin. "Solid state physics (brooks cole, 1976)."

40. Phillips, J.C., and Kleinman, L. "New method for calculating wave functions in crystals and molecules." *Physical Review* 116, no. 2 (1959): 287.
41. Slater, J.C. "Wave functions in a periodic potential." *Physical Review* 51, no. 10 (1937): 846.
42. Loucks, T.L. “Augmented plane wave method: a guide to performing electronic structure calculations.” 28 WA Benjamin, 1967.
43. Sjöstedt, E., Nordström, L. and Singh, D.J. "An alternative way of linearizing the augmented plane-wave method." *Solid state communications* 114, no. 1 (2000): 15-20.
44. Madsen, G.K.H., Blaha, P., Schwarz, K., Sjöstedt, E. and Nordström, L. “Efficient linearization of the augmented plane-wave method”, *Physical Review B*, 64 (2001) 195134.
45. Singh, D.J., and Nordström, L. “Planewaves, Pseudopotentials, and the LAPW Method”, 2nd ed. (Springer, New York, 2006).
46. Weinert, M. "Solution of Poisson’s equation: Beyond Ewald-type methods." *Journal of Mathematical Physics* 22, no. 11 (1981): 2433-2439.
47. Koelling, D. D., and Harmon, B.N. "A technique for relativistic spin-polarised calculations." *Journal of Physics C: Solid State Physics* 10, no. 16 (1977): 3107.
48. MacDonald, A. H., Picket, W.E., and Koelling, D.D. "A linearised relativistic augmented-plane-wave method utilising approximate pure spin basis functions." *Journal of Physics C: Solid State Physics* 13, no. 14 (1980): 2675.
49. Novák, P. "Calculation of spin-orbit coupling." (1997).
50. Desclaux, J. P. "Hartree Fock Slater self consistent field calculations." *Computer Physics Communications* 1, no. 3 (1970): 216-222.
51. Marder, M. P. Condensed matter physics. John Wiley & Sons, 2010.
52. Argaman, N., and Makov, G. "Density functional theory: An introduction." *American Journal of Physics* 68, no. 1 (2000): 69-79.
53. Feit, M. D., Fleck Jr, J.A., and Steiger, A. "Solution of the Schrödinger equation by a spectral method." *Journal of Computational Physics* 47, no. 3 (1982): 412-433.
54. Shirley, J.H. "Solution of the Schrödinger equation with a Hamiltonian periodic in time." *Physical Review* 138, no. 4B (1965): B979.

55. Wannier, G.H. "Wave functions and effective Hamiltonian for Bloch electrons in an electric field." *Physical Review* 117, no. 2 (1960): 432.
56. Nielsen, O.H., and Richard M.M. "First-principles calculation of stress." *Physical Review Letters* 50, no. 9 (1983): 697.
57. Stadler, R., Wolf, W., Podloucky, R., Kresse, G., Furthmüller, J. and Hafner, J. "Ab initio calculations of the cohesive, elastic, and dynamical properties of CoSi 2 by pseudopotential and all-electron techniques." *Physical Review B* 54, no. 3 (1996): 1729.
58. Charpin, T. "Laboratory of geometrix F-75252 Paris." France A package for Calculating elastic tensors of cubic phase using WIEN (2001).
59. Jamal, M., Bilal, M., Ahmad, I., and Jalali-Asadabadi, S. "IRelast package." *Journal of Alloys and Compounds* 735 (2018): 569-579.
60. Hill, R. "The elastic behaviour of a crystalline aggregate." *Proceedings of the Physical Society. Section A* 65, no. 5 (1952): 349.
61. Voigt, W. "Lehrbuch der Kristallphysik (Textbook of crystal physics)." BG Teubner, Leipzig und Berlin (1928).
62. Reuss, A. J. Z. A. M. M. "Calculation of the flow limits of mixed crystals on the basis of the plasticity of monocrystals." *Z. Angew. Math. Mech* 9 (1929): 49-58.
63. Liu, X., Fu, J., and Chen, G. "First-principles calculations of electronic structure and optical and elastic properties of the novel ABX_3-type $LaWN_3$ perovskite structure." *RSC Advances* 10, no. 29 (2020): 17317-17326.
64. Blanco, M.A., Francisco, E. and Luana, V., 2004. "GIBBS: isothermal-isobaric thermodynamics of solids from energy curves using a quasi-harmonic Debye model." *Computer Physics Communications* 158, no. 1 (2004): 57-72.
65. Otero-de-la-Roza, A., Abbasi-Pérez, D. and Luaña, V. "Gibbs2: A new version of the quasiharmonic model code. II. Models for solid-state thermodynamics, features and implementation." *Computer Physics Communications* 182, no. 10 (2011): 2232-2248.
66. Otero-de-la-Roza, Alberto, and Luaña, V. "Gibbs2: A new version of the quasi-harmonic model code. I. Robust treatment of the static data." *Computer Physics Communications* 182, no. 8 (2011): 1708-1720.

67. Allen P. “Boltzmann theory and resistivity of metals. Quantum Theory of Real Materials” *1st edn. London, US: Kluwer Academic Publishers* 348 (1996):219-250.
68. Ziman, J.M. “Electrons and phonons: the theory of transport phenomena in solids.” *New york, USA: Oxford University Press*; 2001.
69. Hurd C. “The hall effect in metals and alloys. The International Cryogenics Monograph Series”, Vol. 1. Boston, MA: Springer; 1972
70. Madsen G.K.H., Singh D.J., “BoltzTraP. A code for calculating band-structure dependent quantities.” *Comput Phys Commun*. 175, no. 1 (2006):67-71.
71. Morelli, D.T., Slack. G.A. “High lattice thermal conductivity solids. High Thermal Conductivity Materials.” New York: Springer; 2006:37-68.
72. Julian, C.L. “Theory of heat conduction in rare-gas crystals.” *Phys Rev* 137, no. 1A (1965): A128.
73. Leibfried, G. and Schl¨omann, E. Nachr. Akad. Wiss. Gottingen II a(4), 71 (1954).
74. Pei, Y., Wang, H., Gibbs, Z.M., LaLonde A.D., Snyder, G.J. “Thermopower enhancement in Pb1-xMnxTe alloys and its effect on thermoelectric efficiency.” *NPG Asia Mater* 4, no. 9 (2012): e28-e28.

CHAPTER 3

STRUCTURAL, ELECTRONIC, ELASTIC, MECHANICAL, THERMODYNAMIC, AND THERMOELECTRIC PROPERTIES OF $XCeO_3$ (X = Mg, Ca, Sr, Ba)

3.1 INTRODUCTION

The advancement in the technology of the processing of materials has led to a new revolution in the field of materials science [1, 2]. The synthesis of novel materials offered new dimensions to the research. The novel materials have demonstrated advanced functionality. The increasing advancement has always been primarily due to the need for the creation of novel energy sources. Moreover, diminishing of the natural energy sources with rapid progression has created global changes in the environment. The scarcity of energy sources has been a subject of global concern. Therefore, materials are to be sought as alternative source [3, 4] of power generation. One of the prime power generation sources is the solar cell. The consumption of solar energy is being augmented by humans for their comfort. The total installed capacity of solar cell photovoltaics has reached 480 GW globally up to 2018 [5]. In order to sustain solar energy, certain measures are to be taken into account as its consumption is expected to be 8519 GW by the end of the year 2050 [5]. On the other hand, the possibility of reuse of energy sources from the waste heat sources like motor vehicles, radiators, and exhaust systems seems an effective alternative owing to the thermoelectric effect on materials.

In this regard, the thermoelectric solid-state power generator [6, 7] is emerging as an alternative source of energy based on the waste heat consumption concept. It uses the simple concept in which temperature difference across the material generates potential difference, which is the well-known Seebeck effect [8, 9]. In this effect the maintenance of the temperature difference across the material is caused by burning fuel from motor vehicles, radiators from industries, harvesting from the body heat, radioactive decay, etc. Therefore, a thermoelectric generator (TEG) works on the principle of converting thermal energy into electrical energy. The competence of such

generator (TEG) is examined by the figure of merit, $ZT = S^2\sigma T/\kappa$, where, S, σ, T and κ denote Seebeck coefficient, electrical conductivity, temperature, and thermal conductivity, respectively. Further, κ consists of lattice (κ_l) and electronic (κ_e) components. The materials having more values of S, σ and less value of κ are considered for the thermoelectric applications. Therefore, materials are being investigated for their figure of merit value near 1 or more than 1. The ZT is also contingent on the level of suitable doping [10-12] and the method of sample preparation. The value of figure of merit for PbTe [13] was first reported to be 0.8, which after considering improved mechanism increased to 1.4. Pb-chalcogenides were consequently thought to be appropriate resources for good TE performances [10, 11, 14–24].

Our study is based on the objective to provide insight into the $XCeO_3$ (X= Mg, Ca, Sr, and Ba) with respect to thermophysical and thermoelectric performances and its suitability for thermally operated devices. In this regard, the paper is systematized: Section 3.2 deals with the methodology, and in Section 3.3 computational results are presented followed by discussion. In Section 3.4 conclusion is presented.

3.2 COMPUTATIONAL DETAILS

The physical properties of cerate oxide perovskite $XCeO_3$ (XCO) are studied through FP-LAPW method [25] grounded on DFT [26] as applied in the WIEN2K code [27]. The $XCeO_3$ belongs to the space group Pm-3m (space group no. 221). The structural optimization is done by using LDA [28], GGA-PBE [29], WC [30], PBEsol [31]. For fulfilling convergence criteria, we have taken G_{max} = 12 (a.u.)$^{-1}$, $R_{MT}.k_{MAX}$ = 7 and l_{MAX} = 10. Additionally, we have performed mBJ XC potential to improve the bandgaps of XCOs. We have used 10^{-4} Ry and 10^{-3} a.u.^{3} as convergence criteria for energy and charge, respectively. The Brillouin zone uses 1000 K points in the tetrahedron method [32] for density of states (DOS).

3.3 RESULTS AND DISCUSSION

Various properties related to Cerium-based oxide perovskite are discussed in the following section.

3.3.1 Structural Properties

The investigation of XCOs for their structural behavior has been computed and presented in this section. These structures show cubic nature in 221 space group. For the studied material, the optimization of the structure is done by considering the GGA-PBE, PBEsol, and WC potential. The obtained E-V data is presented in *Figure 3.1*. The minimum of the energy-volume curve expresses the optimized value of the volume and thus evaluates lattice parameter. Our obtained value of the lattice parameter in cubic structure is found in experimental match [33-35] as shown in *Table 3.1*. In Pm-3m structure each atom occupies Wyckoff positions as X at 1a (0, 0, 0), O at 3c (1/2, 1/2, 0), (1/2, 0, 1/2), (0, 1/2, 1/2) and Ce at 1b (1/2, 1/2, 1/2). The Cerium (Ce) is octahedrally coordinated with six oxygen ions. The calculated ground state structural parameters are summarized in *Table 3.1*. Our findings are quite analogous to the other rare-earth perovskite compounds [36-41]. These perovskite compounds have the same Pm-3m structure in the ground state as that of the $XCeO_3$. Materials' suitability for energetical stability is analyzed by their respective formation and cohesive energies obtained through equations 3.2 and 3.3, respectively [43-45].

$$F.E = \frac{[E(XCO) - (E(X) + E(Ce) + 3E(O))_{solid}]}{n} \quad (3.1)$$

Formation energy per atom is expressed in *equation 3.1* consisting of E(XCO) is the energy of the whole compound $XCeO_3$ (X= Mg, Ca and Ba) and $E(X)_{solid}$, $E(Ce)_{solid}$ and $E(O)_{solid}$ are the energies of X, Ce and O in their free state. We have obtained negative values of formation energies for MCO, CCO, SCO and BCO which ensure the possibility of manufacturing these compounds.

$$C.E = \frac{[(E(X) + E(Ce) + 3E(O))_{atom} - E(XCO)]}{n} \quad (3.2)$$

Cohesive energy is calculated via *equation 3.2* and simultaneously presented in *Table 3.1*. $E(X)_{atom}$, $E(Ce)_{atom}$ and $E(O)_{atom}$ are energies of X, Ce and O in their bulk state. It expresses the degree of bonding, the higher the value, the more stable the combination among atoms.

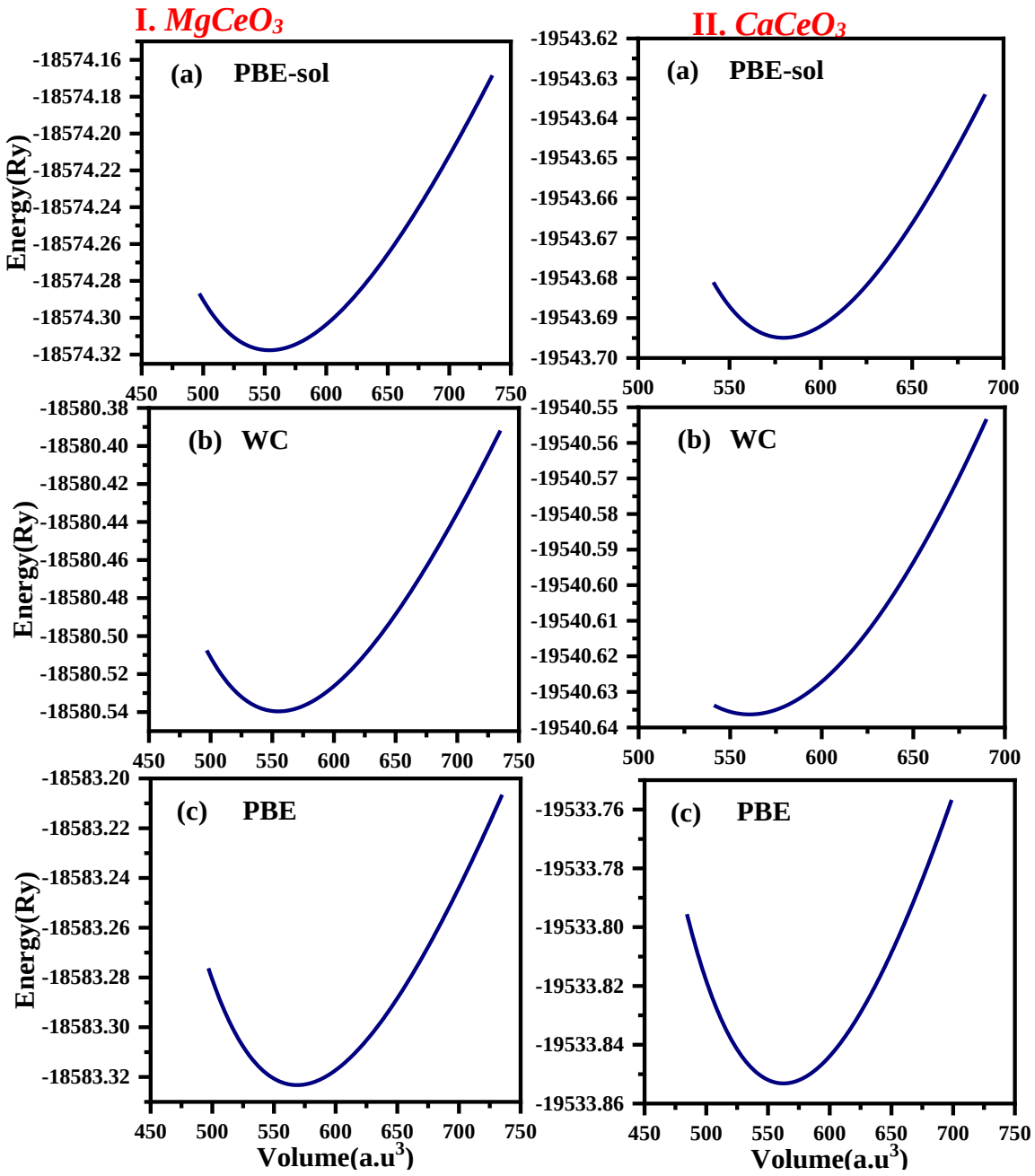

Figure 3.1(a): Optimize graph for I) $MgCeO_3$, II) $CaCeO_3$, in different XC potential a) PBEsol-GGA, b) WC-GGA, and c) PBE-GGA

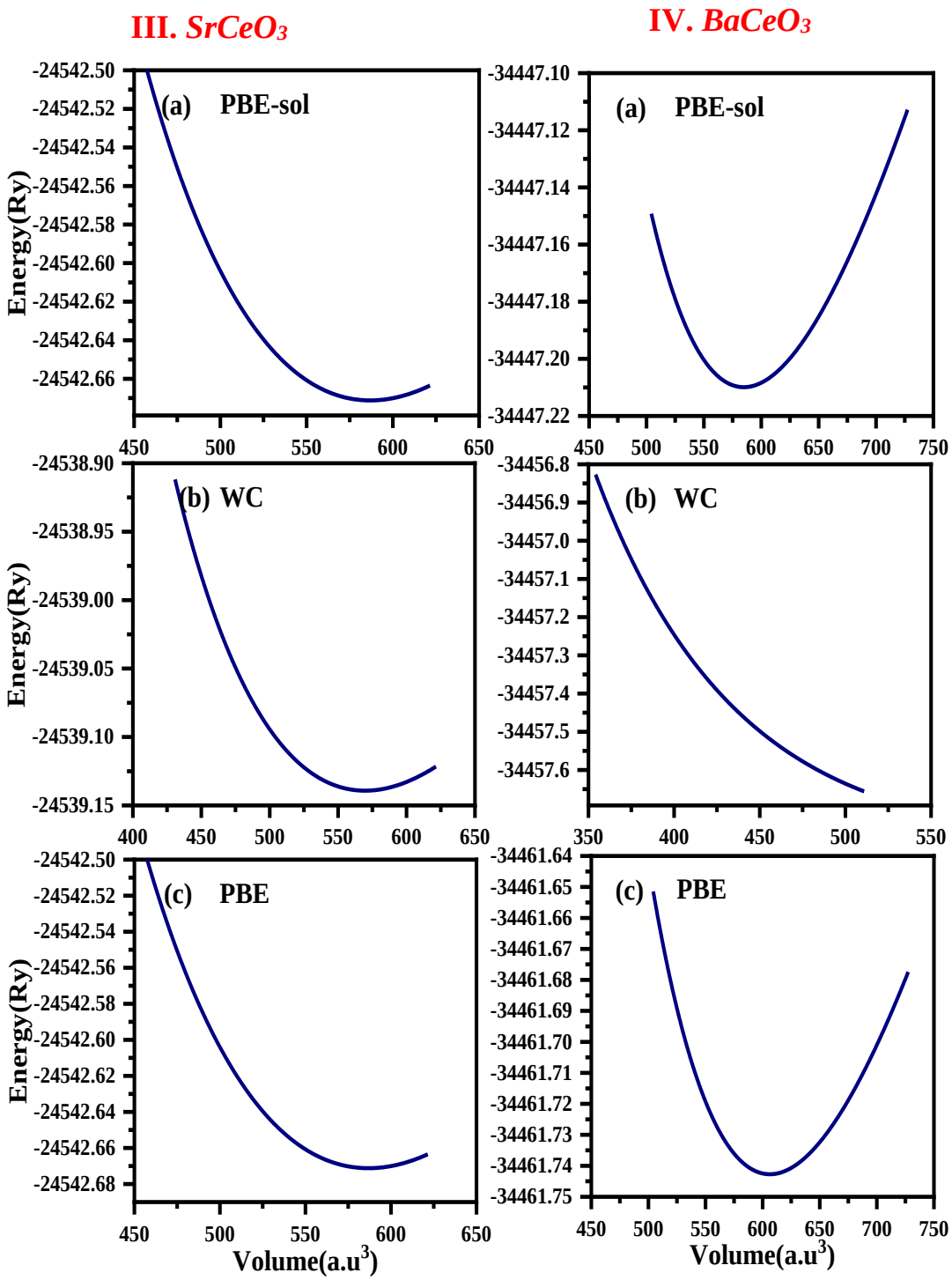

Figure 3.1(b): Optimize graph III) $SrCeO_3$, and IV) $BaCeO_3$ in different XC potential a) PBEsol-GGA, b) WC-GGA, and c) PBE-GGA

Table 3.1: Ground state parameters: Lattice constant *a* (in Å), volume *V* (a.u^3), bulk modulus *B*, Bulk derivative B_P, Enthalpy of formation E_{form} (KJ/mol) and Bondlength (Å), Minimum total energy E_{tot} (Ry), Energy of cohesion E_{coh} (eV/atom) of $XCeO_3$ (X=Mg, Ca, Sr, and Ba) perovskites

Compound	**XC**	**a**	**V**	**B**	**B_P**	**E_{tot}**	**E_{coh}**	**E_{form}**	**Bond length**
	LDA	4.3206	544.28	133.29	4.56	-18565.909746	5.43	-1088.39	Mg-Ce=4.09
$MgCeO_3$									Ce-O=2.36
	PBE	4.3854	569.16	114.68	4.65	-18583.323221			O-Mg=3.34
GGA	**WC**	4.3495	555.28	123.13	4.36	-18580.539531			
	PBEsol	4.3465	554.13	123.03	4.36	-18574.317541			
	Others	-							
$CaCeO_3$	**LDA**	4.3336	549.19	135.38	4.57	-19524.670799	6.16	-1406.33	Ca-Ce=4.11
	PBE	4.4111	579.20	115.59	4.33	-19543.692318			Ce-O=2.37
GGA	**WC**	4.3631	560.51	104.94	2.43	-19540.636312			O- Ca=3.36
	PBEsol	4.4126	579.80	130.95	6.31	-19543.694892			
	Others	4.40 [35]							
$SrCeO_3$	**LDA**	4.3475	554.52	131.99	3.84	-24519.565882	6.28	-	Sr-Ce=3.69
	PBE	4.4327	588.32	110.22	4.12	-24542.670676			Ce-O=2.13
GGA	**WC**	4.3866	569.70	125.77	3.65	-24539.139218			O- Sr=3.02
	PBEsol	4.4308	586.87	120.65	3.43	-24542.671208			
	Others	4.23 [33]							
$BaCeO_3$	**LDA**	4.3889	570.49	131.60	4.47	-34433.500281	5.50	-1528.95	Ba-Ce=4.17
	PBE	4.4789	606.35	110.69	4.52	-34461.742772			Ce-O=2.41
GGA	**WC**	4.4030	576.01	139.28	3.75	-34457.692679			O- Ba =3.41
	PBEsol	4.4257	584.98	121.70	4.40	-34447.209938			
	Others	4.48 [35], 4.47 [34]							

3.3.2 Electronic Properties

The electronic performances of XCOs have been inspected with the help of electronic energy density of states (DOS) and band structure. *Figure 3.2* depicts band structures of XCOs under the PBE-GGA and mBJ-GGA within the Brillouin zone along high symmetry directions. Bandgap values in eV through different XC potentials and their comparison to others' work are conveyed in *Table 3.2*. Bandgap for XCO is found to be undervalued under LDA and GGA. While with mBJ bandgap value matches with experimental results. Band structure of XCOs shows semiconductor nature consisting of direct as well as an indirect bandgap.

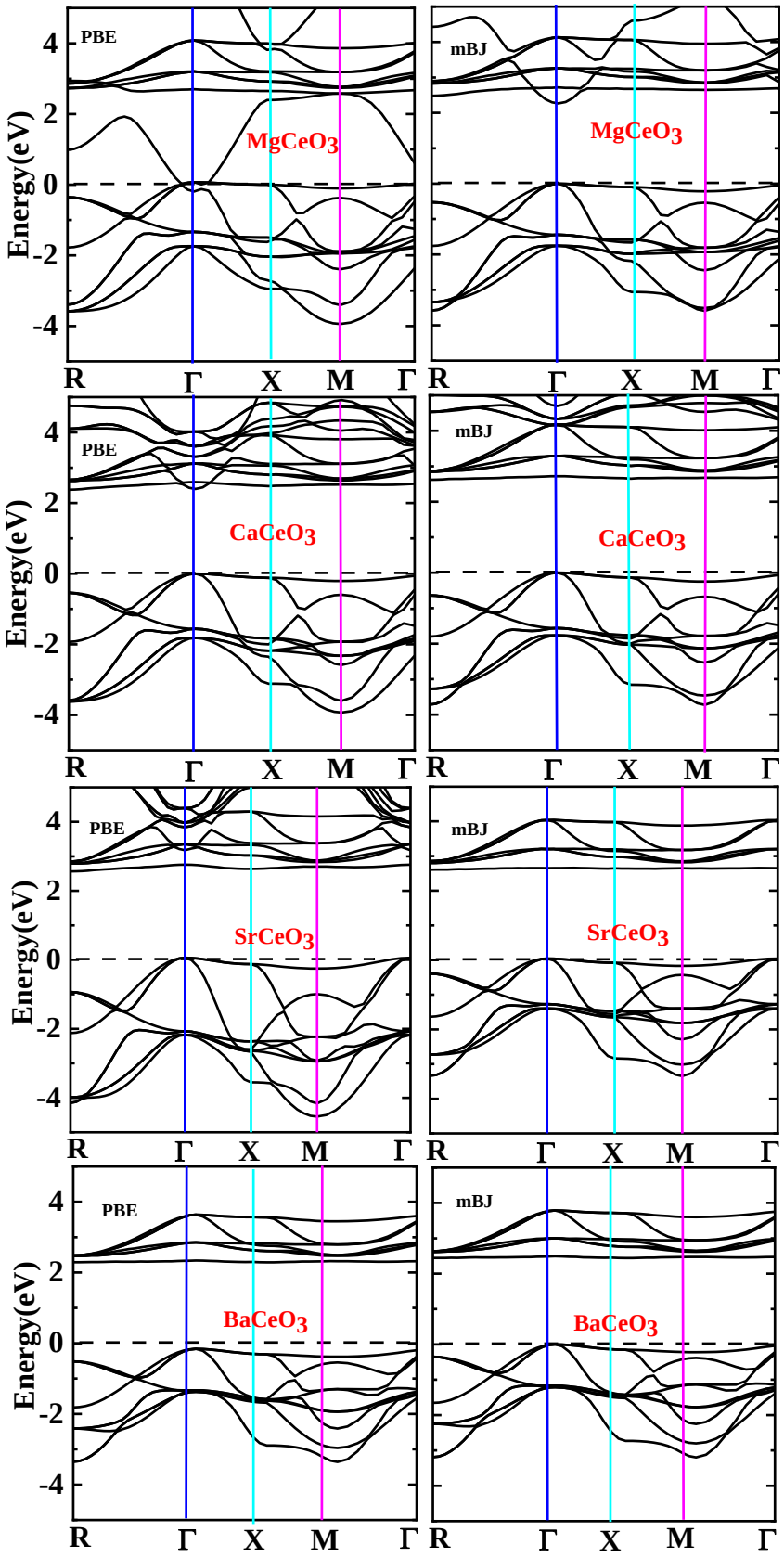

Figure 3.2: Band structure in PBE(Left) and mBJ(right) for $XCeO_3$ (X= Mg, Ca, Sr, and Ba)

The direct band gap values in case of mBJ for MCO, CCO SCO, and BCO are 2.26, 2.6, 2.56, and 2.4 eV, respectively at Γ→Γ symmetry. The contributions of various electronic states to transport properties of XCOs can be understood by calculating total and Partial DOS (TDOS and PDOS). We have, therefore, considered TDOS and PDOS for XCOs and presented in *Figure 3.3* and *3.4*, respectively which depict that lowest lying bands are due to O-*s* states in the VB. Majorly Ce-*f* states and X-*d* states are present in CB. In SCO and BCO, Ce-d states are located near 7.5 eV which are hybridized with the X-*d* and O-*p* electronic states. A sharp peak in BCO around 10 eV is because of *the Ba-f* orbital. The contribution of Mg, Ca, Sr, and Ba in the VB is negligible. The oxygen contribution is seen in both the valence and conduction areas.

Table 3.2: Bandgap (in eV) using different XC potentials

Compound	LDA	GGA			mBJ	Others' work
		PBE	WC	PBEsol		
$MgCeO_3$	0.030	0.019	0.022	0.029	2.266	-
$CaCeO_3$	2.353	2.377	2.433	2.396	2.619	-
$SrCeO_3$	2.372	2.505	2.395	2.361	2.564	-
$BaCeO_3$	2.426	2.351	2.451	2.414	2.439	2.33[42], 2.62 [44]

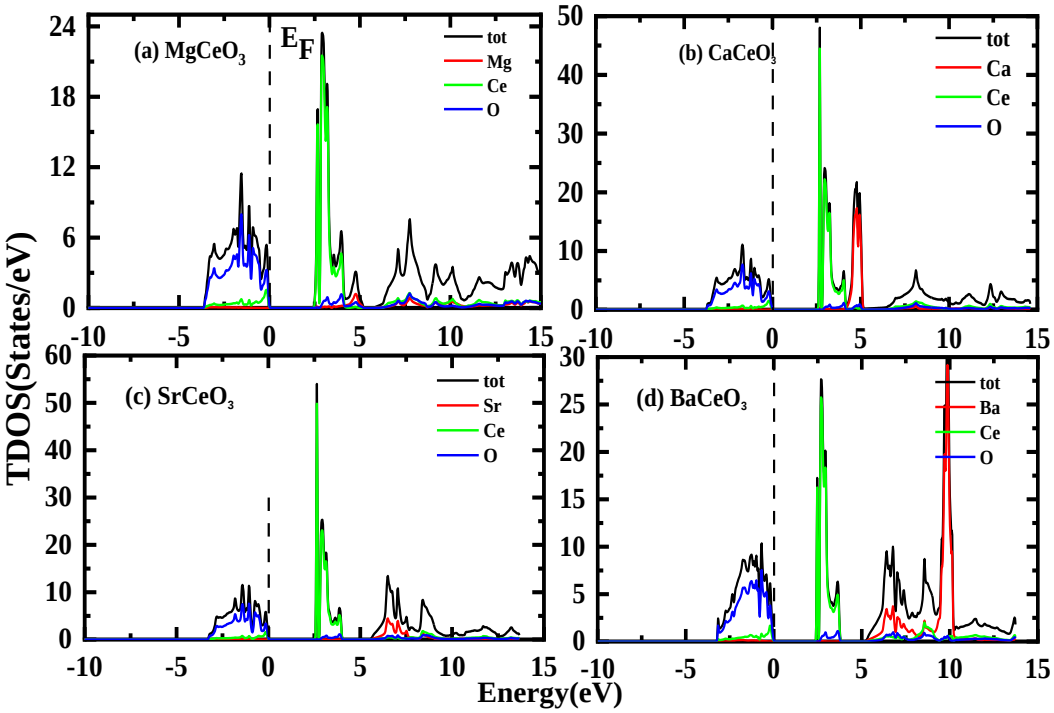

Figure 3.3: Total Density of states TDOS corresponding to energy (in eV) plot for a) $MgCeO_3$ b) $CaCeO_3$ c) $SrCeO_3$, and d) $BaCeO_3$

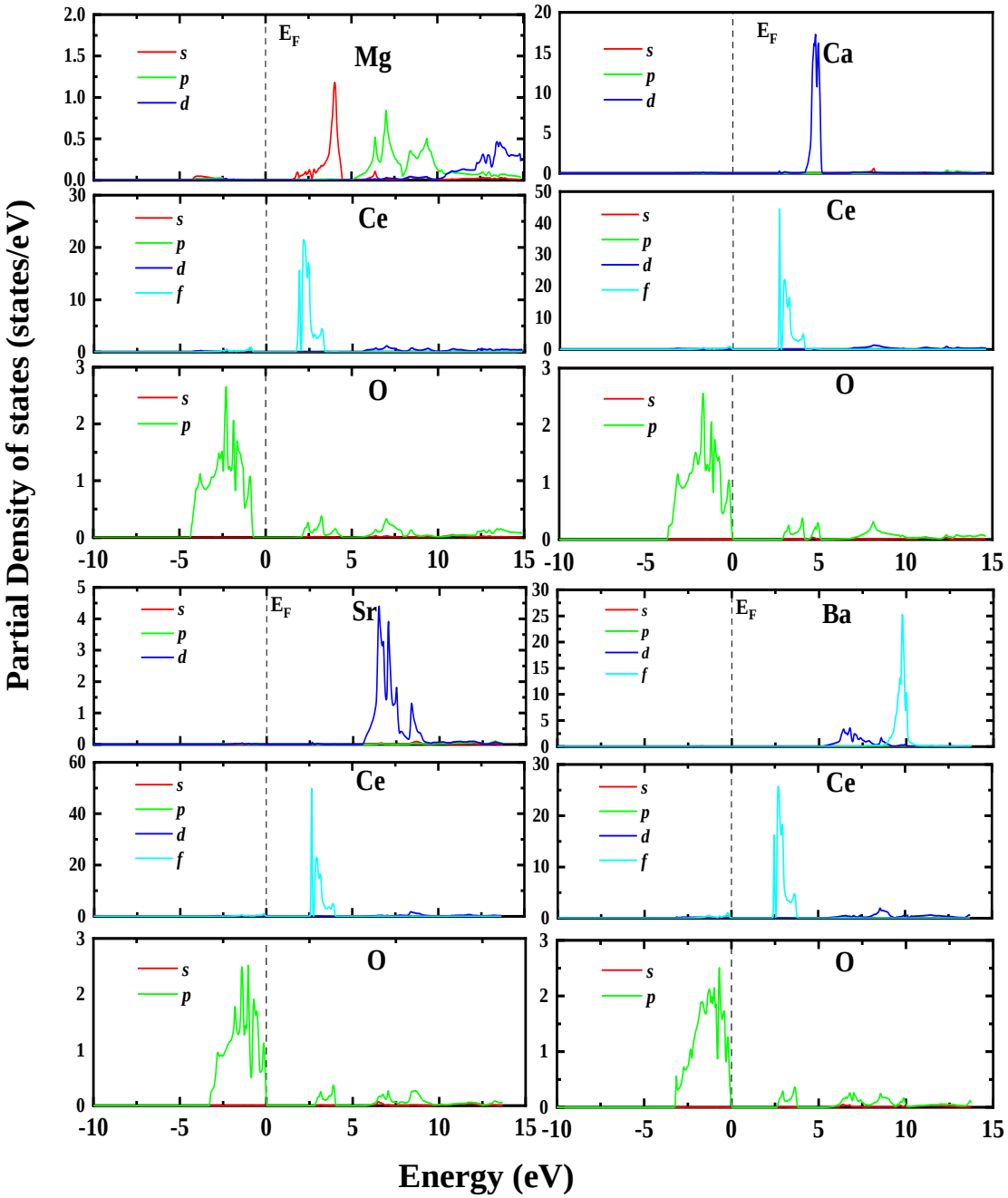

Figure 3.4: PDOS (states/eV) versus Energy (eV) for a) $MgCeO_3$ b) $CaCeO_3$ c) $SrCeO_3$, and d) $BaCeO_3$

3.3.3 Elastic and Mechanical Properties

Above-mentioned properties for XCOs have been examined through DFT with GGA and IR elast package [46] inbuilt in WIEN2K package. The determination of elastic parameters plays a vital role in the material's ability to distort the implication of the force. These elastic constants are also useful in determination of mechanical properties and stability of substances. It also provides information on the behavior of bonding forces, as well as the materials' ductility or brittleness. The effects of the external forces on these materials are measured from the elastic constants. The elastic performances are also associated to the quantities like melting and Debye temperature θ_D, heat capacity, and Grüneisen constant. The elastic parameters are evaluated using the well-known Hooke's law which states that strain and stress have a direct relationship with an elasticity constant. The only valid elastic parameters C_{ij} for the cubical crystal are longitudinal compression (C_{11}), transverse expansion (C_{12}), and shear modulus (C_{44}). To obtain these parameters strain method is used in which a small strain is provided into an unstrained lattice. The obtained value of *Cij* from the present calculations for MCO, CCO, SCO, and BCO are tabulated in *Table 3.3*. The elastic parameters are required for evaluation of materials' mechanical properties. These materials fulfill the required mechanical stability of a cubical system. The required mechanical stability norms [47, 48] for a cubical structure $XCeO_3$ are larger than the succeeding limits of the elastic constants i.e., C_{11}-$C_{12} > 0$, C_{11}+$2C_{12} > 0$, $C_{11} > 0$, $C_{44} > 0$. All considered compounds fulfill the criteria of mechanical stability. Further, some mechanical parameters, young's Y, shear G, and bulk modulus B can be evaluated from these elastic constants. Their relations with the elastic constants [49-53] are shown in chapter 2 *equations (2.92)-(2.102)*. The stiffness of the material is described by the shear modulus and bulk modulus relation *B* relates to how much the material is resistive to the change in the volume. The next elastic modulus, i.e., Young's modulus *Y*, depends on bulk *B* as well as on the shear *G*. It describes the elongation and compression of the solids. Higher *Y* represents more stiffness in the compound. The values of *B*, *G*, and *Y* for XCOs are given in *Table 3.3*. Other mechanical parameters like Poison ratio, Pugh ratio, anisotropy, Cauchy's pressure and thermodynamic parameters such as Debye & melting temperature are also

accessible in *Table 3.3*. Poison Ratio (v) defines the behavior of bonding forces between atoms. The value of the Poison ratio should be in the range of 0.25-0.50. Its value is 0.1 for covalent, 0.25 for metallic and 0.33 for ionic bonding [54, 55]. SCO and BCO show mix nature of metallic and ionic bonding while MCO and CCO shows ionic bonding. Calculated values of Poison ratios are 0.340, 0.296 and 0.291 for MCO, CCO, SCO, and BCO respectively. Cauchy pressure (C_{12}-C_{44}) describes material's ductility and brittleness. Its positive values indicate ductile behavior, while negative values signify the brittle beahavior. Pugh's ratio (B/G) also describes the material's ductility and brittleness. This defines the ranges of plasticity of the crystals. According to Pugh [56], if $B/G < 1.75$, it shows brittleness; otherwise, it shows ductility. After examining, the obtained values of Cauchy pressure and B/G ratio, we concluded that XCO shows a positive value of Cauchy pressure and B/G >1.75 which means materials are ductile and can be easily deformed. Elastic anisotropy (A) is a very significant parameter in engineering and the manufacturing area. It helps in determining the microcracks within the material. Its divergence from 1 represents the anisotropic behavior. It can be evaluated using the formula given.

$$A = \frac{2C_{44}}{C_{11} - C_{12}} \tag{3.3}$$

The obtained value of A for XCO (X= Mg, Ca, Sr, and Ba) is less than unity and thus anisotropic. The thermal behavior of the compound can also be understood by considering elastic parameters. Xing Liu et. al [57] have proposed that θ_D can be computed through elastic constants. It reflects thermodynamic properties and its association with parameters like specific heat, longitudinal velocity, transverse velocity, and the thermal expansion coefficient of the solids. The values of θ_D and T_M for XCOs are shown in *Table 3.3*. Also, we have estimated melting temperature (T_M) for $XCeO_3$ as given in *equation (3.4).*

$$T_M = [553(K) + (5.911)C_{12}]GPa \pm 300K \tag{3.4}$$

Table 3.3: Elastic and Mechanical parameters C_{11}, C_{12}, C_{44} (GPa) and Bulk modulus B (GPa), Shear modulus G (GPa), Young's modulus Y (GPa), Poison Ratio v, Debye temperature θ_D (K), Cauchy Pressure C_{12}-C_{44} (GPa), Pugh's ratio B/G, Anisotropy A, Melting temperature T_M (K), respectively.

Parameters	**$MgCeO_3$**	**$CaCeO_3$**	**$SrCeO_3$**	**$BaCeO_3$**
C_{11}	220.6	212.27	212.55	189.18
C_{12}	71.08	77.63	64.055	66.3
C_{44}	28.4	24.03	43.96	46.4
B	120.9	122.5	113.59	107.3
G	42.3	36.85	54.30	51.9
Y	113.7	100.36	140.52	134.2
ν	0.343	0.36	0.29	0.291
θ_D	414.8	373.0	411.9	372.7
C_{12}-C_{44}	42.6	53.6	20.09	19.9
B/G	2.85	3.32	2.09	2.06
A	0.38	0.35	0.59	0.75
T_M	1856.7	1645.2	931.6	1671.1

3.3.4 Thermodynamic Properties

To check the suitability of XCOs for its possible applications in industry, thermophysical performances like entropy, Grüneisen parameter, heat capacity, bulk modulus, volume, thermal expansion coefficient & Debye temperature and have been evaluated using QHD model via Gibbs program [58-60] with pressure P variation from 0 – 50 GPa & temperature T variation from 0 – 1200 K.

We have plotted the variations of volume, Debye temperature θ_D, thermal expansion coefficient α, bulk modulus B, Entropy S, Grüneisen parameter γ, and heat capacity C_V with respect to T in *Figures 3.5-3.11.*

Figure 3.5 shows change in unit cell volume (V) of $XCeO_3$ with T. From Figure, one can interpret that the volume increases with T for constant values of P. On the other hand, volume declines with increase in P.

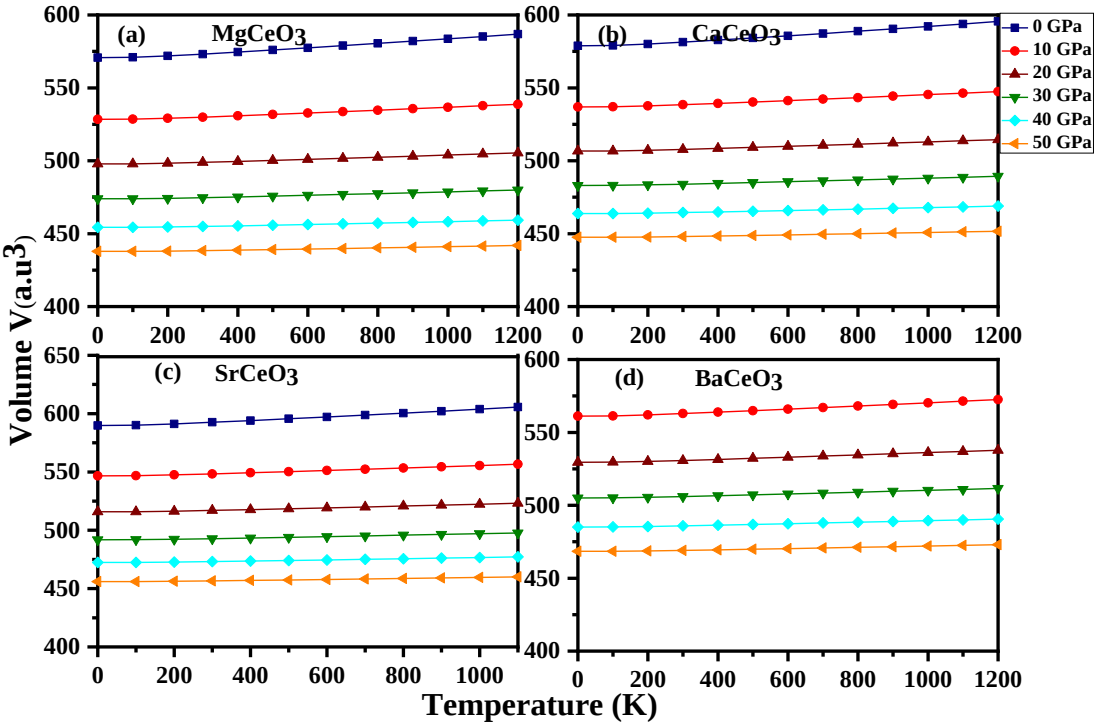

Figure 3.5: Volume variation with *T* at constant *P* for a) $MgCeO_3$ b) $CaCeO_3$ c) $SrCeO_3$, and d) $BaCeO_3$

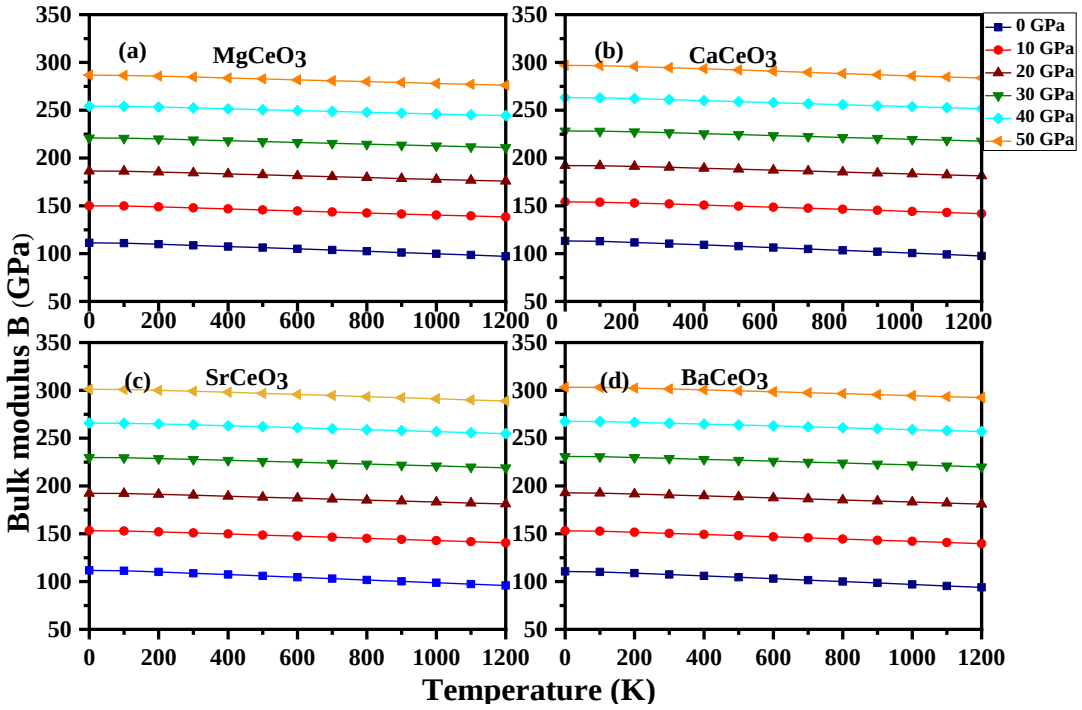

Figure 3.6: Bulk modulus variation with *T* at constant *P* for a) $MgCeO_3$ b) $CaCeO_3$ c) $SrCeO_3$, and d) $BaCeO_3$

In order to understand softness/hardness of solids, the bulk modulus (*B*) of the material plays significant role. The *B* responds under varying temperature and pressure. We have plotted *B* corresponding to *T* and *P*. *Figure 3.6* shows inverse effect (with respect to V(T) behavior) on B under temperature variation at a given values of pressure. *B* declining slowly with *T* at every considered pressure's value. This reduction in *B* with increase in temperature is due to the reduction in the hardness of the $XCeO_3$ material. It seems that there exists a direct relation between pressure and bulk modulus for the material. As the value of pressure increases bulk modulus also increases showing an almost linear relation between them.

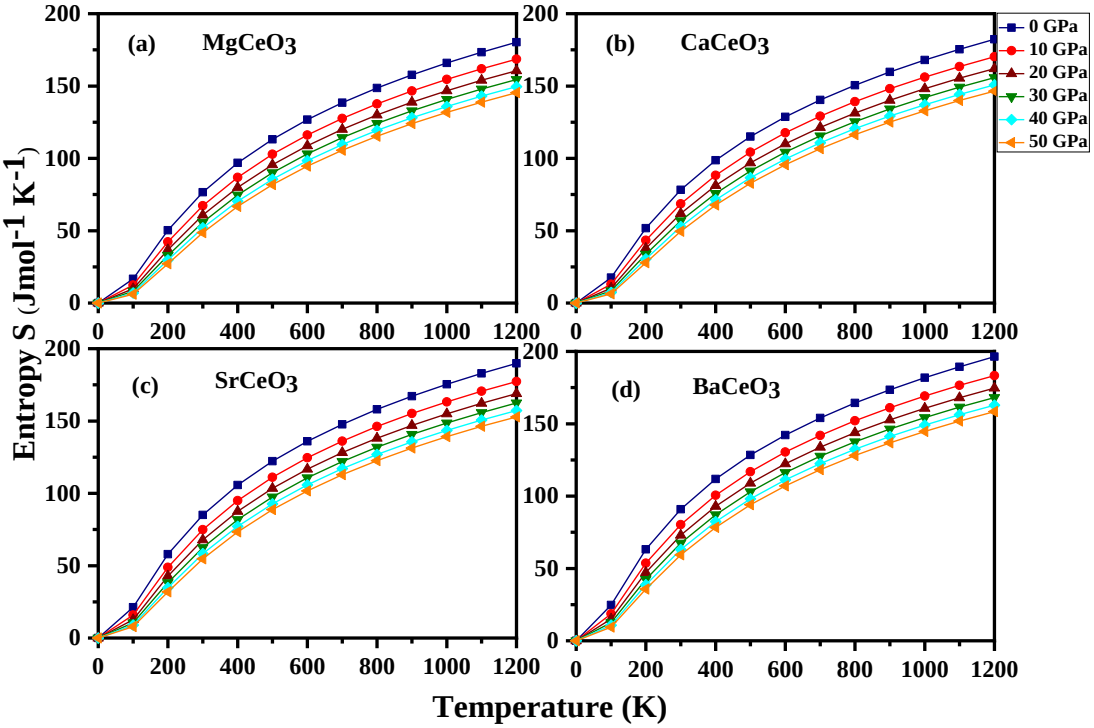

Figure 3.7: Entropy variation with *T* at constant *P* for a) $MgCeO_3$ b) $CaCeO_3$ c) $SrCeO_3$, and d) $BaCeO_3$

One of the important thermal quantities that deal with disorder behavior of the crystals is the entropy, *S*. The entropy of the solids can be tuned by varying temperature and pressure. We have, therefore, calculated *S* for $XCeO_3$ under temperature & pressure variation. In *Figure 3.7*, we have depicted the variation of *S* with respect to temperature at constant pressure and it is noticed that entropy of the solid increases with temperature. The entropy value is calculated to be zero at 0 K irrespective of pressure. This is a consequence of the 3rd law of thermodynamics. The increase in the *S* shows that degree of disorderliness in XCOs increases which can be

understood by considering the calculated values of *S* which increase with increasing temperature. Interestingly, the decrease in entropy is noticed while pressure on the solid is increased at a constant temperature. Such decrease resembles the reduction of the disorder effect in solids.

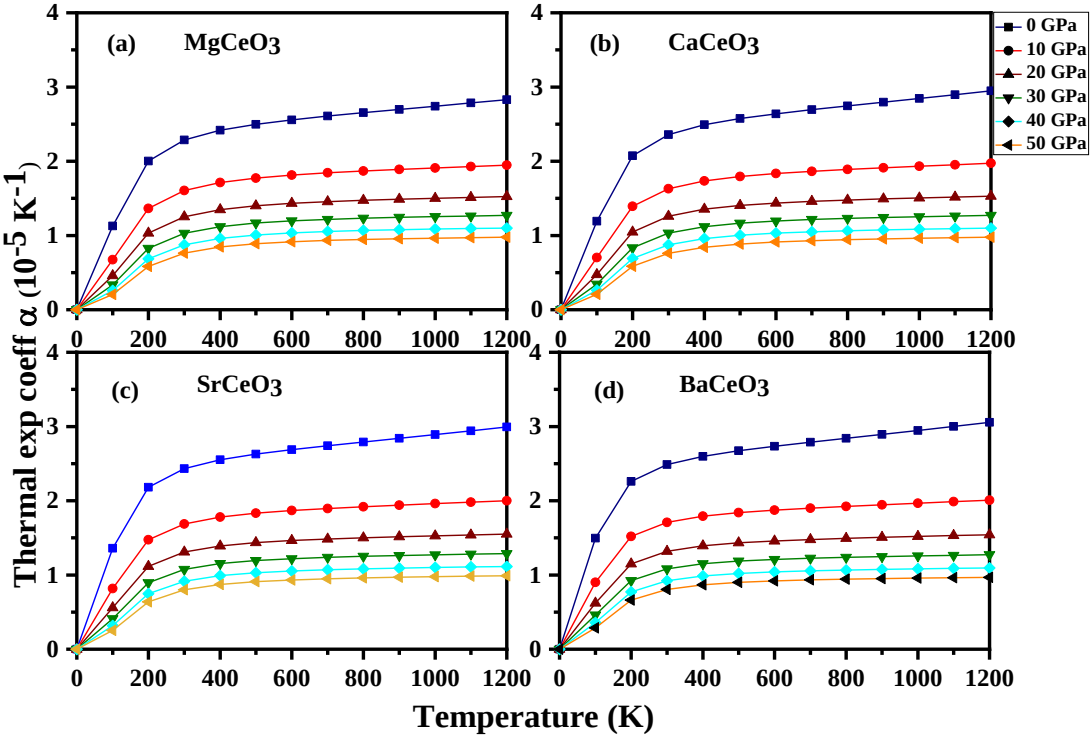

Figure 3.8: Thermal expansion coefficient's variation with *T* at constant *P* for a) $MgCeO_3$ b) $CaCeO_3$ c) $SrCeO_3$, and d) $BaCeO_3$

Solids expand when heated and show contraction when pressurized. Further, the solids show expansion on increasing temperature, even at a constant high pressure value. Conversely, solids show contraction on increasing pressure, even at a constant high temperature. To understand such behaviour of solids we have calculated thermal expansion coefficient, α of XCOs. *Figure 3.8* presents the variation of α as a function of temperature at constant pressure. It is clear from the figure that there is rise in the value of α upto 200 K and beyond 200 K this rise is quite slow. Overall, due to thermodynamic reasoning, the trend is quite similar to that of the heat capacity. The value of α decreases as pressure increases. Furthermore, thermal expansion coefficient helps one to understand melting temperature and strength of atomic bonding of the solids. When the thermal expansion coefficient is large, the strength of atomic bonding is low. This results in low melting temperature of the solid. Conversely,

small value of thermal expansion coefficient implies high strength of atomic bonding in the solids and as a consequence the melting temperatures becomes high.

Grüneisen parameter, γ, linked with degree of anharmonicity, measure the change in vibrational frequencies with respect to change in volume. *Figure 3.9* represents the variation in Grüneisen parameter, γ as a function of *T*. γ rises gradually with rising *T* and falls quickly with rising *P*. The effect of pressure on γ is more pronounced than that of temperature. The decrease in the value of Grüneisen parameter denotes that anharmonicity decreases in XCOs with increasing pressure.

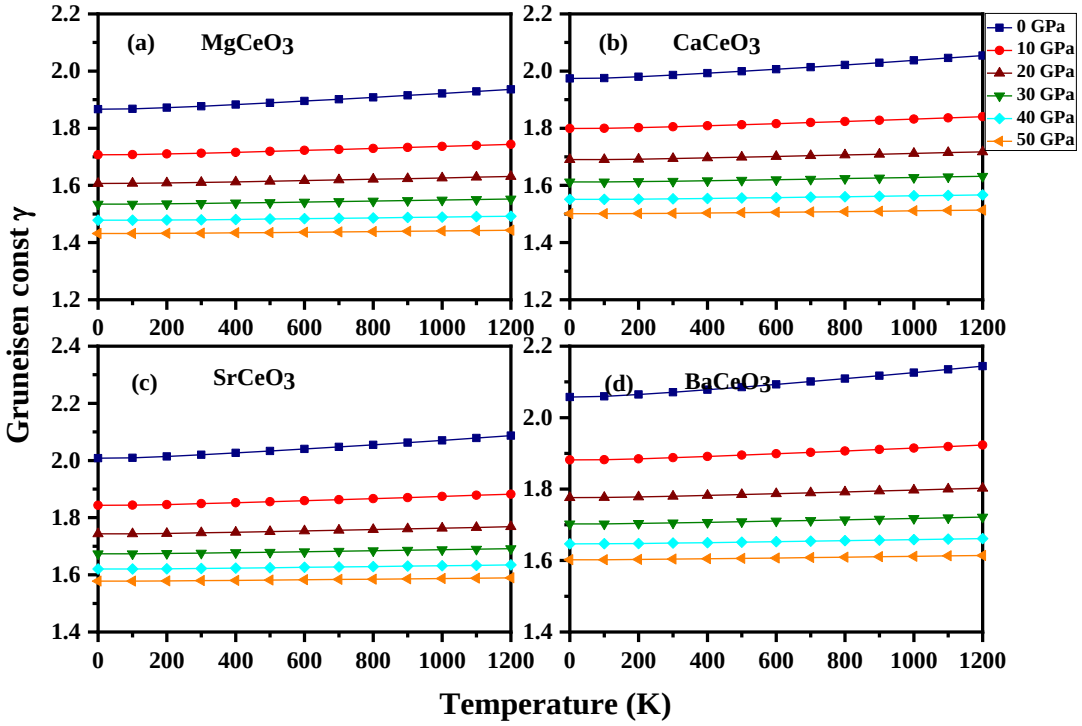

Figure 3.9: Grüneisen constant variation with *T* at constant *P* for a) $MgCeO_3$ b) $CaCeO_3$ c) $SrCeO_3$, and d) $BaCeO_3$

The Debye temperature, θ_D is obtained via *equation (2.100)*. This model correctly explains the lattice vibrations with T^3-variation of specific heat at lower *T* and its attainment of Dulong-Petit limit at high temperature. We have calculated θ_D of XCOs under ambient conditions and also at varying temperatures and pressures. Further, plotted it with temperature (0-1200K) and pressure (0-50 GPa) in *Figure 3.10*. One can notice from the Figure that θ_D decreases slowly with increase in temperature at constant pressure. A substantial increment is noticed with increase in pressure.

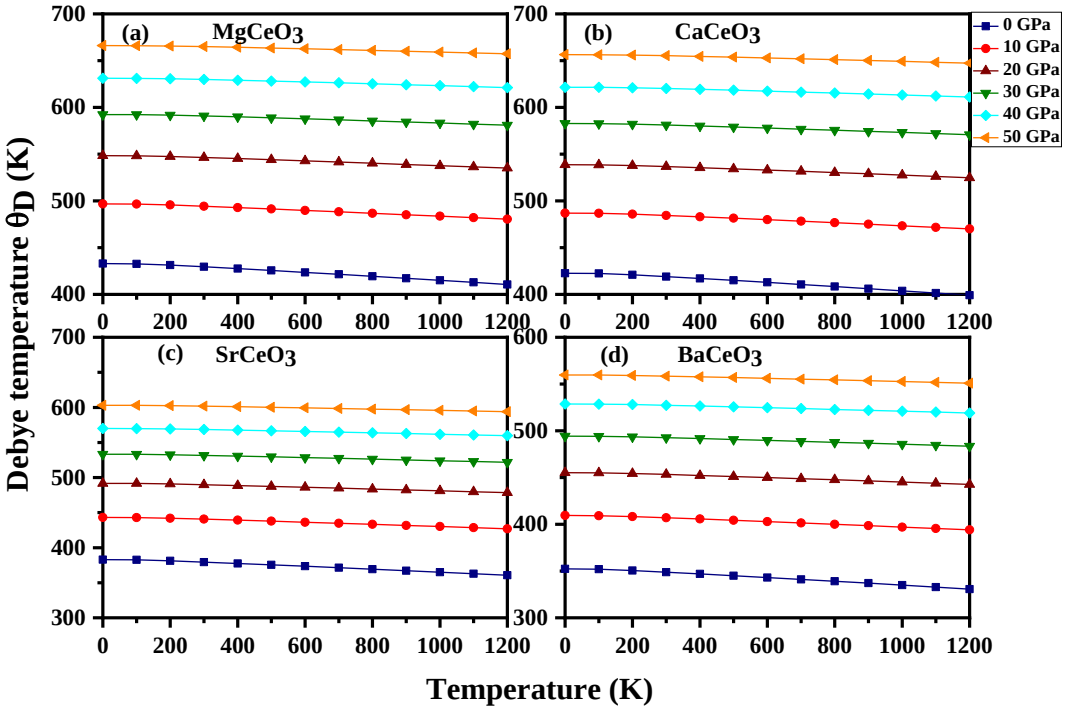

Figure 3.10: Debye temperature variation with *T* at constant *P* for a) $MgCeO_3$ b) $CaCeO_3$ c) $SrCeO_3$, and d) $BaCeO_3$

The heat capacity at constant volume, C_V has been estimated for XCOs and its variation with *T* has been shown in *Figure 3.11*. Figure shows temperature effect on C_V at fixed pressure values of 0, 10, 20, 30, 40, and 50 GPa. A rapid increase in C_V is observed in temperature range (0-300K), which is quite common in solids and represents the T^3-law due to Debye. Further, increase in the C_V becomes gradual at higher temperatures and C_V becomes constant (anharmonicity vanishes) approaching the Dulong and Petit limit [61]. As pressure increases C_V decreases slowly. Therefore, inverse effects on C_V are noticed on increasing temperature and pressure. It was also noticed that temperature has more significant effect than pressure on C_V.

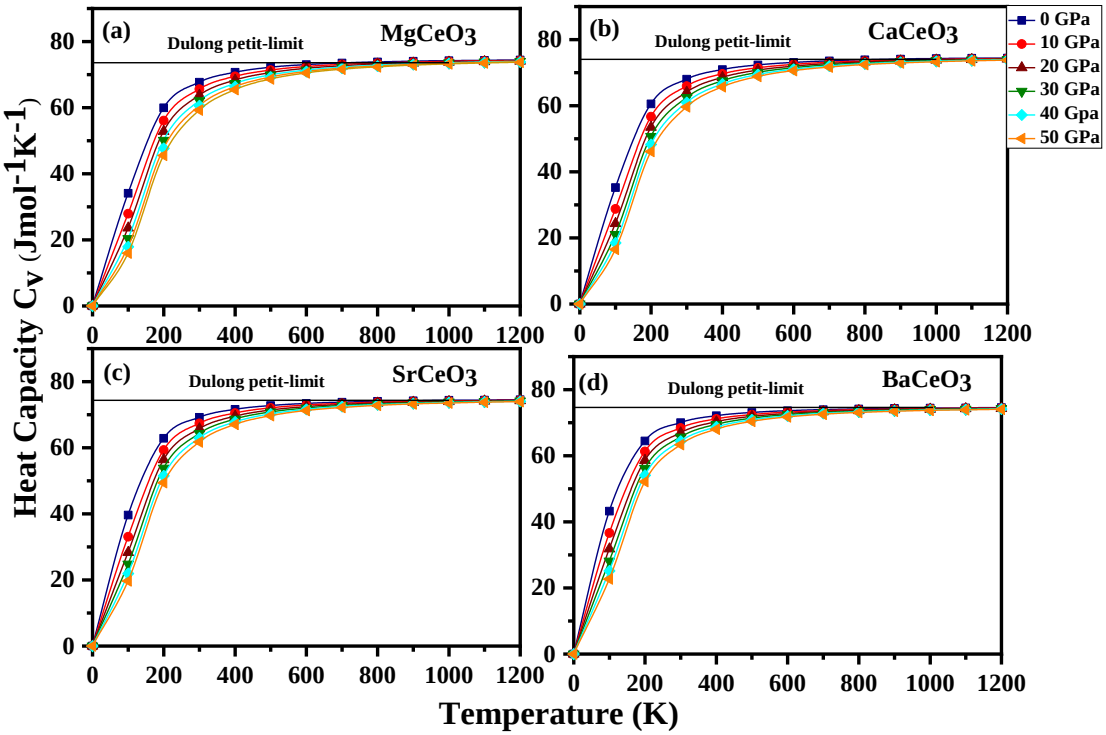

Figure 3.11: Heat Capacity variation with *T* at constant *P* for $XCeO_3$

3.3.5 Thermoelectric Properties

Thermoelectric materials are substitute causes of energy owing to their capability to change heat into electricity and electricity into heat [104, 105]. The thermoelectric devices with high efficiency have high *ZT*, which depends on the Total thermal conductivity κ, Seebeck Coefficient $\mathcal{S}$, and Electrical conductivity σ. In this section, we have evaluated these quantities using Boltzmann theory [62-66] incorporated in BoltzTrap code, which is applied in WIEN2K code [25]. The Seebeck coefficient of $XCeO_3$ variation is shown in *Figure 3.12a*. It is noticed that in the lower region (below room temperature) there is a rapid rise in $\mathcal{S}$. $\mathcal{S}$ first increases till 300 K (for MCO), 400 K (for SCO) and 500 K (for CCO, BCO), then it declines as temperature increases.

The electrical conductivity, σ/τ has also been estimated for $XCeO_3$ for different temperatures, where τ is the relaxation time. As σ/τ is directly proportional to *ZT*, our motive is to find an increment in σ/τ while varying temperature. Considering *Figure 3.12*c, σ/τ increases as temperature increases from 0 to 1200 K. Its value reaches 4.35, 4.66, 4.98, 5.59 ($10^{19}/\Omega ms$) for MCO, CCO, SCO, BCO at 1200 K.

Further, κ is inversely proportional to *ZT*, therefore, our motive is to find decrease in the κ with increasing temperature. Since thermal conductivity, $\kappa = \kappa_e + \kappa_l$, therefore we have estimated both thermal conductivities in this study. The κ_l is calculated via the Slack equation [67-69]. In *Figure 3.12d* and *Figure 3.12e*, variations of electronic κ_e/τ and lattice κ_l/τ thermal conductivities with temperature are shown. *Figure 3.12d* shows the κ_e/τ value increases with increment in temperature with the value obtained at 1200 K equivalent to 3.9, 3.6, 3.75, 3.5 (10^{15}) W/mKs for MCO, CCO, SCO, BCO, respectively. κ_l/τ decreases with increase in temperature for all inspected materials. κ_l/τ has the lowest value at 1200 K i.e., higher temperature gives more favorable value of lattice conductivity. At room temperature, we get the value of κ_l/τ to be 2.9, 3.8, 3.30, 4.29 (10^{15}) W/mKs for MCO, CCO, SCO, BCO, respectively.

In order to calculate efficiency of a thermoelectric material, power factor ($PF = \mathcal{S}^2\sigma/\tau$) is considered to be an important parameter. It is seen that the $\mathcal{S}$ and σ rise with the rise of temperature and consequently the *PF* also increases with rising temperature. This point is illustrated in *Figure 3.12b*, in which *PF* increases almost linearly with temperature.

Finally, after calculating the value of *PF* and κ, we have estimated the $ZT = \mathcal{S}^2\sigma T/\kappa$ for $XCeO_3$ to evaluate its possible application in thermoelectric device sectors. An increase in *ZT* is noticed (in *Figure 3.12f*) with increasing temperature and it is found to be 0.64, 0.66, 0.69 0.7 for MCO, CCO, SCO, BCO, respectively at 1200 K. As a result, these *ZT* values obtained are quite high in comparison to a normal TE material. The conclusion we can draw from this is that all XCOs perovskites are wonderful materials for TE applications.

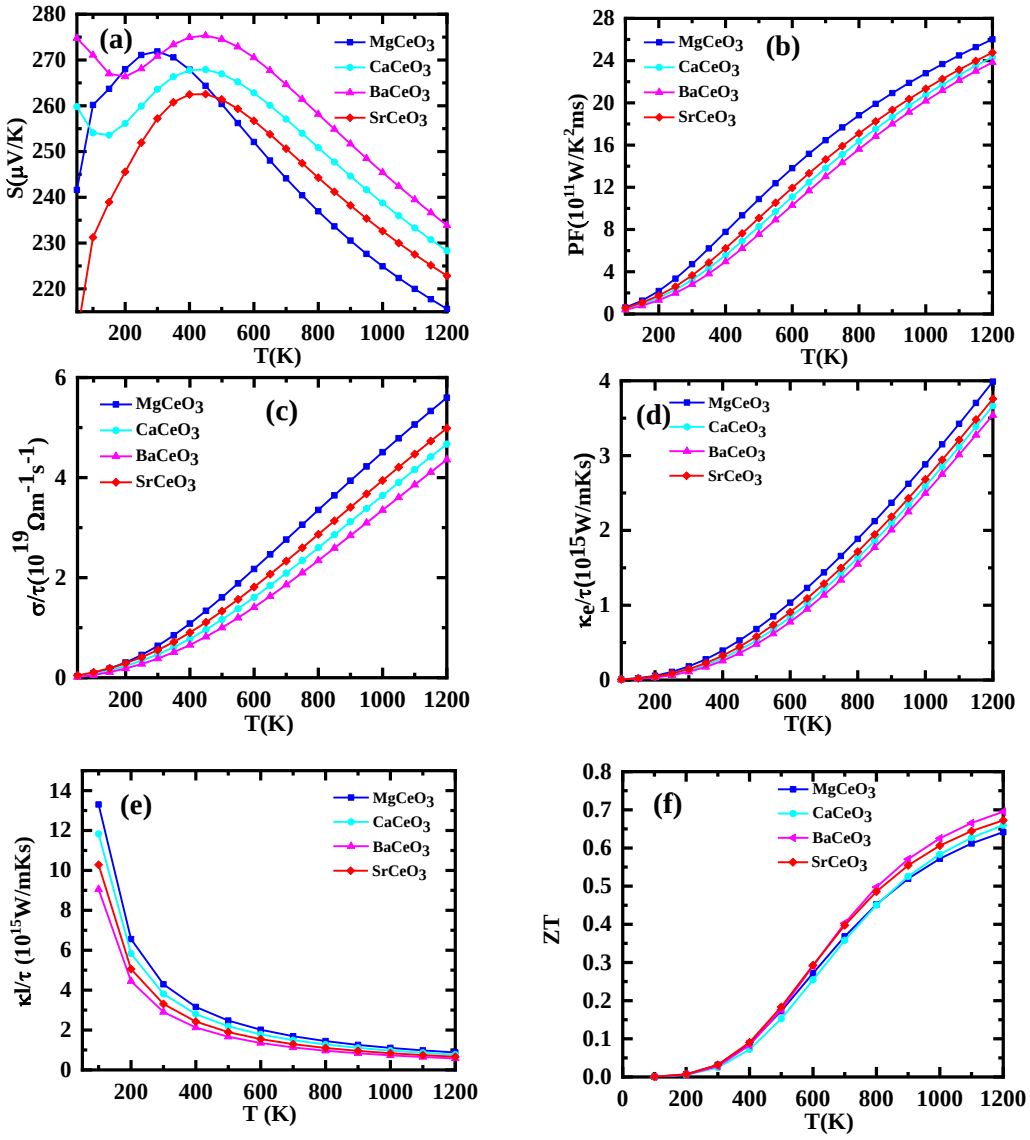

Figure 3.12: Thermoelectric parameters variation with respect to temperature a) Seebeck Coefficient b) Power factor c) Electrical conductivity d) Electronic thermal conductivity e) Lattice thermal conductivity f) Figure of merit

3.4 SUMMARY AND CONCLUSION

We have studied the $XCeO_3$ (X= Mg, Ca, Sr, Ba)perovskite compound to explore its thermophysical and thermoelectric properties using DFT. The different electronic states of $XCeO_3$ show semi-conducting nature with direct band gap values in case of mBJ for MCO, CCO SCO, and BCO are 2.26, 2.6, 2.56, and 2.4 eV, respectively. Thermodynamic and mechanical stability are fulfilled by XCOs. The present

calculations systematically predict a *ZT* value to be 0.64, 0.66, 0.69 0.7 for MCO, CCO, SCO, BCO, respectively at 1200 K. As $XCeO_3$ displays various remarkable properties, therefore it can be the choice of materials experts. Further, our study on $XCeO_3$ opens the scope that compounds may have some potential applications in thermoelectric materials.

REFERENCES

1. Webster, S., Lin, H., Carter III, F.M., Ehmann, K. and Cao, J. "Physical mechanisms in hybrid additive manufacturing: A process design framework." *Journal of Materials Processing Technology* 291 (2021): 117048.
2. Chakraborty, M. and Hashmi, M.S.J. "Wonder material graphene: Properties, synthesis and practical applications." *Advances in Materials and Processing Technologies* 4, no. 4 (2018): 573-602.
3. Sorrell, S. "Reducing energy demand: A review of issues, challenges and approaches." *Renewable and Sustainable Energy Reviews* 47 (2015): 74-82.
4. Frederiks, E.R., Stenner, K., and Hobman, E.V. "Household energy use: Applying behavioural economics to understand consumer decision-making and behaviour." *Renewable and Sustainable Energy Reviews* 41 (2015): 1385-1394.
5. IRENA (2019), *Future of Solar Photovoltaic: Deployment, investment, technology, grid integration and socio-economic aspects (A Global Energy Transformation: paper)*, International Renewable Energy Agency, Abu Dhabi
6. Zabek, D., and Morini, F. "Solid state generators and energy harvesters for waste heat recovery and thermal energy harvesting." *Thermal Science and Engineering Progress* 9 (2019): 235-247.
7. Jaziri, N., Boughamoura, A., Müller, J., Mezghani, B., Tounsi, F. and Ismail, M. "A comprehensive review of Thermoelectric Generators: Technologies and common applications." *Energy Reports* 6 (2020): 264-287.
8. Ong, K.S., Jiang, L. and Lai, K.C. "Thermoelectric energy conversion." (2018): 794-815.
9. Seebeck, T.J. "Magnetic polarization of metals and minerals." *Abhandlungen der Deutschen Akademie der Wissenschaften zu Berlin* 265 (1822): 1822-1823.
10. LaLonde, A.D., Pei, Y., Wang, H. and Snyder, G.J. "Lead telluride alloy thermoelectrics." *Materials today* 14, no. 11 (2011): 526-532.
11. Pei, Y., LaLonde, A., Iwanaga, S. and Snyder, G.J. "High thermoelectric figure of merit in heavy hole dominated PbTe." *Energy & Environmental Science* 4, no. 6 (2011): 2085-2089.

12. Kudman, I. "Thermoelectric properties of p-type PbTe-PbSe alloys." *Journal of Materials Science* 7 (1972): 1027-1029.
13. Sootsman, J.R., He, J., Dravid, V.P., Li, C.P., Uher, C. and Kanatzidis, M.G. "High thermoelectric figure of merit and improved mechanical properties in melt quenched PbTe–Ge and PbTe–Ge_{1-x} Si_x eutectic and hypereutectic composites." *Journal of Applied Physics* 105, no. 8 (2009): 083718.
14. Wang, H., Pei, Y., LaLonde, A.D. and Snyder, G.J. "Weak electron–phonon coupling contributing to high thermoelectric performance in n-type PbSe." *Proceedings of the National Academy of Sciences* 109, no. 25 (2012): 9705-9709.
15. LaLonde, A.D., Pei, Y. and Snyder, G.J. "Reevaluation of $PbTe_{1-x}I_x$ as high performance n-type thermoelectric material." *Energy & Environmental Science* 4, no. 6 (2011): 2090-2096.
16. Wang, H., Pei, Y., LaLonde, A.D. and Snyder, G.J. "Heavily doped p-type PbSe with high thermoelectric performance: an alternative for PbTe." *Advanced Materials* 23, no. 11 (2011): 1366-1370.
17. Kanatzidis, M.G. "Nanostructured thermoelectrics: The new paradigm?. " *Chemistry of Materials* 22, no. 3 (2010): 648-659.
18. Hsu, K.F., Loo, S., Guo, F., Chen, W., Dyck, J.S., Uher, C., Hogan, T., Polychroniadis, E.K. and Kanatzidis, M.G. "Cubic AgPb m SbTe2+ m: bulk thermoelectric materials with high figure of merit." *Science* 303, no. 5659 (2004): 818-821.
19. Zhang, Q., Wang, H., Zhang, Q., Liu, W., Yu, B., Wang, H., Wang, D., Ni, G., Chen, G. and Ren, Z. "Effect of silicon and sodium on thermoelectric properties of thallium-doped lead telluride-based materials." *Nano Letters* 12, no. 5 (2012): 2324-2330.
20. Zhang, Q., Wang, H., Liu, W., Wang, H., Yu, B., Zhang, Q., Tian, Z., Ni, G., Lee, S., Esfarjani, K. and Chen, G."Enhancement of thermoelectric figure-of-merit by resonant states of aluminium doping in lead selenide." *Energy & Environmental Science* 5, no. 1 (2012): 5246-5251.
21. Heremans, J.P., Wiendlocha, B. and Chamoire, A.M. "Resonant levels in bulk thermoelectric semiconductors." *Energy & Environmental Science* 5, no. 2 (2012): 5510-5530.

22. Jaworski, C.M., Wiendlocha, B., Jovovic, V. and Heremans, J.P. "Combining alloy scattering of phonons and resonant electronic levels to reach a high thermoelectric figure of merit in PbTeSe and PbTeS alloys." *Energy & Environmental Science* 4, no. 10 (2011): 4155-4162.
23. Heremans, J.P., Thrush, C.M. and Morelli, D.T. "Thermopower enhancement in PbTe with Pb precipitates." *Journal of Applied Physics* 98, no. 6 (2005): 063703.
24. Pei, Y., LaLonde, A.D., Wang, H. and Snyder, G.J. "Low effective mass leading to high thermoelectric performance." *Energy & Environmental Science* 5, no. 7 (2012): 7963-7969.
25. Blaha, P., Schwarz, K., Sorantin, P. and Trickey, S.B. "Full-potential, linearized augmented plane wave programs for crystalline systems." *Computer physics communications* 59, no. 2 (1990): 399-415.
26. Hohenberg, P. and Kohn, W. “Inhomogeneous electron gas.” *Physical Review* 136, no. 3B (1964): B864.
27. Blaha, P., Schwarz, K., Madsen, G.K.H., Kuasnicke, D. and Luitz, J. "Introduction to WIEN2K." *An Augmented plane wane plus local orbitals program for calculating crystal properties (Vienna university of technology, Vienna, Austria, 2001)* (2001).
28. Kohn, W., and Vashishta, P. "Theory of the inhomogeneous electron gas." *Physics of Solids and Liquids (Springer)* (1983).
29. Perdew, J.P., Burke, K. and Ernzerhof, M. "Generalized gradient approximation made simple." *Physical Review Letters* 77, no. 18 (1996): 3865.
30. Wu, Z. and Cohen, R.E. "More accurate generalized gradient approximation for solids." *Physical Review B* 73, no. 23 (2006): 235116.
31. Csonka, G.I., Ruzsinszky, A., Perdew, J.P. and Grimme, S. "Improved description of stereoelectronic effects in hydrocarbons using semilocal density functional theory." *Journal of Chemical Theory and Computation* 4, no. 6 (2008): 888-891.
32. Monkhorst, H.J. and Pack, J.D. "Special points for Brillouin-zone integrations." *Physical Review B* 13, no. 12 (1976): 5188.
33. Wyckoff R. W. G., *Crystal Structures* 1, 1963 pp 343 Table VIIA.

34. Murali, N., Babu, K.E., Taddesse, P.S., Ramakrishna, A., Parajuli, D., Pramila, R.P.N., Suryanarayana, B., Babu, B.K., Samatha, K. and Veeraiah, V. "Theoretical investigation of structural, electronic, dielectric and optical characteristics of cubic perovskite $BaCeO_3$." *Processing and Application of Ceramics* 15, no. 4 (2021): 351-356.
35. Hasan, M., Nasrin, S., Islam, M.N. and Hossain, A.A. "First-principles insights into the electronic, optical, mechanical, and thermodynamic properties of lead-free cubic ABO_3 [A= Ba, Ca, Sr; B= Ce, Ti, Zr] perovskites." *AIP Advances* 12, no. 8 (2022): 085327.
36. Dar, S.A., Khandy, S.A., Islam, I., Gupta, D.C., Sakalle, U.K., Srivastava, V. and Parrey, K. "Temperature and pressure dependent electronic, mechanical and thermal properties of f-electron based ferromagnetic barium neptunate." *Chinese Journal of Physics* 55, no. 5 (2017): 1769-1779.
37. Dar, S.A., Srivastava, V., Sakalle, U.K. and Pagare, G. "Insight into structural, electronic, magnetic, mechanical, and thermodynamic properties of actinide perovskite $BaPuO_3$." *Journal of Superconductivity and Novel Magnetism* 31, no. 10 (2018): 3201-3208.
38. Dar, S.A., Srivastava, V., Sakalle, U.K., Ahmad Khandy, S. and Gupta, D.C. "A DFT study on structural, electronic mechanical and thermodynamic properties of 5f-electron system $BaAmO_3$." *Journal of Superconductivity and Novel Magnetism* 31 (2018): 141-149.
39. Dar, S.A., Srivastava, V., Sakalle, U.K. and Parey, V. "Ferromagnetic phase stability, magnetic, electronic, elasto-mechanical and thermodynamic properties of $BaCmO_3$ perovskite oxide." *Journal of Electronic Materials* 47 (2018): 3809-3816.
40. Dar, S.A., Srivastava, V., Sakalle, U.K. "A first-principles calculation on structural, electronic, magnetic, mechanical, and thermodynamic properties of $SrAmO_3$." *Journal of Superconductivity and Novel Magnetism* 30, no. 11 (2017): 3055-3063.
41. Dar, S.A., Srivastava, V., Sakalle, U.K., Rashid, A., Pagare, G. First-principles investigation on electronic structure, magnetic, mechanical and thermophysical

performances of $SrPuO_3$ perovskite oxide. *Materials Research Express* 5, no. 2 (2018): 026106.

42. Fan, L., Zhu, B., Chen, M., Wang, C., Raza, R., Qin, H., Wang, X., Wang, X. and Ma, Y. “High-performance transition metal oxide composite cathode for low-temperature solid oxide fuel cells”, Journal of Power Sources 203 (2012): 65–71.
43. Huang, Z.W., Zhao, Y.H., Hou, H. and Han, P.D. "Electronic structural, elastic properties and thermodynamics of $Mg_{17}Al_{12}$, Mg_2Si and Al_2Y phases from first-principles calculations." *Physica B: Condensed Matter* 407, no. 7 (2012): 1075-1081.
44. Han, W.D., Li, K., Hu, F., Li, X.D. and Dai, J. "First-principle investigation of the structural, electronic, elastic, and elastic anisotropy properties and thermal stabilities of $CeMg_2Si_2$ and Mg_2Si." *Materials Research Express* 6, no. 11 (2019): 1165f8.
45. Yakoubi, A., Baraka, O. and Bouhafs, B. "Structural and electronic properties of the Laves phase based on rare earth type BaM_2 (M= Rh, Pd, Pt)." *Results in Physics* 2 (2012): 58-65.
46. Jamal, M., Bilal, M., Ahmad, I. and Jalali-Asadabadi, S. "IRelast package." *Journal of Alloys and Compounds* 735 (2018): 569-579.
47. Bhat, T.M. and Gupta, D.C. "Robust thermoelectric performance and high spin polarisation in CoMnTiAl and FeMnTiAl compounds." *RSC Advances* 6, no. 83 (2016): 80302-80309.
48. Sin’Ko, G. V., and Smirnov, N. A. "Ab initio calculations of elastic constants and thermodynamic properties of bcc, fcc, and hcp Al crystals under pressure." *Journal of Physics: Condensed Matter* 14, no. 29 (2002): 6989.
49. Mehl, M.J., Klein, B.M. and Papaconstantopoulos, D.A. "Intermetallic compounds: principle and practice." *Principles* 1 (1995): 195-210.
50. Voigt, W. "*Lehrbuch der Kristallphysik (Textbook of crystal physics)*." BG Teubner, Leipzig und Berlin (1928).
51. Schreiber, E., Anderson, O.L., Soga, N. and Bell, J.F. "Elastic constants and their measurement." (1975): 747-748.
52. Hill, R. "The elastic behaviour of a crystalline aggregate." *Proceedings of the Physical Society. Section A* 65, no. 5 (1952): 349.

53. Reuss, A. J. Z. A. M. M. "Calculation of the flow limits of mixed crystals on the basis of the plasticity of monocrystals." *Z. Angew. Math. Mech* 9 (1929): 49-58.
54. Mayer, B., Anton, H., Bott, E., Methfessel, M., Sticht, J., Harris, J. and Schmidt, P.C. "Ab-initio calculation of the elastic constants and thermal expansion coefficients of Laves phases." *Intermetallics* 11, no. 1 (2003): 23-32.
55. Haines, J., Leger, J.M. and Bocquillon, G. "Synthesis and design of superhard materials." *Annual Review of Materials Research* 31, no. 1 (2001): 1-23.
56. Pugh, S. F. "XCII. Relations between the elastic moduli and the plastic properties of polycrystalline pure metals." *The London, Edinburgh, and Dublin Philosophical Magazine and Journal of Science* 45, no. 367 (1954): 823-843.
57. Liu, X., Fu, J. and Chen, G. "First-principles calculations of electronic structure and optical and elastic properties of the novel ABX_3-type $LaWN_3$ perovskite structure." *RSC Advances* 10, no. 29 (2020): 17317-17326.
58. Blanco, M.A., Francisco, E. and Luana, V., 2004. "GIBBS: isothermal-isobaric thermodynamics of solids from energy curves using a quasi-harmonic Debye model." *Computer Physics Communications* 158, no. 1 (2004): 57-72.
59. Otero-de-la-Roza, A., Abbasi-Pérez, D. and Luaña, V. "Gibbs2: A new version of the quasiharmonic model code. II. Models for solid-state thermodynamics, features and implementation." *Computer Physics Communications* 182, no. 10 (2011): 2232-2248.
60. Otero-de-la-Roza, Alberto, and Luaña, V. "Gibbs2: A new version of the quasi-harmonic model code. I. Robust treatment of the static data." *Computer Physics Communications* 182, no. 8 (2011): 1708-1720.
61. Petit, A.T., Dulong, P.L. “Study on the measurement of specific heat of solids.” *Ann Chim Phys* 10 (1819): 395
62. Pei, Y., Wang, H. and Snyder, G.J. "Band engineering of thermoelectric materials." *Advanced Materials* 24, no. 46 (2012): 6125-6135.
63. Pei, Y., Wang, H., Gibbs, Z.M., LaLonde, A.D. and Snyder, G.J. "Thermopower enhancement in $Pb_{1-x}Mn_xTe$ alloys and its effect on thermoelectric efficiency." *NPG Asia Materials* 4, no. 9 (2012): e28-e28.
64. Allen, P. "Boltzmann theory and resistivity of metals." *Kluwer International Series in Engineering and Computer Science* (1996): 219-250.

65. Ziman, John M. *Electrons and phonons: the theory of transport phenomena in solids.* Oxford university press, 2001.
66. Hurd, C. “The Hall Effect in Metals and Alloys.” *Plenum Press.* 1972.
67. Morelli, D.T. and Slack, G.A. "High lattice thermal conductivity solids." *High thermal conductivity materials* (2006): 37-68.
68. Bjerg, Lasse, Bo B. Iversen, and Georg KH Madsen. "Modeling the thermal conductivities of the zinc antimonides ZnSb and Zn_4Sb_3." *Physical Review B* 89, no. 2 (2014): 024304.
69. Julian, C.L. “Theory of heat conduction in rare-gas crystals.” *Physical Review* 137, no. 1A (1965): A128.

CHAPTER 4

STRUCTURAL, ELECTRONIC, MAGNETIC, THERMODYNAMIC, AND THERMOELECTRIC PROPERTIES OF $RFeO_3$ (R = Nd, Pr)

4.1 INTRODUCTION

Perovskite structure gives rise to a new class of compound, rare-earth ferrites, $RFeO_3$ where R is a rare earth element. In the crystal lattice, $RFeO_3$ there are mainly three main interactions: R-O-Fe, Fe-O-Fe, and R-O-R. Their tremendous properties of charge ordering [1], colossal magnetoresistance [2], orbital ordering [3], multiferroic [4], and strong correlation between electrical, structural, and magnetic properties [5, 6] encourages us to explore these kinds of compounds. This places a ground for their usage in memory, and spintronics devices, fuel cells, solid oxides, gas sensors [7-10]. The electron systems of transition metals 3d and rare earth 4f orbitals are strongly attracted to one another due to strong coulombic attraction. Various physical properties such as electronic, optical, thermodynamic and thermoelectric, ferromagnetic, etc. are dependent on the crystal structure of the compound and the arrangement of the atoms within the compound. By flipping the FeO_6 octahedra, these characteristics can be changed [11-13]. The high catalytic and gas sensitivity properties of the $NdFeO_3$ (NFO) nano-crystalline perovskite oxide have been demonstrated [14, 15]. These characteristics are crucial in the scientific fields to identify undesirable gas leaks, consequently lowering pollution levels and safeguarding the environment. Moreover, $RFeO_3$'s structural characteristics are influenced by the type and quantity of doping metals. For the sample with 30% Ni-doping, the optical energy bandgap of NFO falls from 4.3 to 4.0 eV with Ni substitution [16]. With Mn doping in $PrFeO_3$ (PFO), ac conductivity and dielectric constant rise [17]. PFO's low dielectric loss and large dielectric constant make it look like a sensible option for the microelectronic industry [17]. PFO has been used in dyes and inorganic pigments [18, 19], as well as magnetic field materials [20-22], and photocatalysis [23-25]. Half metallicity is becoming prominent and observed in many

compounds [26-35], showing that one spin behaves metallic while the other behaves either as a semiconductor or insulator at the fermi level. These kinds of characters have potential applications in spintronics and spin value generators [10]. Groot et.al [26, 27] were the ones who initially suggested the idea of half-metallic ferromagnets in XMnSb half-Heusler alloys and this provides ground to search half-metallicity in other compounds like Perovskites [28], Half Heusler [29], full Heusler alloys [30], wurtzite's [31], magnetite [32-34], zinc blende [35], etc.

The literature research provided the foundation for us to perform a thorough evaluation of the $RFeO_3$ (R = Pr, Nd) perovskites. A theoretical investigation is necessary to properly harness the characteristics of the researched compounds. We have worked on electronic, magnetic, thermodynamic, and thermoelectric details of $PrFeO_3$ and $NdFeO_3$ in their cubic phase. Previous research has shown that employing the modified Becke-Johnson (mBJ) potential [36, 37] results in superior electrical characteristics of half-metallic (HM) compounds This paper provides methodical details about the properties in different sections. To begin, section 4.1 initiates with an introduction to $RFeO_3$ perovskite. Secondly, Section 4.2 describes the methodology and procedures used for calculations, and afterward, Section 4.3 provides discussions of the obtained results and is finally concluded in the last section.

4.2 COMPUTATIONAL DETAILS

DFT [38] has been used to calculate attributes such as structural, magnetic, electronic, thermodynamic, and thermoelectric as a single unit in the Wien2K algorithm [39]. We have adopted GGA [40], TB-mBJ and mBJ+U [41] as exchange-correlation (XC) potential for band structure calculations. And rest of the properties have been calculated using mBJ+U (U is coulombic potential). FPLAPW is utilized for structure generation of RFO. This method divides unit lattice into interstitial and atomic regions which utilize plane wave basis and spherical harmonics in their respective region. We need to solve the many bodies electron problem with consideration of approximation to XC potential. The XC in the GGA scheme depends on the local e^- spin densities and their gradients. One issue is that GGA functionals retain the self-interaction error [42] but lacks derivative discontinuity, which is crucial when comparing the KS band gap. GGA underestimates the value of the bandgap and fails

to match the experimental values. It allures us to work on other hybrid XCs and GW functionals. On the other hand, mBJ is the semi-local electron XC potential having derivative discontinuity which acts as a screening and increases the bandgap. mBJ achieves on average an accuracy even better than that of hybrid functionals and at a substantially lower computing cost, making it to be the best semi-local approximation for determining band gaps. mBJ+U is even cheaper in which coulombic potential U is applied only to localized states, especially 3d and 4f states. A set of K points is generated by tetrahedron method [43]. A mesh of 1000 *K* points with $R_{MT\ X}\ K_{max}$, L_{max}, and G_{max} is set to be 7, 10, and 12, respectively. Our compounds contain strongly correlated 4*f* (Nd/Pr) and 3*d* (Fe) states, that's why we have used mBJ+U for calculations of rest of the properties.

4.3 RESULTS AND DISCUSSION

The evaluated parameters of RFOs are described below in sub-sections parts within this section.

4.3.1 Structural Properties

The considered atomic position for Nd/Pr is (0, 0, 0), for Fe is (0.5, 0.5, 0.5) and for oxygen atoms are (0.5, 0.5, 0), (0, 0.5, 0.5) and (0.5, 0, 0.5). Their muffin tin radius R_{MT}s are 2.5 (Nd/Pr), 1.96 (Fe), and 1.69 (O). These crystal structures are optimized in cubic phase Pm-3m (221) wherein volume is tuned by applying compression from -15 to +15. The crystal structure representing the atomic positions and octahedra FeO_6 is presented in *Figure 4.1*. Lattice constants a for NFO and PFO are optimized around equilibrium volume and their optimized value is presented in *Table 4.1* and found in synchronous with experimental values [44-46]. Energy-Volume (E-V) curves for NFO and PFO, fitted using Birch Murnaghan eos [47], are shown in *Figure 4.2* in ferromagnetic as well as non-magnetic phase and their corresponding ground state values are presented in *Table 4.1*. Concluding, these compounds have shown stability in the ferromagnetic phase. Bulk modulus and its pressure derivative, and volume in the ferromagnetic and non-magnetic phases are presented in *Table 4.1*. Formation (E_{form}) and cohesive (E_{coh}) energies are crucial parameters in determining the

compound feasibility and ascertainment of their formation. Cohesive and formation energies are determined using formulas shown in *equations (4. 1), (4.2)* [48-50].

$$E_{form} = \frac{\{E_{RFO} - (E_R + E_{Fe} + 3E_o)_{solid}\}}{n} \quad (4.\ 1)$$

$$E_{coh} = \frac{\{(E_R + E_{Fe} + 3E_O)_{atom} - E_{RFO}\}}{n} \quad (4.2)$$

where E_{RFO}, E_R, E_{Fe}, E_O are the energies of whole compound, R i.e., Pr, Nd, Fe and O. Negative value of formation energy indicates NFO and PFO compounds can be synthesized easily in the laboratory. Formation and Cohesive energies for RFOs are presented in *Table 4.1*. Higher cohesive value represents strong coulombic interaction between Nd/Pr and Fe atoms which represent magnetic interaction and hybridization among constituent atoms.

Tolerance factor t, which analyzed the symmetry of the structure is determined using Goldschmidt's formula [51] through an ionic radius of elements and bond lengths.

$$t = \frac{r_X + r_O}{\sqrt{2}(r_{Fe} + r_O)} = \frac{\langle X - O \rangle}{\sqrt{2}\langle Fe - O \rangle} \quad (4.3)$$

In equation (4.3), r_X, r_{Fe}, r_O is the ionic radius of the X (X=Pr, Nd), Fe and O ions which is 0.98 Å (Nd), 0.99 Å (Pr), 0.59 Å (Fe) and 1.35 Å (O) [50]. <X-O> and <Fe-O> are the bond length between X and O atoms, and Fe and O atoms, respectively. For cubic perovskites, we found the anticipated value of t to be between 0.8 and 1. [45, 52].

4.3.2 Electronic Properties

Band structures are plotted for exchange-correlation PBE, mBJ, and mBJ+U. PBE-GGA is observed to undervalue the bandgap of several compounds because of the presence of self-interaction error. These values could be corrected by analyzing data in exchange potentials like mBJ and mBJ+U. *Figure 4.3* represents the band structure plot for PFO and NFO in PBE, mBJ, and mBJ+U functionals. We found that both the compounds NFO and PFO are showing metallic character in both states of spin for PBE functional while in the case of mBJ and mBJ+U, a shift in bands is observed in the spin-down case resulting in creation of a bandgap of 2.0eV (PFO) and 1.8eV (NFO). In spin-up states, the fermi level is completely populated, indicating their metallic nature. In contrast, spin-down states show a gap between conduction band

and the valence band, demonstrating their semiconductor nature. From this, we interpret that PFO and NFO have changed their character from completely metallic to half-metallic on the application of mBJ+U making them applicable for applications in spintronic devices.

Table 4.1: Parameters like Lattice parameter *a* (Å), volume *V* (a.u^3), Ground state energy E_0 (Ry), Bulk modulus *B* (GPa), Bulk pressure in Ferromagnetic & Non-magnetic phase, Curie Temperature T_c (K), Formation energy E_{form} (KJ/mol), and Cohesive energy E_{coh} (eV) Tolerance factor *t*, and Bond lengths (Å).

Parameters		**PrFeO3**		**NdFeO3**	
		FM	**NM**	**NM**	**FM**
	Present	3.8389	3.7616	3.7474	3.8341
a(Å)	**GGA**	3.762[a]		3.754[a]	
	Expt.	3.887[b]		3.870[b]	
V(a.u)^3		381.7792	359.1734	355.1359	380.3562
B(GPa)		155.5049	209.4571	230.8959	157.0536
B.P		3.3001	4.4844	7.6272	4.5456
E_0(Ry)		-21483.1126	-21483.0363	-22257.5120	-22257.6737
ΔE_{NM-FM}(Ry)		0.076345		0.161761	
T_C(K)		1290		1471	
E_{form} (eV/atom)		-2.561		-2.676	
E_{coh} (eV/atom)		6.24		6.43	
Eg (↓) (eV)		2.0		1.8	
t	**GGA**	0.99		0.99	
	Ionic method	0.849		0.852	
Bond lengths (Å)	**R-Fe**	3.53		3.52	
	Fe-O	2.04		2.03	
	Pr-O	2.88		2.88	

Further, we have plotted a graph for the total and partial density of states against energy for PFO and NFO in *Figure 4.4* which shows that in spin down case, maxima of the valence region and minima of the conduction region are due to O-p and Nd/Pr-*f*, respectively. In spin-up states, both perovskites under consideration, major contribution at fermi level is from Pr/Nd-*d*. In comparison to Pr and Nd, O's contribution is negligible at fermi level E_F. Fe input is insignificant at the fermi level.

Fe-*d* and O-*p* states are present below fermi level which shows the covalent interactions between these two atoms. Fe and O show strong hybridization in spin-up as well as spin down states. Figure shows that peak value increases on going from PFO to NFO. Maximum value of peaks is due to Pr-*f* and Nd-*f* states. The maximum peak for PFO and NFO is located at 1.9 and 2.6 eV for spin up states and located at 1.5 and 2.5 eV for spin down states, respectively. Maximum density of electrons is presented at these peaks.

Spin polarization *P* of electron at E_F is determined from equation (4. 4) [53].

$$P = \frac{\rho\uparrow(E_F) - \rho\downarrow(E_F)}{\rho\uparrow(E_F) + \rho\downarrow(E_F)} \qquad (4.\ 4)$$

where, $\rho\uparrow(E_F)$ and $\rho\downarrow(E_F)$ are the densities of spin up and down states at E_F, respectively. 100% spin polarisation for NFO and PFO perovskites is observed when columbic potential is applied.

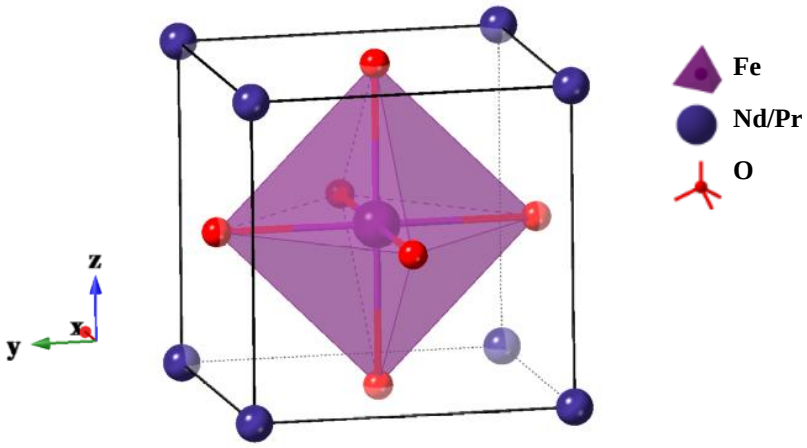

Figure 4.1: Structural diagram of Nd/$PrFeO_3$

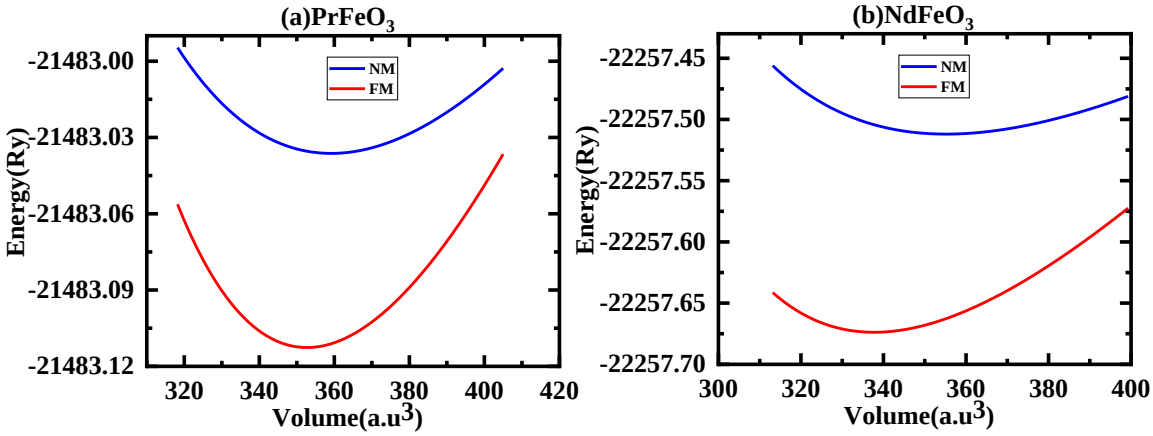

Figure 4.2: Volume Optimization graph for $PrFeO_3$ and $NdFeO_3$

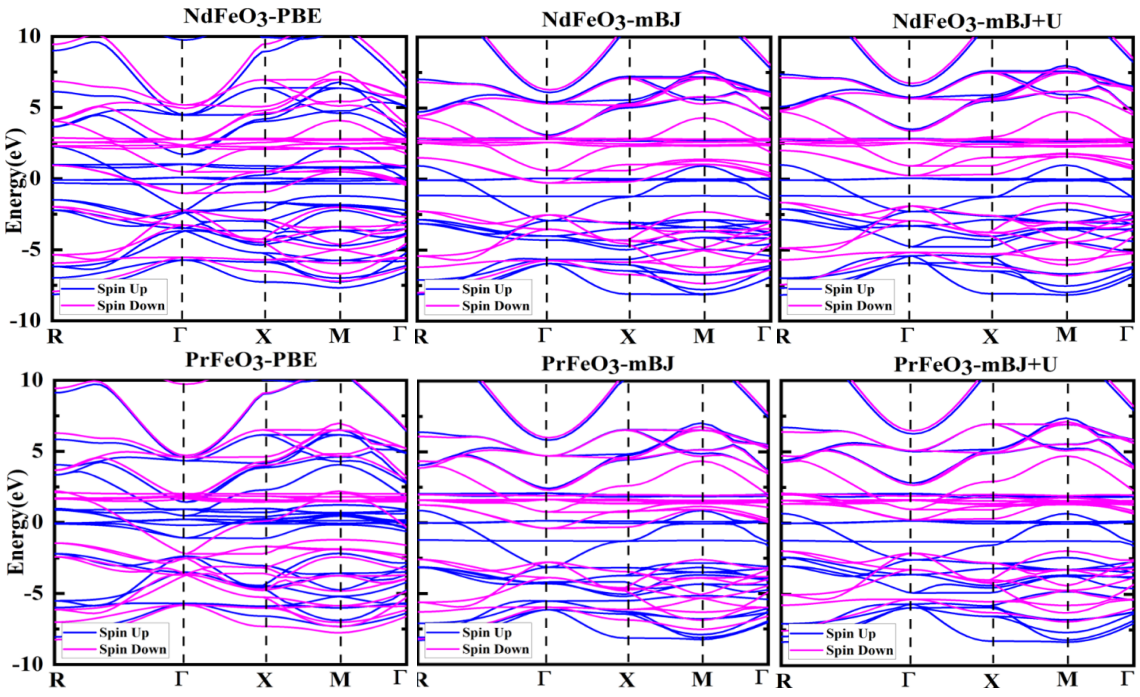

Figure 4.3: Band structure diagram for $NdFeO_3$ and $PrFeO_3$ in PBE, mBJ, mBJ+U in spin up (blue color lines) & down (pink colour lines)

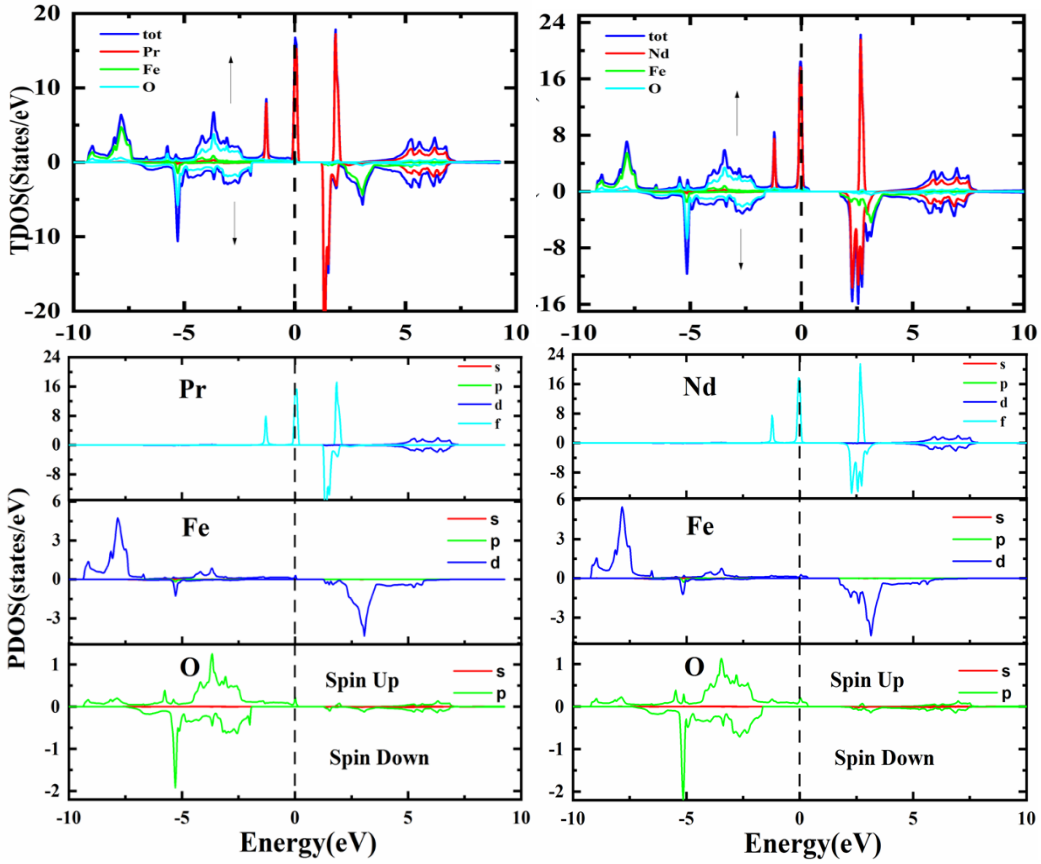

Figure 4.4: TDOS and PDOS plot for $PrFeO_3$ and $NdFeO_3$ in spin up and down

4.3.3 Magnetic Properties

Total and partial magnetic moments for RFOs are presented in *Table 4.2*. Total magnetic moment is the sum of the magnetic moment (MM) of each atom and interstitial region. Major contribution to magnetic moment is from Fe while contribution from oxygen atom is the least. The total magnetic moment of PFO ($7\mu_B$) and NFO ($8\mu_B$) is integral which belongs to half metallic [54]. The calculated MM of Fe in PFO and NFO are $4.24\mu_B$ and $4.21\mu_B$, respectively. The difference in their MM is very small which illustrates there is no transfer of charge from O to Fe. Moreover, as a result of exchange correlation function from GGA to mBJ+U, magnetic contribution of Fe atoms is increased. *Table 4.2*, clears that MM of Nd is more than Pr. This means NFO is having stronger magnetic behavior than PFO. The positive value of MM of Fe, O, and interstitial represents that they are aligned parallel to Nd/Pr.

Curie temperature (T_C), is a significant parameter, for estimating magnetic behavior of materials. Certain materials lose their permanent magnetism with induced magnetism at T_C. We have calculated T_c for PFO and NFO using Mean Field Approximation (MFA) inside the limits of the Heisenberg model [55]. The formula for calculation uses the energy variance amongst non-magnetic and ferromagnetic phases (ΔE_{NM-FM}), which is shown in equation (4.5).

$$T_C = \frac{2\Delta E_{NM-FM}}{3K_B} \tag{4.5}$$

where K_B is the Boltzmann constant. Their values are presented in *Table 4.1* and all are above room temperature. This means PFO and NFO have potential applications in spintronics. Half-metallic ferromagnets with T_C much beyond room temperature are widely desirable, and the current compound may serve as a possible contender for spintronics and magneto-electronic devices [55].

Table 4.2: Total, Interstitial, Individual elements' Magnetic Moments (in Bohr magneton μ_B) for $PrFeO_3$ and $NdFeO_3$ using PBE, mBJ and mBJ+U

Compound	**$PrFeO_3$**			**$NdFeO_3$**		
Configuration	**PBE-GGA**	**mBJ**	**mBJ+U**	**PBE-GGA**	**mBJ**	**mBJ+U**
M_{tot}	5.1670	6.5013	7.00	7.2267	7.65	8.0008
$M_{Interestial}$	0.2679	0.1599	0.1634	0.4427	0.1175	0.1121
$M_{Pr/Nd}$	2.0860	2.1068	2.0053	3.1593	3.2539	3.1568
M_{Fe}	2.6202	3.7069	4.2427	3.3295	3.7354	4.2175
M_O	0.0642	0.1758	0.1963	0.0984	0.1832	0.1714

4.3.4 Thermodynamic Properties

The thermodynamic stability of RFO compounds must be checked to ensure their applicability and the possibility of their manufacture in the industry. Consequently, the thermodynamic properties of RFOs corresponding to temperature (0-1200 K) and pressure (0- 40 GPa) are analyzed in *Figure 4.5*. Parameters include entropy S, heat capacity C_V, Grüneisen parameter γ, Debye temperature θ_D and thermal expansion coefficient α. All these parameters are examined via Quasi Harmonic Debye model as incorporated in Gibbs2 code [56-58] inbuilt within WIEN2K software [39].

The first and foremost parameter, entropy *S* which describes the degree of disorder and randomness within the material on application of temperature has been analyzed in *Figures 4.5a, 4.5b* for PFO, NFO. We can see that entropy is 0 at zero K which obeys the third law of thermodynamics. As temperature increases, *S* increases exponentially i.e., temperature contributes to the disturbances in the material. While pressure had a reverse effect on *S*, its increment decreases the *S* i.e., at higher pressure *S* behaves more orderly.

Heat capacity CV variation with temperature and pressure are shown *Figure 4.5(c, d)* for (PFO, NFO). CV explains the lattice vibrations, phase transformation, and heat storage capacity of the solids. At lower temperatures, the CV curve follows T^3 behavior identical to the Debye-T^3 law. At higher temperature, it reaches saturation

point and become almost constant. This saturation point represents the Dulong- Petit limit [59]. Its value is 73.8 and 73.6 J/mol K for PFO and NFO, respectively.

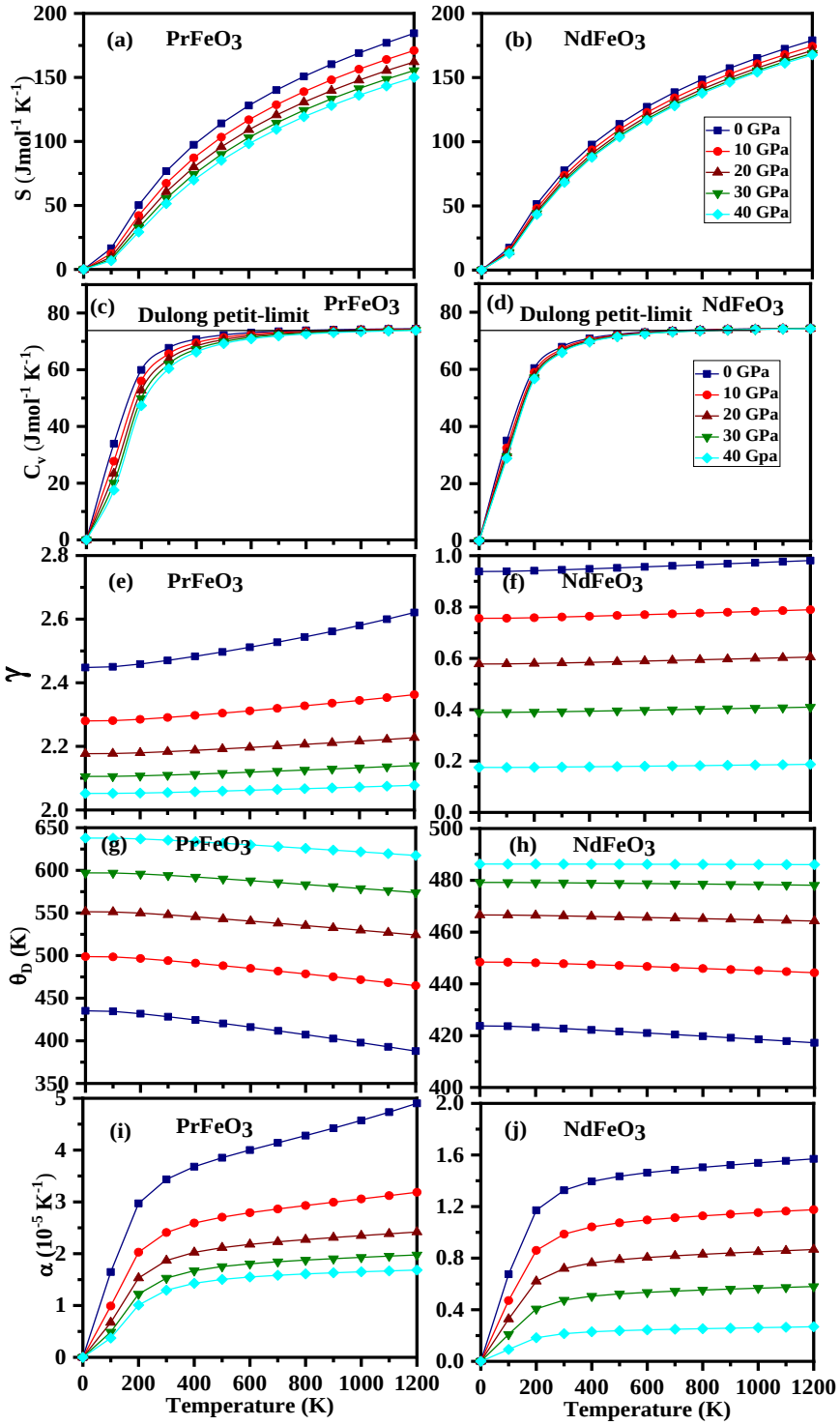

Figure 4.5: Thermodynamic parameters: Entropy (a, b), Specific heat (c, d) Grüneisen parameter (e, f), Debye temperature (g, h), Thermal expansion coefficient (i, j) for PFO and NFO

Grüneisen Parameter γ is a significant thermodynamic parameter that explains the anharmonicity due to temperature and pressure within the solid. Its plot corresponding to *T* is shown in *Figure 4.5e, 4.5f* for PFO, NFO, respectively which illustrate a slow increment in its value with respect to temperature while a rapid decrement is observed with respect to pressure. γ for room temperature and zero pressure are 2.47 (PFO) and 0.94 (NFO).

Debye temperature θ_D is plotted in *Figure 4.5(g, h)* explicates the vibrational effects in the solid. Below θ_D, quantum effects are more dominating, while above θ_D, quantum effects lose dominance. By examining *Figure 4.5(g, h)*, one can say with temperature θ_D decreases slowly while with pressure θ_D increases significantly for both PFO and NFO. θ_D at 0 GPa for 300 K are 428 K and 423 K for PFO and NFO, respectively.

Finally, we have shown consequences of *T* on thermal expansion coefficient α for RFO in *Figure 4.5(i, j)*. With temperature, it increases linearly till 200 K beyond that its increase is unhurried. This explains that temperature results in expansion of solid due to motion of the particles within the solid. Pressure shows opposite behaviour it reduces the value of α. The highest value of α is observed at the lowest pressure. The value of α for PFO and NFO at 300 K and 0 GPa is 3.4 and 1.3 (10^{-5}/K), respectively.

4.3.5 Thermoelectric Properties

Furthermore, we have investigated the transport behavior of both the perovskites by using mBJ+U because it results in making the compound half-metallic. Seebeck coefficient, electrical conductivity, electronic thermal conductivity, power factor, and figure of merit are evaluated with respect to chemical potential (μ-E_F) in the -2 to 2eV for temperatures 300 K, 600 K, 900 K, and 1200 K. Positive region corresponds to n-type doping while negative corresponds to p-type doping. All thermoelectric calculations are evaluated via the Boltzmann transport phenomenon [60-63], inhibited in BoltzTrap program [63] with considering constant relaxation time τ.

Seebeck coefficient ($\mathcal{S}$) and electrical conductivity (σ) plots corresponding to chemical potential are revealed in *Figure 4.6(a, b)* and *Figure 4.6(c, d)*, respectively. Seebeck coefficient measures the amount of thermovoltage generated due to differences in the temperature across the compound. For lower of μ, the value of the

Seebeck coefficient decreases with temperature while it increases later at higher value of μ. For both the perovskites, Spin-up states are found only in the positive region of μ i.e., spin-up states are the result of n-type of doping. For spin-down states in the case of PFO, p-type contributes more than n-type while in NFO equal contribution of both types of doping is seen. At the fermi level E_F, only spin-down states contribute and show that S increases for PFO and decreases for NFO with the rise in *T*.

Similarly, σ/τ in *Figure 4.6c* and *4.6d* are for PFO and NFO, respectively. It provides information about the flow of charges from higher to lower temperature gradients. For PFO (*fig 4.6c*) Spin-up states, σ/τ are found to be active only below EF with two peaks obtained at -2 and -1 eV with values equivalent to 4.3 and 3.5 (10^{20} /Ωms), respectively. Spin-down states contribute to both n and p regions with maximum values of σ/τ *equ*al to 0.78 and 0.64 (10^{20} /Ωms) obtained at -2eV and 1.5 eV, respectively. A similar kind of behavior of σ/τ is observed for spin-down states of NFO in *fig 4.6d* but peaks obtained at -2 and 2 eV are 1.9 and 1.24 (10^{20} /Ωms). Here, Spin-up states also contribute in both the n and p regions with three peaks obtained at -2, -0.9, and 0.06 eV are 4.43, 3.87, and 1.31 (10^{20} /Ωms). At the fermi level, σ/τ increases with temperature for PFO while decreasing for NFO.

Thermal conductivity (κ) is the measure of heat transfer or conductance due to electrons' movement and lattice vibrations. So, thermal conductivity consists of electronic (κ_e) and lattice thermal conductivity (κ_l). *Figure 4.6(e, f)* presents the plot w.r.t chemical potential μ of electronic thermal conductivity for PFO as well as NFO. The optimum values for PFO in spin-up states for p-type region are 2.12, 6.38, 9.4, and 12.5 (10^{15} W/mKs) and for n-type region are 0.23, 0.29, 0.32, 0.35 (10^{15} W/mKs) at 300, 600, 900, and 1200 K, respectively. This shows that κ_e is increasing drastically with temperature. While for spin-down case its maximum value for p-type region is 0.48, 1.23, 2.3, and 3.8 (10^{15} W/mKs) and for n-type region are 0.26, 0.77, 1.67, and 2.93 (10^{15} W/mKs) at 300, 600, 900, and 1200 K. In the spin-down case, we obtained the increasing trend but not with much high value as in spin-up states. κ_e for NFO with respect to μ is shown in *Figure 4.6f*. Here, we have seen similar kind of trend with μ and T as in PFO graph but optimum values are at a bit higher place in p-type region than PFO. They are 3.25, 6.5, 10.14, 13.7 (10^{15} W/mKs) (spin-up) and 1.36, 2.64, 4.25, 5.79 (10^{15} W/mKs) (spin-down) at 300, 600, 900, and 1200 K,

respectively. The κ_e is almost 10^{15} W/mKs at 300 K which is quite low and makes them applicable for thermoelectric materials.

Power factor PF is the parameter helpful in measuring the efficacy of investigated materials. Mathematically, it is expressed in terms of S and σ/τ as $PF = S^2\sigma/\tau$. Its plot corresponding to temperature and chemical potential is shown in Figure 4.6g and 4.6h for PFO and NFO, respectively. For PFO-Spinup, the value of PF is maximum and increases with temperature from 300 to 1200 K in the -1 to +1 eV region while decreasing in other areas. For the Spin-down PFO case, *PF* is active in -μ region (-2.0 to -1.0 eV) and +μ region (0.5 to 2eV) and is found to be increasing with temperature. *Figure 4.6h* represents the PF variation with T and μ for NFO. For the Spin-up case, three peaks are observed in which two peaks in the region of -1 to +1 show an increment with temperature and one peak in -1.5 to -1 eV show a reverse effect with temperature. It is due to the decrement in *S* and σ/τ in -μ region. For the Spin-down case, *PF* increases with temperature and is found only at extreme end i.e -2 to -1 eV (-μ region) and 1 to 2 eV (+μ region). For both the perovskites, both spins are found to be active in p-type and n-type regions.

Lattice thermal conductivity κ_l which contributes to total thermal conductivity and represents lattice vibration due to heat conduction within the solids. Its calculation is done using slack approach [64]. The equation is modified by Julian [65], Leibfried and Schlomann [66]. κ_l take place an important role in increasing thermoelectric efficiency. *Figure 4.7a* and *4.7b* shows the κ_l/τ and κ_e/τ behavior with respect to temperature for PFO and NFO. Lattice conductivity decreases with temperature while total thermal conductivity increases with temperature at E_F. *Figure 4.7c* shows the Total κ variation with the *T*, illustrating that at lower temperature lattice conductivity is dominates while at higher temperatures electronic conductivity dominates.

Finally, figure of merit (also known as thermoelectric efficiency) *ZT* demonstrated in *Figure 4.7d* for PFO and NFO perovskites and expressed as

$$\mathrm{ZT} = \frac{\mathrm{PF}}{\kappa/\tau}\mathrm{T} \tag{4.6}$$

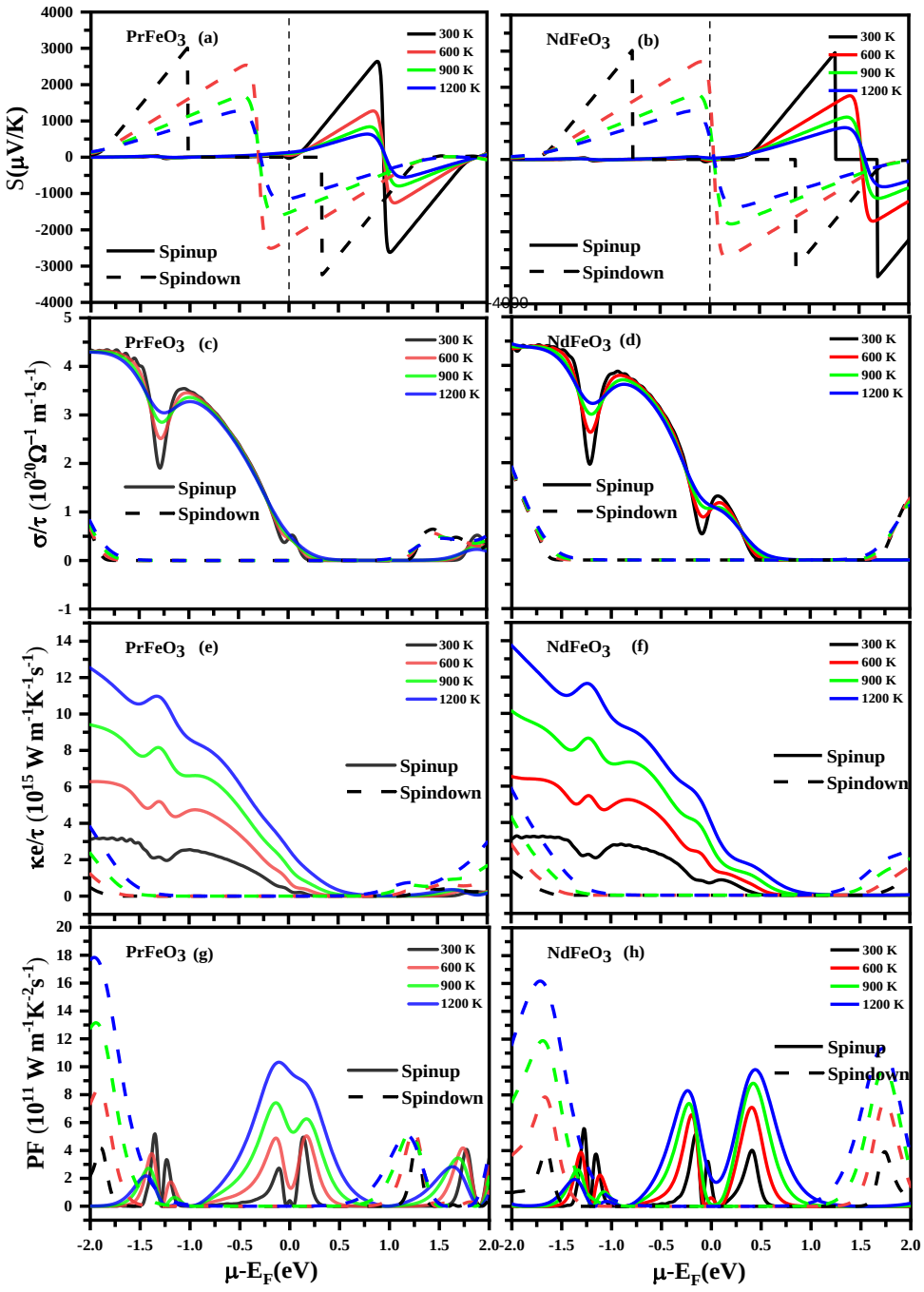

Figure 4.6: (a, b) Seebeck coefficient, (c, d) Electrical conductivity, (e, f) Electronic thermal conductivity, (g, h) Power factor

This is the crucial parameter in defining the efficiency of thermoelectric materials. Ideal value of *ZT* for its application in industry is considered to be ≈ unity. Thermoelectric materials are useful in conversion of waste heat (unused heat) into electricity via Seebeck effect which is based on the production of thermal voltage owing to difference in the *T* across the solid. *Figure 4.7d* shows that as temperature increases *ZT* increases for PFO and its maximum value obtained is 0.38 at 1200 K. While we see that NFO shows oscillatory behavior and its increment corresponding to temperature is very less and only reaches 0.05 at 1200 K. So, we interpret only PFO can be used in future as thermoelectric material.

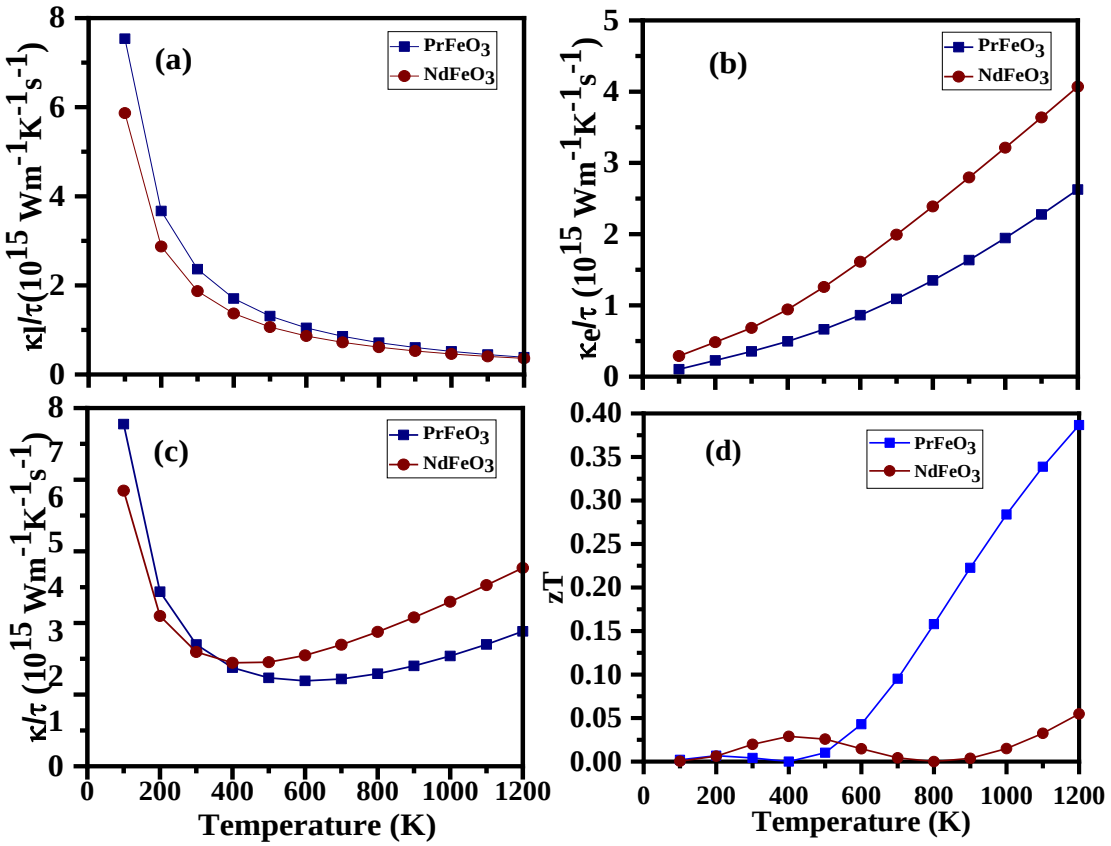

Figure 4.7: (a) Lattice thermal conductivity, (b) Electronic thermal conductivity, (c) Total thermal conductivity, (d) Figure of merit

4.4 SUMMARY AND CONCLUSION

Concludingly, we have presented $RFeO_3$ (R=Pr, Nd) perovskite for their various properties using GGA, mBJ, and mBJ+U potential. These materials have shown half-metallic behavior in mBJ+U potential. The result of formation energies shows both perovskites can be manufactured under ambient conditions. The thermoelectric efficiency of PFO is found to increase with temperature with a maximum value reach to 0.38 at 1200 K. Therefore, PFO and NFO both materials have shown low value of thermoelectric efficiency. But these materials can be used as a source for spintronic applications due to their half-metallic characteristics.

REFERENCES

1. Mizokawa, T., and Fujimori, A. "Spin, charge, and orbital ordering in Mn perovskite oxides studied by model Hartree-Fock calculations." *Physical Review B* 56, no. 2 (1997): R493.
2. Ahn, K. H., Wu, X.W., Liu, K. and Chien, C.L. "Magnetic properties and colossal magnetoresistance of La (Ca) Mn O_3 materials doped with Fe." *Physical Review B* 54, no. 21 (1996): 15299.
3. Mochizuki, M., and Imada, M. "G-type antiferromagnetism and orbital ordering due to the crystal field from the rare-earth ions induced by the $GdFeO_3$-type distortion in $RTiO_3$ where R= La, Pr, Nd and Sm." *Journal of the Physical Society of Japan* 73, no. 7 (2004): 1833-1850.
4. Shang, M., Zhang, C., Zhang, T., Yuan, L., Ge, L., Yuan, H., and Feng, S. "The multiferroic perovskite $YFeO_3$." *Applied Physics Letters* 102, no. 6 (2013): 062903.
5. Singh, A., Choudhary, I., Mehta, S., Dahiya, S., Walia, C.S., Raina, K.K., and Chatterjee, R. "Optimal multiferroic properties and enhanced magnetoelectric coupling in $SmFeO_3$–$PbTiO_3$ solid solutions." *Journal of Applied Physics* 107, no. 8 (2010): 084106.
6. Song, Y.Q., Zhou, W.P., Fang, Y., Yang, Y.T., Wang, L.Y., Wang, D.H. and Du, Y.W. "Multiferroic properties in terbium orthoferrite." *Chinese Physics B* 23, no. 7 (2014): 077505.
7. Toàn, N.N., Saukko, S. and Lantto, V. "Gas sensing with semiconducting perovskite oxide $LaFeO_3$." *Physica B: Condensed Matter* 327, no. 2-4 (2003): 279-282.
8. Minh, N.Q. "Ceramic fuel cells." *Journal of the American Ceramic Society* 76, no. 3 (1993): 563-588.
9. Scott, J. F. "Multiferroic memories." *Nature Materials* 6, no. 4 (2007): 256-257.
10. Cao, S., Zhao, H., Kang, B., Zhang, J. and Ren, W. "Temperature induced spin switching in $SmFeO_3$ single crystal." *Scientific Reports* 4, no. 1 (2014): 1-5.
11. Chmaissem, O., Dabrowski, B., Kolesnik, S., Mais, J., Brown, D.E., Kruk, R., Prior, P., Pyles, B. and Jorgensen, J.D. "Relationship between structural

parameters and the Néel temperature in $Sr_{1-x}Ca_xMnO_3$ (0<~ x<~ 1) and $Sr_{1-y}Ba_yMnO_3$ (y<~ 0. 2)." *Physical Review B* 64, no. 13 (2001): 134412.

12. Maris, G., Volotchaev, V., and Palstra, T.T.M. "Effect of ionic size on the orbital ordering transition in RMnO3+ δ." *New Journal of Physics* 6, no. 1 (2004): 153.
13. Liu, Q., Li, B., Liu, J., Li, H., Liu, Z., Dai, K., Zhu, G., Zhang, P., Chen, F. and Dai, J. "Structure and band gap tuning of transparent $(Ba_{1-x}Sr_x)$ SnO_3 thin films epitaxially grown on MgO substrates." *EPL (Europhysics Letters)* 98, no. 4 (2012): 47010.
14. Ho, T.G., Ha, T.D., Pham, Q.N., Giang, H.T., Thu Do, T.A. and Nguyen, N.T. "Nanosized perovskite oxide $NdFeO_3$ as material for a carbon-monoxide catalytic gas sensor" *Advances in Natural Sciences: Nanoscience and Nanotechnology* 2 (2011): 015012.
15. Wang, Y., Yan, X., Chen, J., Deng, J., Yu, R. and Xing, X. "Shape controllable synthesis of $NdFeO_3$ micro single crystals by a hydrothermal route" *Cryst Eng Comm* 16 (2014): 858–862.
16. Mir, S.A., Ikram, M. and Asokan, K. "Effect of Ni doping on optical, electrical and magnetic properties of Nd orthoferrite." *In Journal of Physics: Conference Series* 534, no. 1, p. 012017. IOP Publishing, 2014.
17. Sultan, K., Ikram, M. and Asokan, K. "Structural, optical and dielectric study of Mn doped $PrFeO_3$ ceramics." *Vacuum* 99 (2014): 251-258.
18. Opuchovic, O., Kreiza, G., Senvaitiene, J., Kazlauskas, K., Beganskiene, A. and Kareiva, A. "Sol-gel synthesis, characterization and application of selected sub-microsized lanthanide (Ce, Pr, Nd, Tb) ferrites." *Dyes and Pigments* 118 (2015): 176-182.
19. Luxová, J., Šulcová, P. and Trojan, M. "Influence of firing temperature on the color properties of orthoferrite $PrFeO_3$." *Thermochimica Acta* 579 (2014): 80-85.
20. Zhou, Z., Guo, L., Yang, H., Liu, Q. and Ye, F. "Hydrothermal synthesis and magnetic properties of multiferroic rare-earth orthoferrites." *Journal of alloys and compounds* 583 (2014): 21-31.
21. Mir, F.A., Sharma, S.K. and Kumar, R. "Magnetizations and magneto-transport properties of Ni-doped $PrFeO_3$ thin films." *Chinese Physics B* 23, no. 4 (2014): 048101.

22. Cheon, C.I., Kim, J.S. and Jang, P.W. "Ferroelectric and Magnetic Properties of $PrFeO_3$–$PbTiO_3$ and $PrFeO_3$–$BiFeO_3$–$PbTiO_3$ Thin Films." Japanese journal of applied physics 41, no. 11S (2002): 6777.
23. Tijare, S.N., Bakardjieva, S., Subrt, J., Joshi, M.V., Rayalu, S.S., Hishita, S. and Labhsetwar, N. "Synthesis and visible light photocatalytic activity of nanocrystalline $PrFeO_3$ perovskite for hydrogen generation in ethanol–water system." *Journal of Chemical Sciences* 126, no. 2 (2014): 517-525.
24. Tang, P., Xie, X., Chen, H., Lv, C. and Ding, Y. "Synthesis of Nanoparticulate $PrFeO_3$ by Sol–Gel Method and its Visible-Light Photocatalytic Activity." *Ferroelectrics* 546, no. 1 (2019): 181-187.
25. Megarajan, S.K., Rayalu, S., Nishibori, M. and Labhsetwar, N. "Improved catalytic activity of $PrMO_3$(M= Co and Fe) perovskites: synthesis of thermally stable nanoparticles by a novel hydrothermal method." *New Journal of Chemistry* 39, no. 3 (2015): 2342-2348.
26. De Groot, C.H., Buschow, K.H.J. and De Boer, F.R. "Magnetic properties of $R_2Co_{17-x}Al_x$ compounds (R= Ho, Dy, Y)." *Physica B: Condensed Matter* 229, no. 3 (1997):213-6.
27. De Groot, R.A., Mueller, F.M., van Engen, P.V. and Buschow, K.H.J. "New class of materials: half- metallic ferromagnets." *Physical Review Letters* 50, no. 25 (1983):2024
28. Ghimire, M.P., Thapa, R.K., Rai, D.P., Sinha, T.P., Hu, X. "Half metallic ferromagnetism in trilayered perovskites $Sr_4T_3O_{10}$ (T= Co, Rh)." *Journal of Applied Physics* 117, no. 6 (1983):063903.
29. Malsawmtluanga, T., Vanlalruata, B. and Thapa, R.K. "Investigation of half-metallicity of GeKMg and SnKMg by Using mBJ potential method." *In Journal of Physics: Conference Series*, vol. 765, no. 1, p. 012018. IOP Publishing, 2016.
30. Wu, C., Zheng, W., Si, N., Feng, W.J., Zhang, F.G. and Jiang, W. "The structural, half-metal, magnetic, and mechanical properties of full Heusler alloy CrCoVSb: a first-principles study." *Chinese Journal of Physics* 66 (2020): 436-443.

31. Jaiganesh, G., Eithiraj, R.D. and Kalpana, G. "Theoretical study of electronic, magnetic and structural properties of Mo and W based group V (N, P, As, Sb and Bi) compounds." *Computational Materials Science* 49, no. 1 (2010): 112-120.
32. Akai H. “Ferromagnetism and its stability in the diluted magnetic semiconductor (In, Mn) As.” *Physical Review Letters* 81, no. 14 (1998):3002.
33. Al-zyadi, J.M., Gao, G.Y., Yao, K.L. “First-principles study on the (111) surface of half-metallic rocksalt VPo.” *Solid State Communications* 152, no. 14 (2012):1244-8.
34. Ogawa, T., Shirai, M., Suzuki, N., Kitagawa, I. “First -principles calculations of electronic structures of diluted magnetic semiconductors (Ga, Mn) As.” *Journal of Magnetism and Magnetic materials* 196 (1999):428 -9.
35. Fong, C.Y., Qian, M.C., Pask, J.E., Yang, L.H., and Dag, S. "Electronic and magnetic properties of zinc blende half-metal superlattices." *Applied Physics Letters* 84, no. 2 (2004): 239-241.
36. Perdew, J.P., Ruzsinszky, A., Csonka, G.I., Vydrov, O.A., Scuseria, G.E., Constantin, L.A., Zhou, X., and Burke, K. “Restoring the density-gradient expansion for exchange in solids and surfaces” *Phys. Rev. Lett*. 100 (2008): 136406.
37. Maqsood, S., Rashid, M., Din, F.U., Saddique, M.B. and Laref, A. "Theoretical Investigation of Half-Metallic Oxides $XFeO_3$ (X= Sr, Ba) via Modified Becke–Johnson Potential Scheme." *Journal of Electronic Materials* 47, no. 3 (2018): 2032-2041.
38. Hohenberg, P., Kohn, W. “Inhomogeneous electron gas.” *Phys Rev.* 136, no. 3B (1964): B864-B871
39. Blaha, P., Schwarz, K., Madsen, G.K.H., Kvasnicka, D., Luitz, J. “wien2k.” An augmented plane wave+ local orbitals program for calculating crystal properties” (2001) p. 60.
40. Perdew, J.P., Burke, K., Ernzerhof, M. “Generalized gradient approximation made simple.” *Phys Rev Lett*. 77, no. 18 (1996): 3865- 3868.
41. Tran, F., Blaha, P. “Accurate band gaps of semiconductors and insulators with a semilocal exchange-correlation potential.” *Phys Rev Lett.* 102 (2009):226401.

42. Anisimov, V.I., Solovyev, I.V., Korotin, M.A., Czyżyk, M.T. and Sawatzky, G.A. "Density-functional theory and NiO photoemission spectra." *Physical Review* B 48, no. 23 (1993): 16929.
43. Monkhorst, H.J. and Pack, J.D. "Special points for Brillouin-zone integrations." *Physical review B* 13, no. 12 (1976): 5188.
44. Babu, K.E., Kumar, V.V., Kumari, K.B., Neeraja, K., Praveena, N.G. and Veeraiah, V. "Electronic structure and magnetic properties of cubic perovskite $PrFeO_3$ and NdFeO3: a first-principles study." *In AIP Conference Proceedings*, vol. 1992, no. 1, p. 040036. AIP Publishing LLC, 2018.
45. Jiang, L. Q., Guo, J. K., Liu, H. B., Zhu, M., Zhou, X., Wu, P., & Li, C. H. (2006). Prediction of lattice constant in cubic perovskites. Journal of Physics and Chemistry of Solids, 67(7), 1531–1536.
46. Rocher, G.S. "Structure and Bonding in Crystalline Materials" *Cambridge University Press, Cambridge, UK* (2001): p. 174.
47. Birch, F. "The effect of pressure upon the elastic parameters of isotropic solids, according to Murnaghan's theory of finite strain." *Journal of Applied Physics* 9, no. 4 (1938): 279-288.
48. Huang, Z.W., Zhao, Y.H., Hou, H., Han, P.D. "Electronic structural, elastic properties and thermodynamics of $Mg_{17}Al_{12}$, Mg_2Si and Al_2Y phases from first-principles calculations." *Phys B Condens Matter* 407, no. 7 (2012): 1075-1081.
49. Han, W-D., Li, K., Hu, F., Li, X-D., Dai, J. "First-principle investigation of the structural, electronic, elastic, and elastic anisotropy properties and thermal stabilities of $CeMg_2Si_2$ and Mg_2Si." *Mater Res Express* 6, no. 11 (2019):1165f8.
50. Yakoubi, A., Baraka, O., Bouhafs, B. "Structural and electronic properties of the laves phase based on rare earth type BaM_2 (M= Rh, Pd, Pt)." *Res Phys.* 2 (2012): 58-65.
51. Goodenogh, J.B. "Electronic and ionic transport properties and other physical aspects of perovskites." *Reports on Progress in Physics* 67, no. 11 (2004): 1915.
52. Maqsood, S., Rashid, M., Din, F.U., Saddique, M.B. and Laref, A. "Theoretical Investigation of Half-Metallic Oxides $XFeO_3$ (X= Sr, Ba) via Modified Becke–Johnson Potential Scheme." *Journal of Electronic Materials* 47, no. 3 (2018): 2032-2041.

53. Srivastava, V., Kaur, N., Wang, X., Mushtaq, M., and Dar, S.A. "First-principles study on structural, electronic, magnetic, elastic, mechanical and thermodynamic properties of Mn_2PtCo Heusler alloy." *International Journal of Energy Research* 45, no. 7 (2021): 11305-11319.
54. Ali, Z., Ahmad, I. and Reshak, A.H. "GGA+ U studies of the cubic perovskites $BaMO_3$ (M= Pr, Th and U)." *Physica B: Condensed Matter* 410 (2013): 217-221.
55. Yan, P.L., Zhang, J.M., Zhou, B. and Xu, K.W. "The structural, electronic, magnetic and mechanical properties of quaternary Heusler alloys ZrTiCrZ (Z= Al, Ga, In, Si, Ge, Sn): a first-principles study." *Journal of Physics D: Applied Physics* 49, no. 25 (2016): 255002.
56. Blanco, M.A., Francisco, E. and Luana, V., 2004. "GIBBS: isothermal-isobaric thermodynamics of solids from energy curves using a quasi-harmonic Debye model." *Computer Physics Communications* 158, no. 1 (2004): 57-72.
57. Otero-de-la-Roza, A., Abbasi-Pérez, D. and Luaña, V. "Gibbs2: A new version of the quasiharmonic model code. II. Models for solid-state thermodynamics, features and implementation." *Computer Physics Communications* 182, no. 10 (2011): 2232-2248.
58. Otero-de-la-Roza, Alberto, and Luaña, V. "Gibbs2: A new version of the quasi-harmonic model code. I. Robust treatment of the static data." *Computer Physics Communications* 182, no. 8 (2011): 1708-1720.
59. Petit, A.T., Dulong, P.L. “Study on the measurement of specific heat of solids.” *Ann Chim Phys* 10 (1819): 395.
60. Allen P. “Boltzmann theory and resistivity of metals. Quantum Theory of Real Materials” 1st edn. London, US: Kluwer Academic Publishers 348 (1996):219-250.
61. Ziman, J.M. “Electrons and phonons: the theory of transport phenomena in solids.” *New york, USA: Oxford University Press* (2001).
62. Hurd, C. “The hall effect in metals and alloys.” *The International Cryogenics Monograph Series* 1. Boston, MA: Springer (1972).
63. Madsen, G.K.H., Singh, D.J. “BoltzTraP. A code for calculating band-structure dependent quantities.” *Comput Phys Commun.* 175, no. 1 (2006):67-71.

64. Morelli, D.T., Slack, G.A. “High lattice thermal conductivity solids. High Thermal Conductivity Materials.” *New York: Springer* (2006):37-68.
65. Julian, C.L. “Theory of heat conduction in rare-gas crystals.” *Phys Rev* 137, no. 1A (1965): A128.
66. Leibfried, G., and Schl¨omann, E. Nachr. Akad. Wiss. G¨ottingen II a(4), 71 (1954).

CHAPTER 5

STRUCTURAL, ELECTRONIC, ELASTIC, MECHANICAL, THERMODYNAMIC, AND THERMOELECTRIC PROPERTIES OF $RbSnX_3$ (X =F, Cl, Br, I)

5.1 INTRODUCTION

The over-exploitation of resources and imperfect knowledge have limited the fuel accessible for energy resources. The need of the hour is to change the basis of energy resources from fossil to renewable. Some of the energy sources that lead to recreation are photovoltaics, thermoelectric, biomass, solar cells, etc. [1-4]. The study of materials offers a fresh way to access the necessary energy sources. Perovskites can be employed for these types of energy applications [5, 6]. Perovskite compounds have exhibited amazing properties, including optoelectronic, thermoelectric, colossal magnetoresistance, [7-13], etc., which can lead to further developments in industry, aerodynamics, and technical areas [14-20]. These compounds have promising optoelectronic properties. These materials' thermoelectric (TE) capabilities are also intriguing because they can be employed as energy sources. These properties contribute to the development of TE materials which further contribute to the formation of thermoelectric power generators. The first reported TE material with an efficiency of more than 1 was PbTe [21]. However, Pb-based compounds are more toxic and less stable. As a result, in the search for more efficient TE materials, alternate materials must be considered, and leadless halide perovskites are suitable for meeting the requirements. Here, we provide a brief literature survey of these materials. Xin Mao et al. [22] have worked on the bandgaps of 260 inorganic halide perovskites. Gou et al. [23] have examined the photovoltaic properties of $CsSnI_3$. $Rb_xCs_{1-x}SnI_3$ perovskite examined by Jung et.al [24] for Rb/Cs effect on structural, electronic, and thermodynamic performances Yunsheng et al. [25] have introduced the strain's effects on tuning the bandgap of $RbSnCl_3$ along with structural, electronic, and optical examinations. The $RbyCs_{1-y}Sn\ (Br_xI_{1-x})_3$ perovskite compounds were considered a hopeful contender for solar photovoltaic applications as reported by

Jiang et al. [26]. Rai et al. have worked on the optical and electronic behavior of $RbMF_3$ [27]. Khan et al. have also worked on similar properties of $ASnF_3$ [28] and $RbSnX_3$ (X= Br, Cl) [29] compounds. The current work presents a thorough image of the $RbSnX_3$ (X=F, Cl, Br and I) perovskites. They have been previously investigated for electronic, structural, and optical properties [22-35]. We have therefore expanded our research on them by providing novel details about their elastic, mechanical, thermophysical and thermoelectric parameters for their applications in the respective areas. The present research work is sectioned into different parts. Section 5.1 provides an introduction and status of the work on halide perovskites, and Section 5.2 provides the computational methodologies used in calculations of total energy and its associated properties. Section 5.3 deals with the potential results through a discussion. Section 5.4 presents the concluding remarks of the present study.

5.2 COMPUTATIONAL DETAILS

The rubidium tin-based halide perovskites, $RbSnX_3$ (X=F, Cl, Br and I), crystallize in cubic phase Pm-3m (221). Their physical properties are assessed by applying quantum mechanics to density functional theory [36]. DFT solves many bodies interacting electron and nuclei system by reducing it to Kohn Sham one electron equation. To discover the most stable ground state of the compounds, different exchange-correlation potentials such as Perdew et al. (PBE) [37], WC (Wu and R. E. Cohen) [38], and PBE-sol (PBE functional revised for solids) [39] is used to optimize the crystal structures. Total energies are fitted using the Birch Murnaghan equation [40]. For understanding the electronic performances, halide perovskites are treated under Tran and Blaha modified Becke Johnson (TB-mBJ) [41] and GGA (PBE, WC, PBE sol) potentials. The quantum mechanical computational treatment with appropriate choices of basis set via FP-LAPW, as applied in WIEN2K coding [42] is given for solving the schrödinger equation of the current problem. FPLAPW technique divides unit cell crystals into interstitial and atomic regions. These two regions work in different coordinate systems i.e., interstitial use plane wave and atomic uses spherical harmonics. The self-consistent field (SCF) calculations are accomplished with convergence criteria i.e., $R_{MT}\ X\ K_{MAX}$, L_{max}, and G_{max} are set to be equivalent to 7, 10, and 12 $(a.u)^{-1}$, respectively, where R_{MT} represents the radius of

smallest atom, K_{MAX}, highest size propagation vector, and L_{max}, highest value of angular momentum and G_{max}, Fourier charge density inside the atomic sphere. The energy bands and total density of states are investigated via tetrahedron method [43] with a mesh of 10 x 10 x 10 *K* points for the integration of the first Brillouin zone. The charge and energy convergences are considered to be 10^{-3} a.u^3 and 10^{-3} Ry to prevent core charge leakage.

Further, elastic constants for the cubical crystals are evaluated from the cubic-elastic package by Morteza Jamal [44] along with its interference with WIEN2K [42]. The Quasi-harmonic model, as implemented in Gibbs2 programming, is used to calculate the thermodynamic performances of halide perovskites [45–47]. The semiclassical Boltzmann transport phenomena [48-50], which is used in the BoltzTrap code [51, 52], is also used to report thermoelectric properties.

5.3 RESULTS AND DISCUSSION

5.3.1 Structural Properties

The $RbSnX_3$ (X=F, Cl, Br, and I) (RSX) perovskites stabilize in space group 221 (Pm-3m) with lattice constants [53, 54] reported in *Table 5.1*. The Rb atoms are positioned at the corner (0, 0, 0), Sn at the center (½, ½, ½) while X atoms are positioned at the face center (½, ½, 0), (0, ½, ½), and (½, 0, ½) of the lattice. Figure 5.1 represent the arrangement of atoms within the crystal structure of $RbSnX_3$ (X= F, Cl, Br, and I). The values of lattice parameters have also been predicted analytically [55, 56]. Lattice parameter obtained analytically and through DFT shows similitude behavior. The obtained values of lattice parameter, volume, bulk pressure, pressure derivative, and ground state, formation, and cohesive energies are presented in *Table 5.1.* As we can see in *Table*, minimum energy for RSX perovskite is corresponding to PBE-GGA i.e., -18920.979129 Ry ($RbSnF_3$), -21090.640532 Ry ($RbnCl_3$), and -33961.419432 Ry ($RbSnBr_3$), and -61035.93155Ry ($RbSnI_3$). Therefore, we concluded that all three compounds are stable in PBE-GGA. As we move from F to I, we found that volume and lattice parameters increase while bulk decreases. The stability of the material and energy feasibility is assured by calculating the formation energy.

The calculated formation energies of $RbSnF_3$, $RbSnCl_3$, and $RbSnBr_3$ fulfil the criterion $E_{form} < 0.2eV/atom$ [57, 58], which ensures the feasibility and ascertaining of the formation of these materials. Their negative values ensure thermodynamical stability and their possibility of experimental synthesis. Cohesive energy measures the energy required to isolate atoms present in the compound. The cohesive energies for $RbSnF_3$, $RbSnCl_3$, $RbSnBr_3$, and $RbSnI_3$ are obtained. The least unstable of the three compounds is $RbSnF_3$.

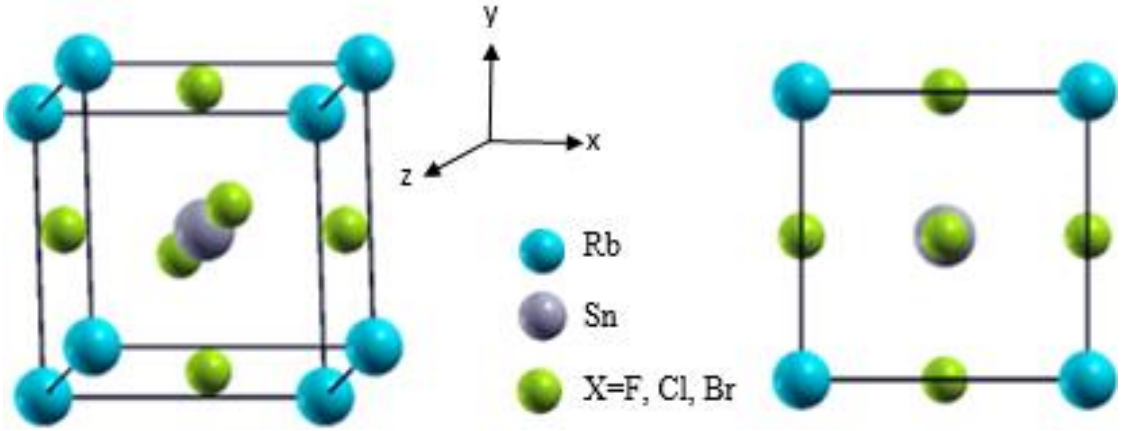

Figure 5.1: Crystal structure of $RbSnX_3$

5.3.2 Electronic Properties

Further, we have determined the band gaps for Rb-Sn halide perovskites using band structure diagrams as depicted in *Figure 5.2*. Considering various potentials, $RbSnX_3$ (X=F, Cl, Br, and I) compounds demonstrate semiconducting nature, as shown in Figure. These structures exhibit the semiconducting nature of direct bandgap. The maximum value of bandgap for $RbSnF_3$, $RbSnCl_3$, $RbSnI_3$ are obtained in case of mBJ and their values are 3.65, 1.5 eV, 0.65 eV, respectively while for $RbSnBr_3$, maximum bandgap observed in PBE-GGA. It means mBJ overestimates the value of bandgap for $RbSnF_3$, $RbSnCl_3$, $RbSnI_3$ while underestimating $RbSnBr_3$. Looking at simply the mBJ example, we discovered that the value of band gaps decreases on switching from F to I. Finally, *Table 5.2* shows the band gap values for various exchange potentials and compares them to the data from the other's an experiment and theoretical work.

Table 5.1: Lattice parameters *a* (Å), Volume *V* (a.u^3), Bulk modulus *B* (GPa), Pressure derivative *B'*, Minimum energy E_0 (Ry), Formation energy E_{form} (eV/atom), and Cohesive energy E_{coh} (eV/atom) for $RbSnF_3$, $RbSnCl_3$, $RbSnBr_3$, $RbSnI_3$

Compound	**XC GGA**	**Lattice parameter (Å)**			**V (a.u^3)**	**B (GPa)**	**B'**	**E_0 (Ry)**	**E_{form} (eV/atom)**	**E_{coh} (eV/atom)**
		Optimized	**Others**	**Analytical**						
$RbSnF_3$	PBE	4.765	-	4.703	730.180	43.528	4.765	-18920.979129	-2.48	3.66
	WC	4.703			702.063	47.454	4.747	-18917.453675		
	PBE-sol	4.693			698.981	48.731	4.734	-18909.936595		
$RbSnCl_3$	PBE	5.607	5.596 [53]	5.558	1190.037	24.810	3.215	-21090.640532	-1.45	2.76
	WC	5.512			1130.415	25.405	3.619	-21086.418126		
	PBE-sol	5.499			1122.589	25.965	4.616	-21077.338911		
$RbSnBr_3$	PBE	5.869	5.863 [53]	5.826	1364.647	19.315	4.962	-33961.419432	-1.16	3.19
	WC	5.760			1289.641	22.198	5.263	-33955.728075		
	PBE-sol	5.747			1281.541	22.727	5.279	-33941.938841		
$RbSnI_3$	PBE	6.264	6.25 [54]	6.254	1652.626	15.205	4.405	-61035.931550	-0.93	1.62
	WC	6.127			1552.329	17.410	4.804	-61028.657480		
	PBE-sol	6.112			1541.270	17.269	4.435	-61008.957220		

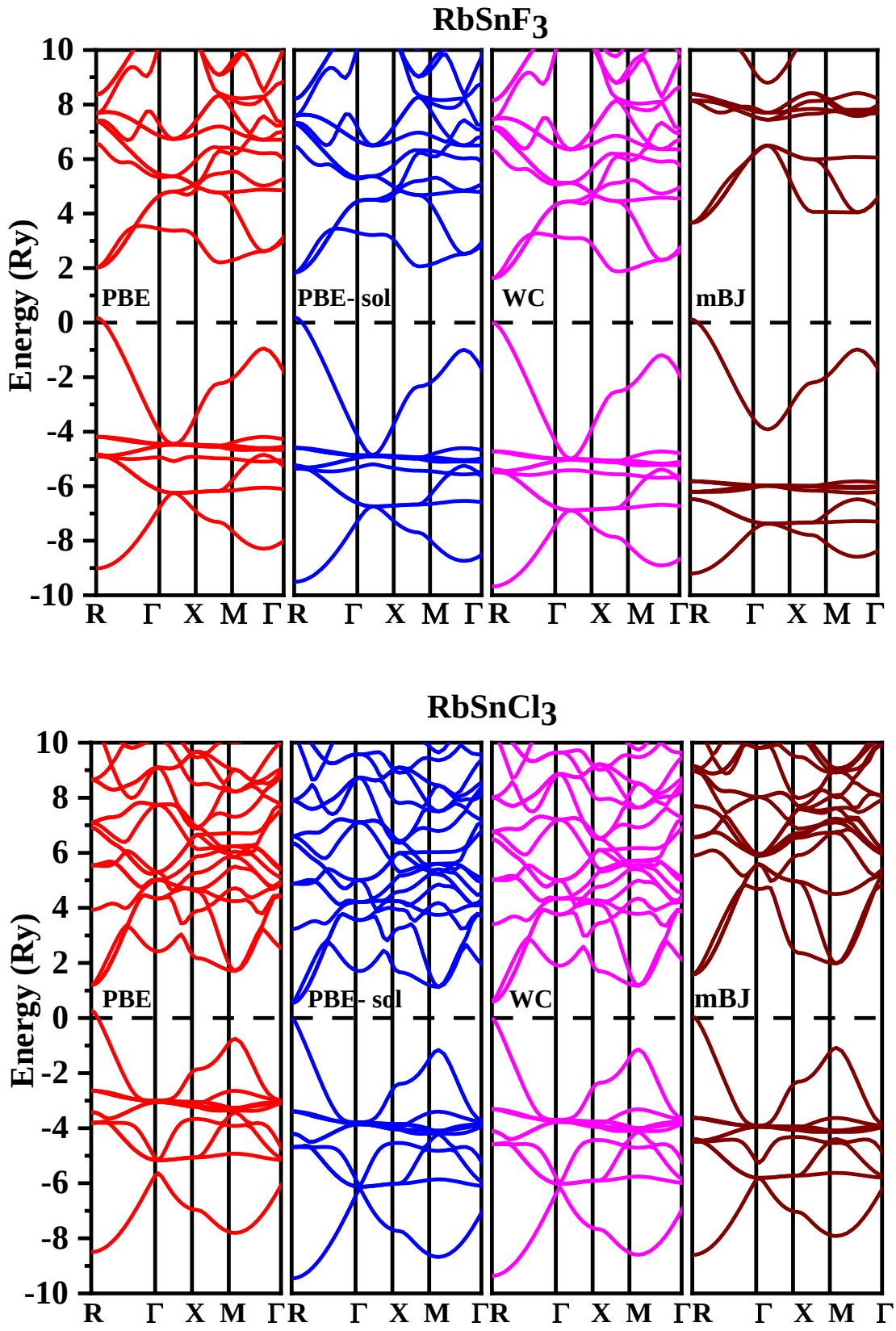

Figure 5.2(a): Band Structure plot for $RbSnX_3$ (X= F, Cl, Br, and I)

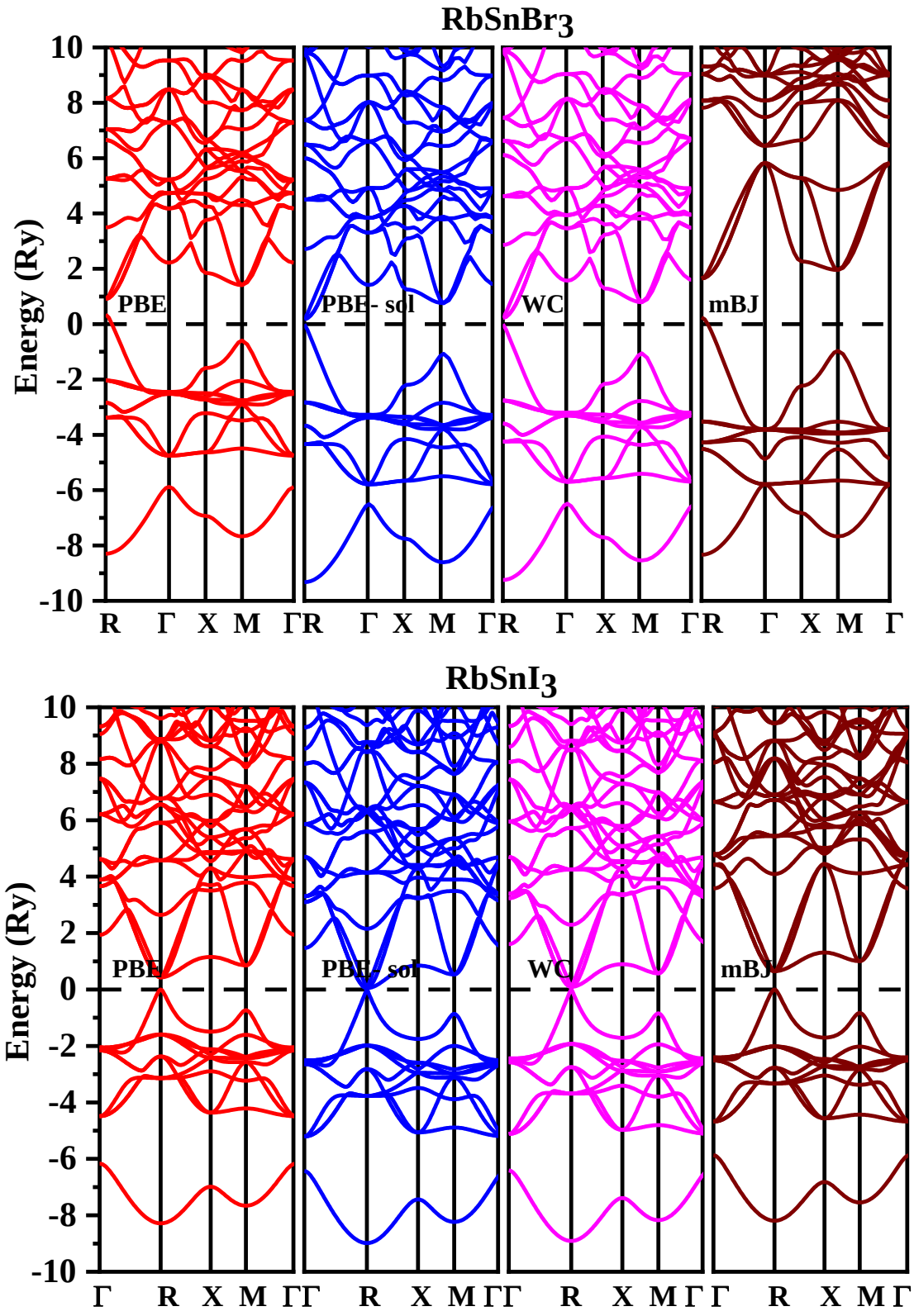

Figure 5.2(b): Band Structure plot for $RbSnX_3$ (X= F, Cl, Br, and I)

Table 5.2: Band gap (in eV) using exchange-correlations XC: PBE, WC, PBE-sol and mBJ for $RbSnX_3$ (X=F, Cl, Br, and I)

Compound	**XC**	**Bandgap (eV)**	**Other works/ Exp (eV)**
$RbSnF_3$	PBE	2.102	
	WC	1.622	-
	PBE-sol	1.926	
	mBJ	3.65	
$RbSnCl_3$	PBE	1.062	1.43 [22], 1.61 [60], 0.94 [53]
	WC	0.596	
	PBE-sol	0.543	
	mBJ	1.532	
$RbSnBr_3$	PBE	1.047	0.57 [59], 1.10 [60], 0.59 [53]
	WC	0.226	
	PBE-sol	0.182	
	mBJ	1.025	
$RbSnI_3$	PBE	0.432	0.38, 1.39 [56], 0.383[54]
	WC	0.097	
	PBE-sol	0.052	
	mBJ	0.649	

5.3.3 Elastic and Mechanical Properties

The determination of elastic parameters plays a vital role in material's ability to deform on the application of the force. These elastic constants are also useful in determining mechanical properties. It also provides information on the behavior of bonding forces, as well as the materials' ductility or brittleness. The effects of the external forces on these materials are measured from the elastic constants. The obtained value of elastic constants (C_{ij}) from the present calculations for $RbSnF_3$, $RbSnCl_3$, $RbSnBr_3$, and $RbSnI_3$ are tabulated in *Table 5.3*.

The elastic parameters are required for evaluation of materials' mechanical properties. These materials fulfill the required mechanical stability of a cubical system. The required mechanical stability norms [61, 62] for a cubical structure $RbSnX_3$ are larger than the succeeding limits of the elastic constants. All considered compounds fulfill the criteria of mechanical stability.

Further, some mechanical parameters, bulk modulus *B*, shear modulus *G*, and young's modulus *Y* can be evaluated from these elastic constants. Their relations with the elastic constants [63-67] are shown in chapter 2 *equations (2.92)-(2.102)*. The stiffness of the material is described by the shear modulus. *B* relates to how much the material is resistive to the change in the volume. The next elastic modulus, i.e., Young's modulus *Y*, depends on bulk *B* as well as on the shear *G* modulus. It describes the elongation and compression of the material. The values of *B*, *G*, and *Y* for $RbSnF_3$, $RbSnCl_3$, $RbSnBr_3$, and $RbSnI_3$ are given in *Table 5.3*. We can interpret from *Table 5.3* that $RbSnF_3$ has the highest value of *B*, *G*, and *Y*, among all of them.

Other mechanical parameters like Poison ratio, Pugh ratio, anisotropy, Cauchy's pressure and thermodynamic parameters are calculated and offered in *Table 5.3*.

The Poison Ratio defines the behavior of bonding forces between atoms. The value of the Poison ratio should be in the range of 0.25-0.50 [68]. Its value is 0.1 for covalent, 0.25 for metallic and 0.33 for ionic bonding [69,70]. $RbSnCl_3$, $RbSnBr_3$, and $RbSnI_3$ show mix nature of metallic and ionic bonding while $RbSnF_3$ shows ionic bonding and $RbSnI_3$ shows more of metallic nature. Calculated values of Poison ratios are 0.360, 0.296, 0.290 and 0.27 for $RbSnF_3$, $RbSnCl_3$, $RbSnBr_3$, and $RbSnI_3$, respectively.

Cauchy pressure (C_{12}-C_{44}) describes material's ductility and brittleness. Its positive values indicate ductile behavior, while negative values signify brittleness. Pugh's ratio (*B/G*) likewise describes ductile and brittle behavior. This defines the ranges of plasticity of the crystals. According to Pugh [71], if $B/G > 1.75$, it shows ductility; otherwise, it is brittle. After examining, the calculated values of Cauchy pressure and *B/G* ratio in *Table 5.3,*Table 5.3 we concluded that RSX shows a positive value of Cauchy pressure and a $B/G > 1.75$ which means materials are ductile and can be easily deformed.

Elastic anisotropy (*A*) is a very significant parameter in engineering and the manufacturing area. It helps in determining the microcracks within the material. Its divergence from 1 represents anisotropy. The obtained value of *A*, shown in *Table 5.3*, for RSX is less than unity and thus anisotropic.

The thermal behavior of the compound can also be understood by considering elastic parameters. Xing Liu *et. al* [72] have proposed that θ_D can be computed using elastic

coefficients. It reflects the thermodynamic properties and their association with parameters like specific heat, longitudinal velocity, transverse velocity, and the thermal expansion coefficient of the solids. Another important parameter that can be evaluated from the elastic constants is melting temperature (T_M). Melting temperature is linked to the elastic constants [73] and its value for $RbSnX_3$ (X= F, Cl, Br, and I) are shown in *Table 5.3*. Their values decrease with an increase in the ionic radius of the 'X' element in the compound.

Table 5.3: Elastic constant C_{11}, C_{12} and C_{44} (GPa), Bulk modulus B (GPa), Shear modulus G (GPa), and Young's modulus Y (GPa), Poison ratio ν, Cauchy's pressure C_{12}-C_{44} (GPa), Pugh ratio B/G, Anisotropy A, Debye temperature θ_D (K) and Melting temperature T_M (K) for $RbSnX_3$ (X= F, Cl, Br, and I) perovskites

Parameters	**$RbSnF_3$**	**$RbSnCl_3$**	**$RbSnBr_3$**	**$RbSnI_3$**
C_{11}	90.25	47.51	46.20	33.63
C_{12}	21.78	8.66	7.34	5.99
C_{44}	6.65	6.38	6.06	5.58
B	44.60	21.61	20.29	15.20
G	13.75	10.16	9.89	8.10
Y	37.41	26.36	25.52	20.64
ν	0.36	0.29	0.29	0.27
C_{12}-C_{44}	15.13	2.28	1.27	0.41
B/G	3.24	2.13	2.05	1.88
A	0.19	0.32	0.31	0.40
θ_D	222.81	189.01	159.39	129.519
T_M	1086± 300	834± 300	826± 300	752± 300

5.3.4 Thermodynamic Properties

We have accomplished the thermodynamic performances of considered materials by means of Quasi-harmonic model [45-47]. Gibbs2 program, inbuilt within the WIEN2K code is incorporated for calculation of these parameters. Various thermodynamic parameters: heat capacity (C_V), volume (V), bulk modulus (B), Debye temperature (θ_D), Grüneisen constant (γ), entropy (S), and thermal expansion coefficient (α), have been calculated w.r.t temperature (T) and pressure (P) ranging

from 0–1200 K and 0–50 GPa, respectively for $RbSnF_3$, $RbSnCl_3$, $RbSnBr_3$, and $RbSnI_3$ halide perovskites. Gibbs2 program [44] uses the slater method [74], which was further explored by M.A Blanco for finding these thermodynamic quantities.

Heat capacity (C_V) plot with temperature is presented in *Figure 5.3(a-d)* for $RbSnF_3$, $RbSnCl_3$, $RbSnBr_3$, and $RbSnI_3$. The term "heat capacity" refers to the amount of energy needed to heat or cool a substance of a particular mass. It provides information about phase transitions and lattice vibrations. We interpret from the figure that at lower temperatures, C_V increases rapidly due to the dominance of an anharmonic effect following the T^3 law of the Debye model. Its behavior in the range of 300-800 K is sluggish. Further, high temperatures tend to suppress anharmonicity resulting in the attainment of the saturation limit i.e., Dulong-Petit limit [75]. This explains that thermal energy results in the excitation of phonon modes. Another way around, C_V variation is found to be decrease with pressure for all inspected values of temperatures. Heat capacity's behavior for $RbSnX_3$ perovskites is bestowed on the Debye model. Their values at 300 K and 0 GPa are calculated to be 72.6 ($RbSnF_3$), 73.6 ($RbSnCl_3$), 74.1 ($RbSnBr_3$) and 74.3 ($RbSnI_3$) J/mol K. The Dulong-Petit limits achieved for $RbSnX_3$ at 1200 K and 0 GPa are 74.7 ($RbSnF_3$), 74.8 ($RbSnCl_3$), 74.8 ($RbSnBr_3$), and 74.62 ($RbSnI_3$) J/mol K, respectively. Our provided data may help experimentalists to obtain data on the C_V.

The temperature and pressure variation on volume (V) of cubic structured $RbSnX_3$ compounds is shown in *Figure 5.4(a-d)*. Figures illustrate that volume increases indolently with temperature but it decreases tediously with pressure for $RbSnF_3$, $RbSnCl_3$, $RbSnBr_3$ and $RbSnI_3$ perovskites. As it is well-known that volume and pressure show inverse relations. The unit cell volume follows the general pattern of expansion and compression in solids on the application of temperature and pressure, respectively.

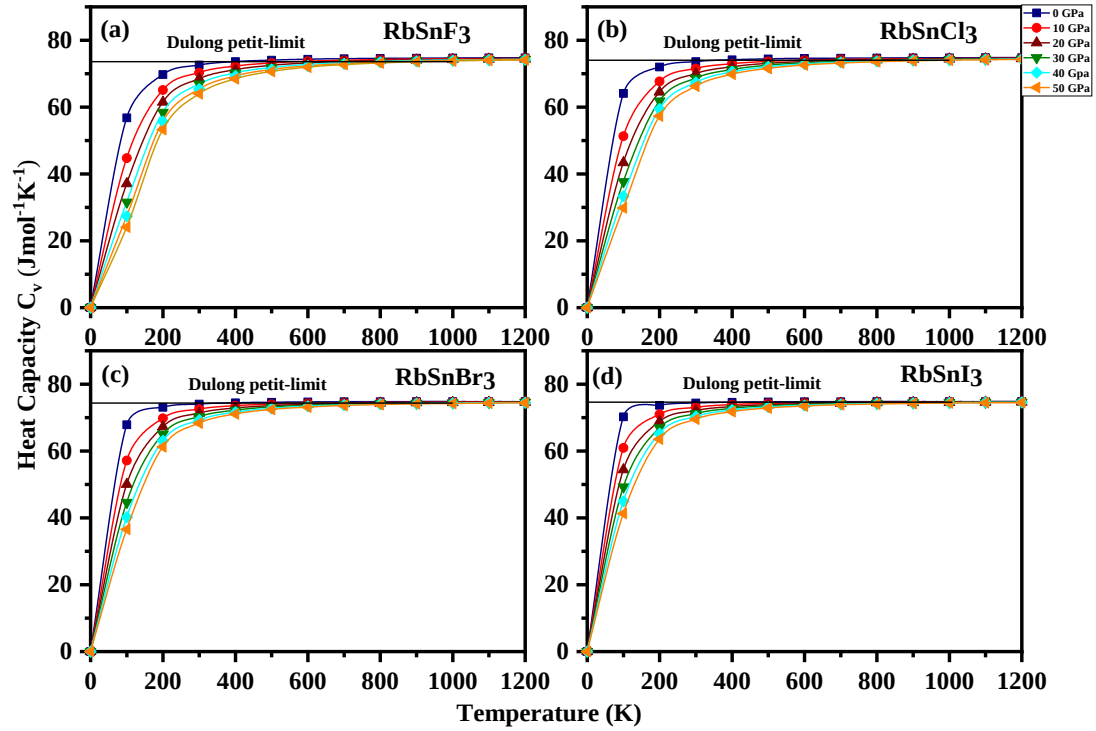

Figure 5.3: Heat Capacity plot versus temperature for the constant value of pressures for $RbSnX_3$ (X=F, Cl, Br, and I) perovskite

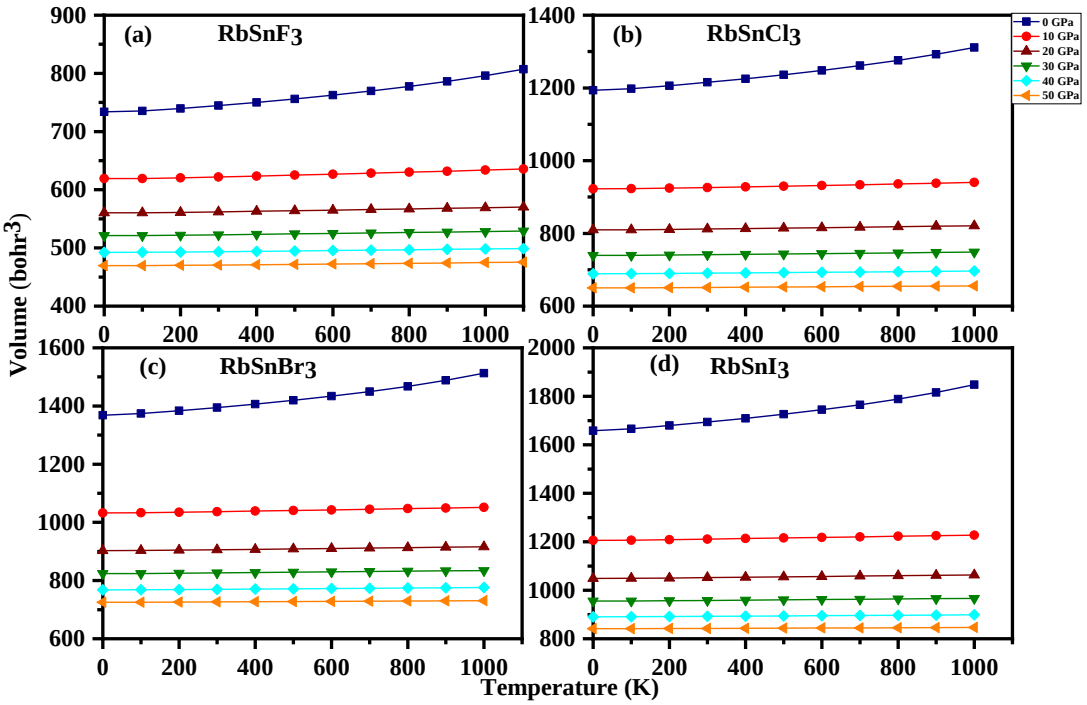

Figure 5.4: Volume plot versus temperature for the constant value of pressures for $RbSnX_3$ (X=F, Cl, Br, and I) perovskite

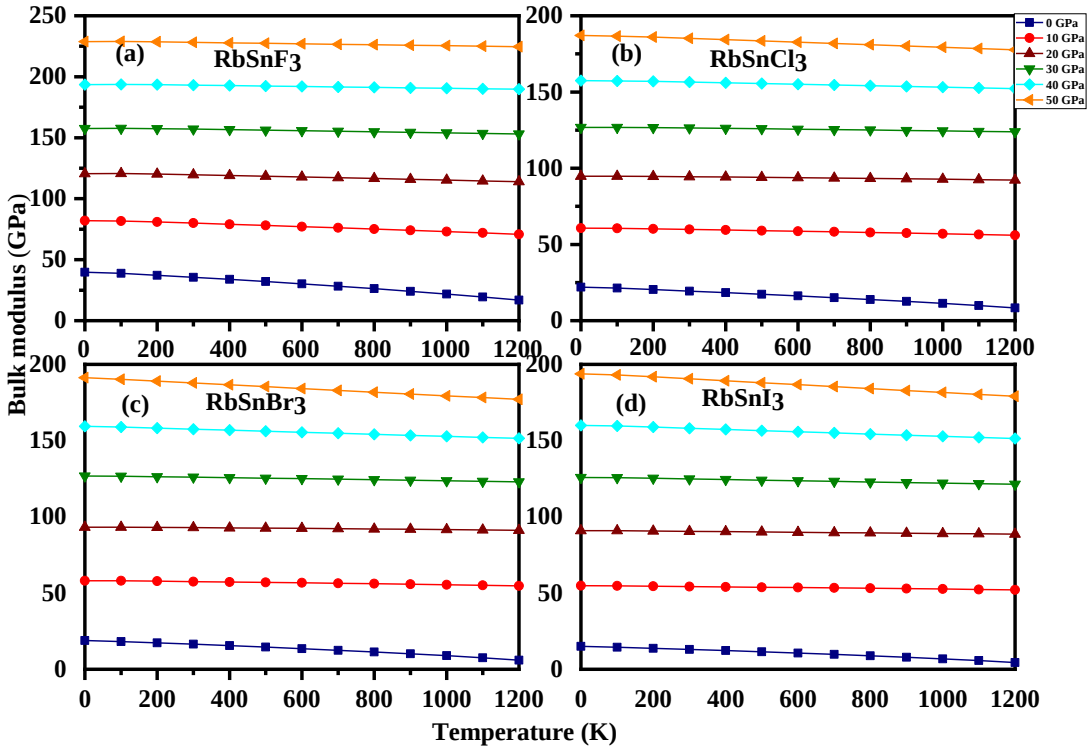

Figure 5.5: Bulk modulus plot versus temperature for the constant value of pressures for $RbSnX_3$ (X=F, Cl, Br, and I) perovskite

Figure 5.5(a-d) shows a variation in *B* w.r.t *T* (0-1200 K) at a constant value of pressure 0, 10, 20, 30, 40, 50 GPa. The bulk modulus gets increased with the increment of pressure while showing a decrement with the temperature for $RbSnF_3$ (*Figure 5.5a*), $RbSnCl_3$ (*Figure 5.5b*), $RbSnBr_3$ (*Figure 5.5c*) and $RbSnI_3$ (*Figure 5.5d*). The response of bulk modulus to *T* and *P* is inversed by the unit cell volume. As temperature increases hardness of the material also increases while pressure diminishes the same. Temperature decreases the interatomic distance of the atoms within the compound, which results in reducing the hardness. B_0 values are 35.6 ($RbSnF_3$), 19.4 ($RbSnCl_3$), 16.4 ($RbSnBr_3$) and 13.1 ($RbSnI_3$) GPa under ambient conditions. The bulk modulus shows an inverse relationship with the ionic radius of the halide atoms in the RSX perovskites.

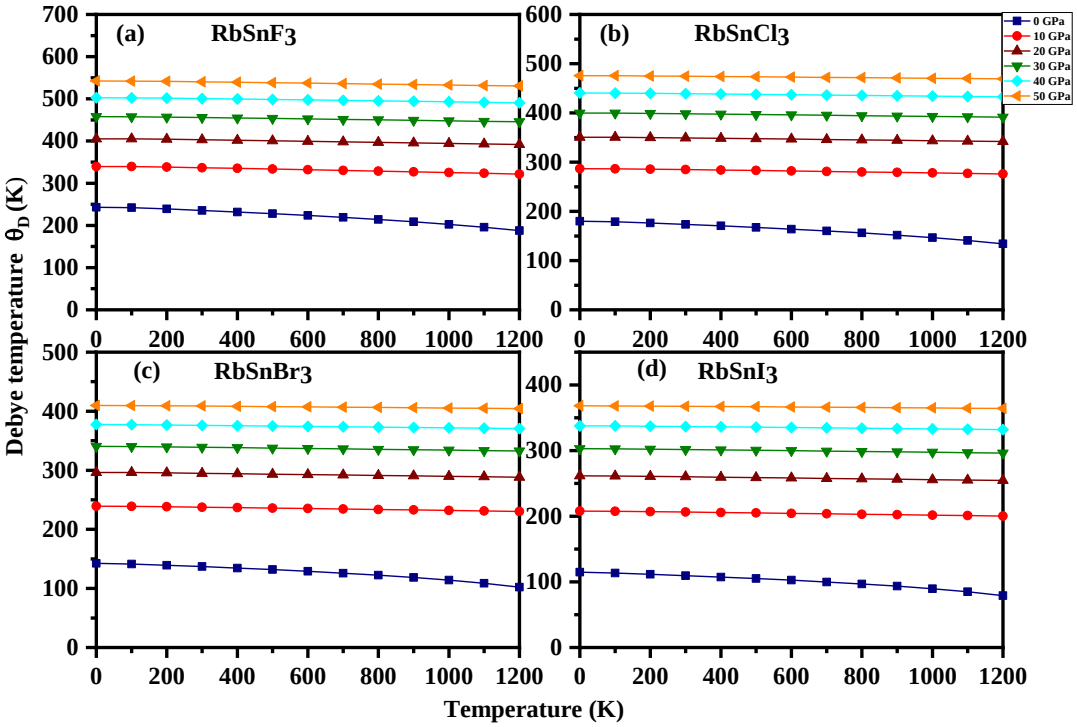

Figure 5.6: Debye temperature plot versus temperature for the constant value of pressures for $RbSnX_3$ (X=F, Cl, Br, and I) perovskite

Debye temperature θ_D an important thermodynamic parameter explicates quantities like C_v and α. It refers to the maximum temperature attained due to a single mode of vibration. It helps in understanding the vibrational effects in the lattice. Below θ_D, vibrations exist in the lattice due to the dominance of quantum effects while above θ_D, these effects are less significant. *Figure 5.6(a-d)* conveys temperature and pressure effects on θ_D, which display a leisurely reduction in the value of θ_D as T increases and a significant increase as P increases at constant values of pressure and temperature, respectively, for $RbSnX_3$. At 300 K and zero pressure, the values of θ_D for $RbSnF_3$, $RbSnCl_3$, $RbSnBr_3$, and $RbSnI_3$ are 235.58, 173.5, 137.01 and 109.53 K, respectively. It has values of 187.95 K ($RbSnF_3$), 134.01 K ($RbSnCl_3$), 102.23 K ($RbSnBr_3$) and 79.02 K ($RbSnI_3$) at (1200 K and 0 GPa). The reported values of θ_D decrease with increasing ionic radius of the halide present in the considered compound. These values are in synchronous with the value obtained from the mechanical method.

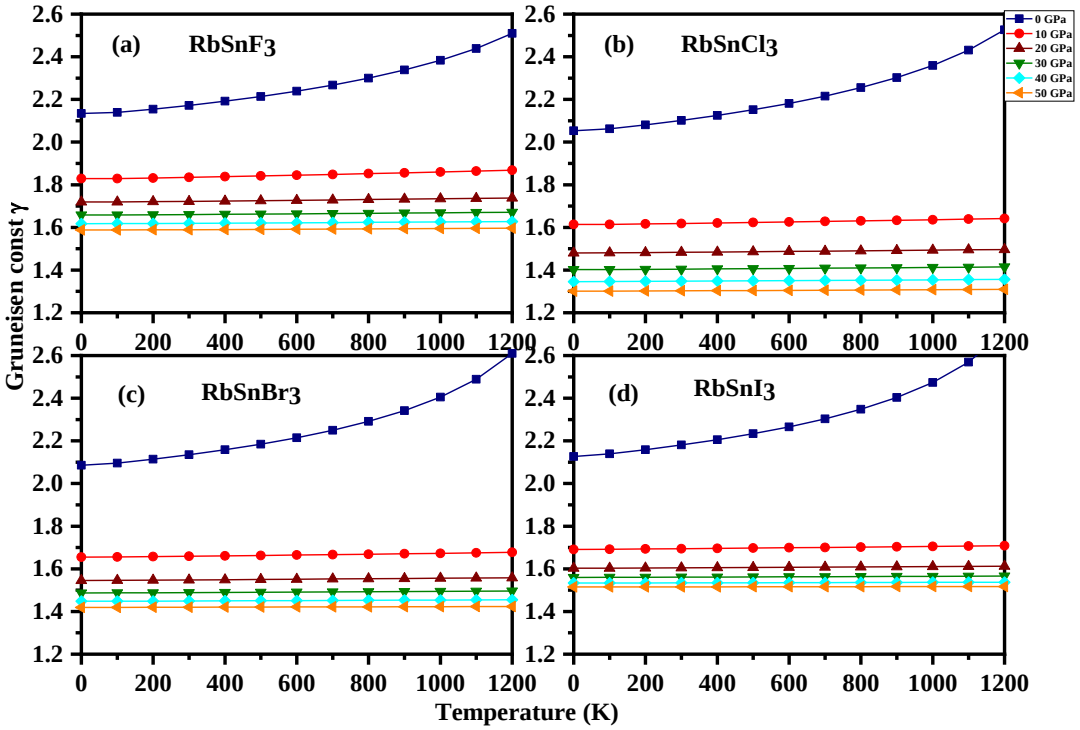

Figure 5.7: Gr*ü*neisen constant plot versus temperature for the constant value of pressures for $RbSnX_3$ (X=F, Cl, Br, and I) perovskite

The nature of Grüneisen constant (γ) is understood by illustrating its variation with *T* and *P* in *Figure 5.7(a-d)* for RSX compounds. When a material is exposed to higher *T* and *P* values, this parameter shows how the vibrational frequency changes. As a result, the dynamics of the crystal are altered. *Figure 5.7* describes a slow increment in the value of γ when temperature changes from 0 to 1200 K at constant values of pressures, i.e., 0, 10, 20, 30, 40, and 50 GPa. We found Grüneisen constant reduces rapidly as pressure increases for constant values of temperatures. The pressure's effect is found to be more significant as compared to the temperature on RSX perovskites. Grüneisen constant obtained at zero *T* and *P* for $RbSnF_3$, $RbSnCl_3$, $RbSnBr_3$ and $RbSnBr_3$ are 2.13, 2.05, 2.08 and 2.12, respectively.

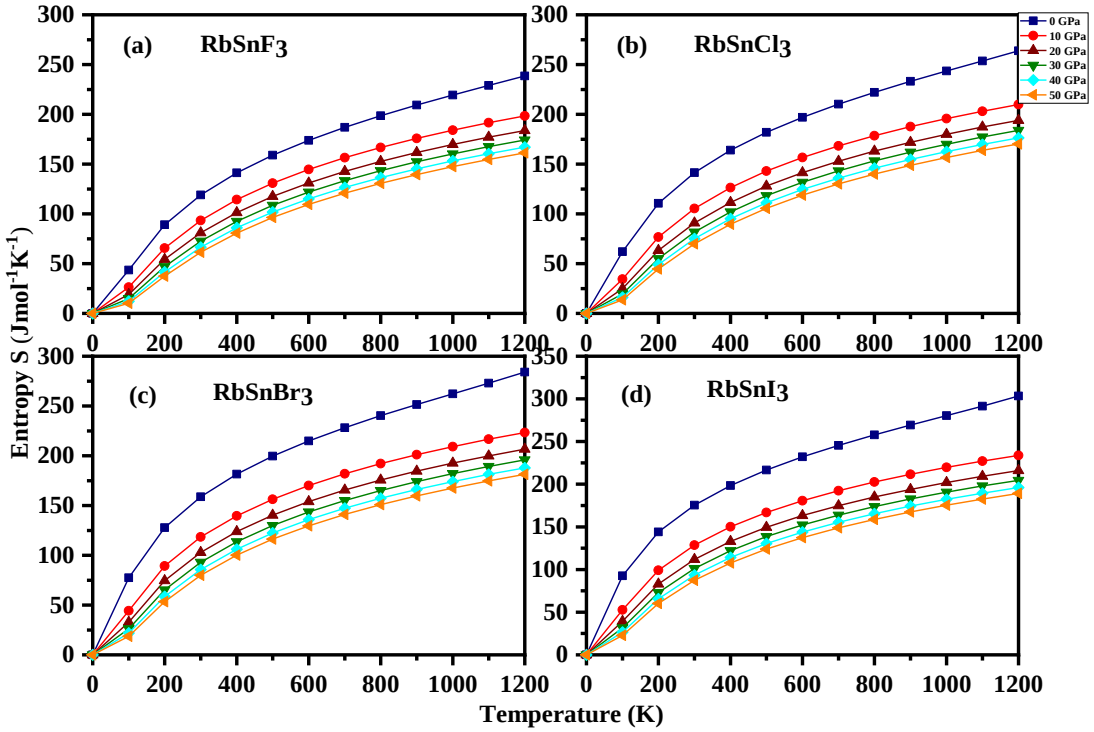

Figure 5.8: Entropy plot versus temperature for the constant value of pressures for $RbSnX_3$ (X=F, Cl, Br, and I) perovskite

Further, entropy (*S*) represents the uncertainty and disorder insight of the system. The degree of disorder or disturbance within the substance can be understood by studying the changes that occurred due to temperature and pressure. Plot of *S* with *T* (0-1200 K) and P (0-50 GPa) is presented in *Figure 5.8(a-d)* for $RbSnF_3$, $RbSnCl_3$, $RbSnBr_3$ and $RbSnI_3$ perovskites. *Figure 5.8(a-d)* represents that entropy is zero at zero kelvin and zero pressure. *S* increases exponentially with *T*, implying that at higher temperatures, disturbance within the material increases at constant pressure while decreasing with pressure, implying that the material becomes more ordered at higher pressure. Temperature uses to increase the thermal vibrations while pressure tries to seize these vibrations. In the graph between entropy and temperature, we didn't find discontinuity in the value of entropy which represents single phase transition. We have reported entropy values as 119, 141, 159 and 175 J/(mol K) at 0 GPa and 300 K for $RbSnF_3$, $RbSnCl_3$, $RbSnBr_3$ and $RbSnI_3$ perovskites, respectively.

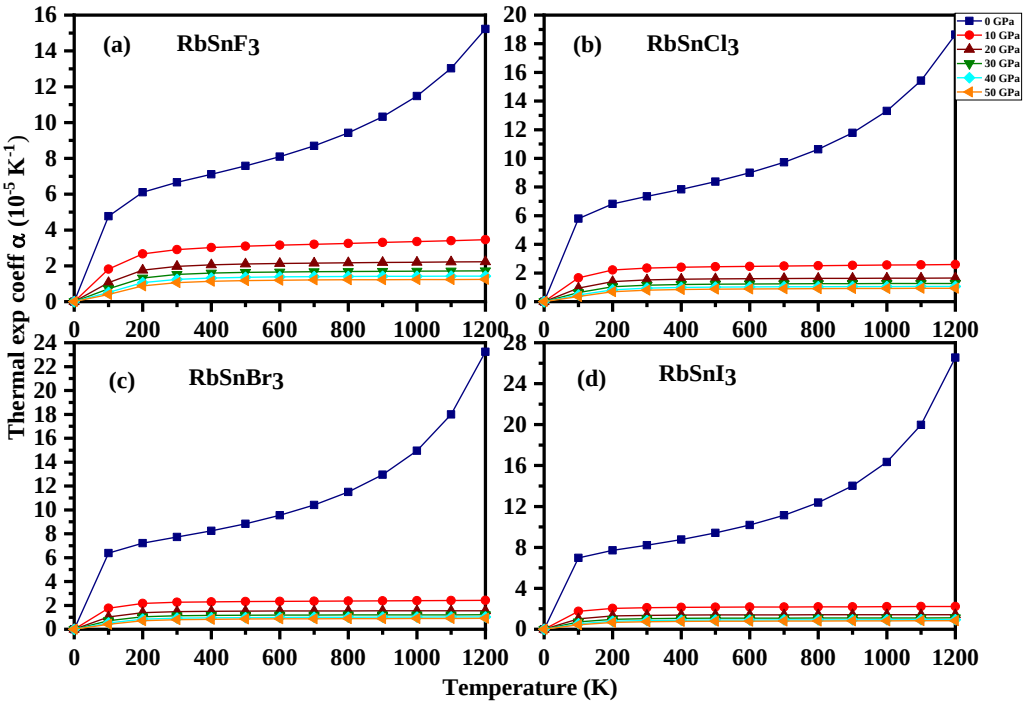

Figure 5.9: Thermal expansion coefficient plot versus temperature for the constant value of pressures for $RbSnX_3$ (X=F, Cl, Br, and I) perovskite

Furthermore, volumetric thermal expansion coefficient α plots with T and P are presented in *Figure 5.9(a-d)*. It elucidates that on applying heat, the substances expand in all directions due to the motion of the constituent particles within the substances. We can interpret from the graphs that the values of α increase swiftly till 100 K and beyond that, an idle increase is seen. The observed values of α at 300K and 0 GPa are 6.66, 7.35, 7.72 and 8.22 (10^{-5}/K) for $RbSnF_3$, $RbSnCl_3$, $RbSnBr_3$ and $RbSnI_3$, respectively. With pressure, their values have shown the opposite effect to that of temperature. A continuous decrease in the α is observed with changes in P at a constant value of T. The lowest pressure side yields the highest value of α. α also helps in understanding the bonding in the solids; the larger value of α means the bond is weaker while a smaller value means the bond is stronger. This work explores the systematic learning of the thermal properties of $RbSnX_3$ perovskites that opens its scope for further study in experimentation.

5.3.5 Thermoelectric Properties

We have determined a variety of thermoelectric (TE) parameters to determine the material's suitability for thermoelectric applications. For this, we have used the mBJ-

DFT method with semi-classical Boltzmann theory [48, 49], which is ingrained in Boltztrap code [52] via the WIEN2K code, using 50,000 *K* points. The majority of spins are near the Fermi level (E_F); therefore, effective studies for thermoelectric properties are in the vicinity of the E_F. Around $3/5^{th}$ of energy across the world is unused as waste heat [75]. Thermoelectric materials can be an alternative source of energy owing to their capability of changing waste thermal energy into electricity and vice-versa [76, 77]. In this context, we have worked on the TE properties for evaluating the Seebeck coefficient ($\mathcal{S}$), electrical conductivity (σ), thermal conductivity (κ), power factor (*PF*), and figure of merit (*ZT*). The performance of TE materials depends upon these parameters. The best thermoelectric material for the conversion of thermal energy into electrical energy should have lower κ and higher σ and their resultant formula clubbed into *ZT* which is described as follows:

$$\mathrm{ZT} = \frac{\mathcal{S}^2\sigma}{\kappa}\mathrm{T} \tag{5.1}$$

The term in the denominator is thermal conductivity comprises of electronic (κ_e) as well as lattice (κ_l) conductivities. For practical use of materials for TE applications, the values of ZT should be equal to or more than unity. κ_e is evaluated through the BoltzTrap code and κ_l through the Slack model [79]. A high *ZT* contributes to an extremely low κ_l. Slack provides the model to find out the κ_l using θ_D and γ.

$$\kappa_l = \frac{0.849 \times 3\sqrt[3]{4}}{20\pi^3\left(1 - \frac{0.514}{\gamma} + \frac{0.228}{\gamma^2}\right)}\left(\frac{K_B\theta_D}{\hbar}\right)^3 \frac{\overline{M}\,\delta}{\gamma^2 T n^{\frac{2}{3}}} \tag{5. 2}$$

$$\kappa_l = A_\gamma \frac{\overline{M}\,\delta{\theta_D}^3}{\gamma^2 T n^{\frac{2}{3}}} \tag{5. 3}$$

$$A_\gamma = \frac{2.43 \times 10^{-8}}{1 - \frac{0.514}{\gamma} + \frac{0.228}{\gamma^2}} \tag{5. 4}$$

Equations 5.4-5.6 [77-81] represent the formula for the estimation of κ_l (in $Wcm^{-1}K^{-1}$), which consists of $\overline{M}$, average atomic mass (in a.m.u), δ^3, volume per atom (in Å). A_γ is related to the Grüneisen parameter expressed in Eq. 5.6, given by Julian [79] and later modified by Leibfried and Schlomann [82].

Our motive is to find the lower value of κ_l, which further helps in the enhancement of the (ZT). Therefore, using BoltzTrap code, we have computed $\mathcal{S}$, σ/τ, κ_e/τ, PF ($\mathcal{S}^2\sigma/\tau$), where τ is the scattering relaxation time. In *Figures 5.10* to *5.11*, we show how they change with temperatures ranging from 50 to 1200 K. κ_l and ZT were evaluated through *equations 5.4* and *5.3*, respectively.

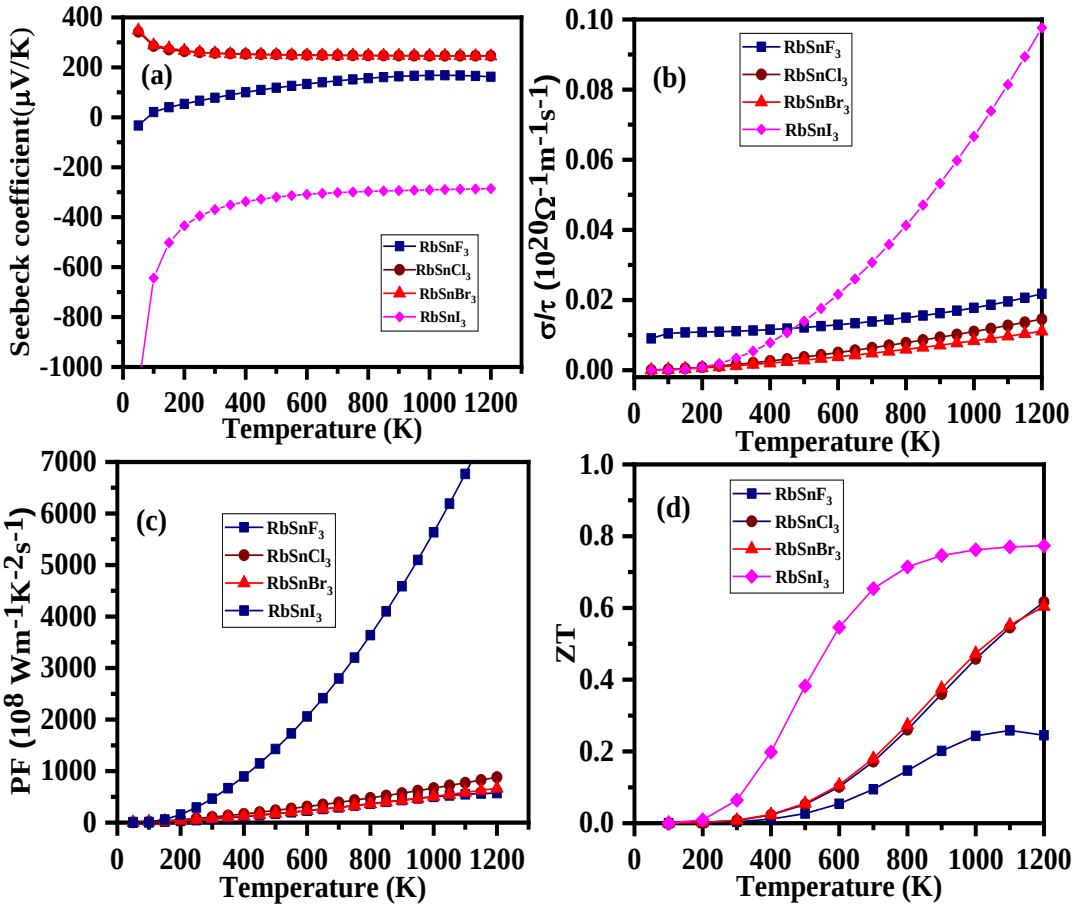

Figure 5.10: Variation of Seebeck Coefficient $\mathcal{S}$, Electrical thermal conductivity σ/τ, Power factor PF, Figure of merit ZT with respect to temperature T

Figure 5.10a is the plot of Seebeck coefficient ($\mathcal{S}$) vs Temperature from 50 to1200 K, which elucidates that the Seebeck coefficient (thermopower) for $RbSnCl_3$ and $RbSnBr_3$ decreases with T and is positive in the entire range. This represents p-type conduction, and hence, holes are the majority of charge carriers. Its value decreases from 342 μV/K at 50 K to 246 μV/K at 1200 K for $RbSnCl_3$ and decreases from 348 μV/K at 50 K to 245 μV/K at 1200 K for $RbSnBr_3$. The value of $\mathcal{S}$ becomes constant for higher values of temperature. The plot of $\mathcal{S}$ vs T for $RbSnF_3$ shows their variation to be directly proportional to each other. Its value varies from -33.2 μV/K at 50 K to

162 μV/K at 1200 K. Below 100 K, the value of the charge carrier is negative and after 100 K, it becomes positive. That is, $RbSnF_3$ has both n- and p-type conduction and has both holes and electrons as charge carriers. S for $RbSnI_3$ shows a negative value in the entire range of temperature. The values of S are about -350 μV/K at 300 K. The larger value of Seebeck coefficient is a fact of semiconductor materials.

Figure 5.10b depicts an analysis of the electrical conductivity (σ/τ) of $RbSnX_3$ perovskites over a temperature range of 50-1200 K. We interpret that σ/τ increases linearly with T but a sharp rise is observed in $RbSnI_3$. Electrical conductivity σ/τ for ($RbSnF_3$, $RbSnCl_3$, $RbSnBr_3$, $RbSnI_3$) increases from (9.06, 0.044, 0.032, 0.03) 10^{17} $\Omega^{-1}m^{-1}s^{-1}$ at 50 K to (21.79, 14.55, 11.1, 97) 10^{17} $\Omega^{-1}m^{-1}s^{-1}$ at 1200 K. Large variation in electrical conductivity is observed in case of $RbSnI_3$. This means conduction of free charge carriers rises with the rise in temperature due to an increase in the kinetic energy of the charge carriers. All the considered perovskites show an enhancement in electrical conductivity.

The power factor (*PF*) is an indicator of the capable use of power and can be calculated by incorporating the $\mathcal{S}$ and σ/τ as $\mathcal{S}^2\sigma/\tau$. Therefore, we have calculated PF and presented its variation w.r.t temperature for $RbSnX_3$ (X = F, Cl, Br, and I) in *Figure 5.10c*. Its value increases linearly for all the considered compounds. But we found that the value of the *PF* for $RbSnF_3$ is linearly increased till 1000 K, beyond that the increase is sluggish. In case of $RbSnI_3$ rise in *PF* is quite sharp compared to other Rb compounds. The values of *PF* at room temperature for $RbSnF_3$, $RbSnCl_3$, $RbSnBr_3$ and $RbSnI_3$ are 68.5, 108.2, 82.9 and 465.1 (10^8 $Wm^{-1}K^{-2}s^{-1}$), respectively.

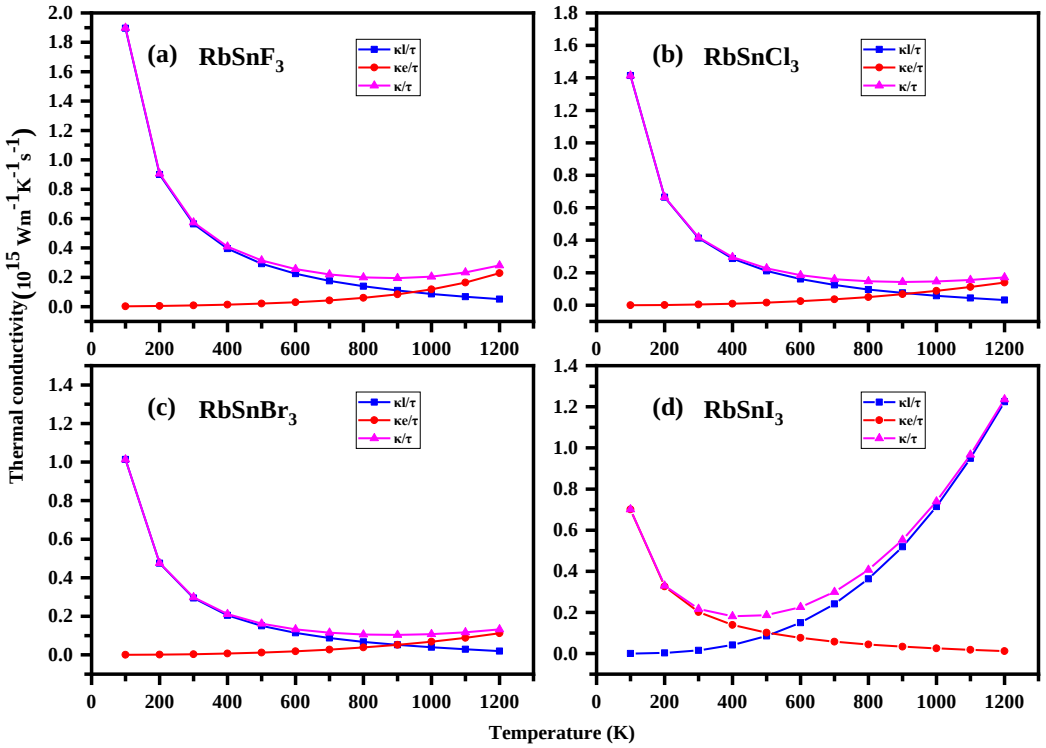

Figure 5.11: Total κ/τ, Lattice $\frac{\kappa_l}{\tau}$ and electronic $\frac{\kappa_e}{\tau}$ Thermal conductivity variation with respect to temperature

To approach the higher value of *ZT* for the materials, a low value of κ is required. To estimate the thermal conductivity of the materials, the role of electrons and vibrations of a lattice is equally important. We have therefore estimated electronic κ_e/τ and lattice κ_l/τ thermal conductivities. *Figure 5.11(a, b, c, d)* shows a plot of the electronic κ_e/τ, lattice κ_l/τ, and total κ/τ thermal conductivities for $RbSnF_3$, $RbSnCl_3$, $RbSnBr_3$ and $RbSnI_3$ with temperature (50 K to 1200 K), respectively. The calculated thermal conductivities (κ_l/τ, κ_e/τ, κ/τ) at the maximum considered temperature (1200 K) for $RbSnF_3$, $RbSnCl_3$, $RbSnBr_3$ and $RbSnI_3$ are (0.052, 0.229, 0.280), (0.032, 0.140, 0.172), (0.019, 0.112, 0.132) and (1.224, 0.011, 1.23) (in 10^{15} $Wm^{-1}K^{-1}s^{-1}$), respectively. In case of $RbSnX_3$ (X= F, Cl, and Br), Lattice thermal conductivity decrease with temperature, while electronic thermal conductivity increases with temperature. While reverse is observed in $RbSnI_3$ perovskite. The major contribution to heat conduction is due to lattice vibrations. This trend justifies the behavior of semiconductors during thermal conduction.

As stated in the mathematical expression for *ZT* provided in *Eq.5.3*, the *ZT* is assessed utilizing both lattice and electrical thermal conductivities. *Figure 5.11d* shows the *ZT* fluctuation with temperature for $RbSnX_3$ (where X=F, Cl, Br, and I). We perceive the value of *ZT* is almost 0 till 300 K for $RbSnCl_3$, $RbSnBr_3$ and 200 K for $RbSnI_3$ and beyond that, it increases linearly with temperature. For $RbSnF_3$, *ZT* is almost 0 till 400 K and it increases linearly in the range 400-1100 K and decreases afterward. The maximum value of *ZT* is obtained as 0.26 (1100 K), 0.62 (1200 K), 0.60 (1200 K), and 0.77 (1200 K) for $RbSnF_3$, $RbSnCl_3$, $RbSnBr_3$, and $RbSnI_3$, respectively. This data can be used as a reference for forthcoming theoretical and experimental procedures and the design of novel thermoelectric devices.

5.4 SUMMARY AND CONCLUSION

Finally, the requirement of the technological applications in context of the materials' performances in study of thermoelectric, mechanical and thermodynamic is concluded here. We have systematically explained Rb-Sn-based perovskites using a computational quantum mechanical technique via DFT. The electronic structures of RSX compounds reveal that considered compounds are non-magnetic and semiconducting. Further, in mechanical context, three cubic elastic constants have been calculated and their bulk moduli are reported to be 44.6, 21.61, 20.29, and 15.20 GPa, respectively. The considered materials are successful in fulfilling the criteria of mechanical stability. On thermodynamic background, the considered materials have been tested for their performances on thermal expansion coefficient, Debye temperature, unit cell volume, entropy, and their variation w.r.t temperature and pressure. Furthermore, surprisingly, $RbSnI_3$, $RbSnCl_3$ and $RbSnBr_3$ exhibit enhanced figure of merit values as 0.77, 0.62 and 0.60, respectively at 1200 K for their application in thermoelectric devices. The present study opens a scope to work experimentally and suggests materials' technological application in thermoelectric devices.

REFERENCES

1. Hafez, A.M., Zedan, A.F., Alqaradawi, S.Y., Salem, N.M. and Allam, N.K. "Computational study on oxynitride perovskites for CO_2 photoreduction." *Energy Conversion and Management* 122 (2016): 207-214.
2. Singh, S., and Sudhir K.P. "Understanding the thermoelectric properties of $LaCoO_3$ compound." *Philosophical Magazine* 97, no. 6 (2017): 451-463.
3. Reshak, A.H. "Fe_2MnSi_x Ge_{1-x}: influence thermoelectric properties of varying the germanium content." *Rsc Advances* 4, no. 74 (2014): 39565-39571.
4. Khanday, W.A., Kabir, G. and Hameed, B.H. "Catalytic pyrolysis of oil palm mesocarp fibre on a zeolite derived from low-cost oil palm ash." *Energy Conversion and Management* 127 (2016): 265-272.
5. Yin, W.J., Yang, J.H., Kang, J., Yan, Y. and Wei, S.H. "Halide perovskite materials for solar cells: a theoretical review." *Journal of Materials Chemistry A* 3, no. 17 (2015): 8926-8942.
6. Jena, A.K., Kulkarni, A. and Miyasaka, T. “Halide perovskite photovoltaics: background, status, and future prospects.” *Chemical reviews* 119, no. 5 (2019): 3036-103.
7. Kojima, A., Teshima, K., Shirai, Y. and Miyasaka, T. “Organometal halide perovskites as visible-light sensitizers for photovoltaic cells.” *Journal of the American Chemical Society* 131, no.17 (2009): 6050-1.
8. Huang, H., Polavarapu, L., Sichert, J.A., Susha, A.S., Urban, A.S., and Rogach, A.L. “Colloidal lead halide perovskite nanocrystals: synthesis, optical properties and applications NPG.” *Asia Materials* 8, no.11 (2016**):** e328.
9. Ray, N., and Waghmare, U.V. "Coupling between magnetic ordering and structural instabilities in perovskite biferroics: a first-principles study." *Physical Review B* 77, no. 13 (2008): 134112.
10. Inoue, J., and Maekawa, S. "Spiral state and giant magnetoresistance in perovskite Mn oxides." *Physical Review Letters* 74, no. 17 (1995): 3407.
11. Balamurugan, S., Yamaura, K., Karki, A. B., Young, D. P., Arai, M., and Takayama-Muromachi, E. "Specific-heat evidence of strong electron correlations and thermoelectric properties of the ferromagnetic perovskite $SrCoO_{3-\delta}$." *Physical Review B* 74, no. 17 (2006): 172406.

12. Fu, P., Wei, Q., Bai, S., Yang, D., Chen, L., Guo, X., and Li, C. "Integrating large-area perovskite solar module with thermoelectric generator for enhanced and stable power output." *Nano Energy* 65 (2019): 104009.
13. Ramirez, A. P. "Colossal magnetoresistance." *Journal of Physics: Condensed Matter* 9, no. 39 (1997): 8171.
14. Wang, J., Zhang, C., Liu, H., et al. “Spin-optoelectronic devices based on hybrid organic-inorganic trihalide perovskites.” *Nature Communications* 10, no.1 (2019):129.
15. Kulkarni, A., Ciacchi, F.T., Giddey, S., et al. “Mixed ionic electronic conducting perovskite anode for direct carbon fuel cells.” *Int J Hydrog Energy* 37, no. 24 (2012): 19092-19102.
16. Park, N-G. “Perovskite solar cells: an emerging photovoltaic technology.” *Materials Today* 18, no. 2 (2015): 65-72.
17. Chen, Y., Zhang, L., Zhang, Y., Gao, H., Yan, H. “Large-area perovskite solar cells-a review of recent progress and issues.” *RSC Advances* 8, no. 19 (2018): 10489-10508.
18. Li, B., Hui, W., Ran, X., Xia, Y., Xia, F., Chao, L., Chen, Y., and Huang, W. "Metal halide perovskites for resistive switching memory devices and artificial synapses." *Journal of Materials Chemistry C* 7, no. 25 (2019): 7476-7493.
19. Yoo, E.J., Lyu, M., Yun, J.H., Kang, C. J., Choi, Y.J. and Wang, L. "Resistive switching behavior in organic–inorganic hybrid $CH_3NH_3PbI_{3-x}Cl_x$ perovskite for resistive random access memory devices." *Advanced Materials* 27, no. 40 (2015): 6170-6175.
20. Hwang, B., and Lee J.S. "Recent advances in memory devices with hybrid materials." *Advanced electronic materials* 5, no. 1 (2019): 1800519.
21. Wang, H., Pei, Y., LaLonde, A.D., Snyder, G.J. “Heavily doped p-type PbSe with high thermoelectric performance: an alternative for PbTe.” *Adv Mater* 23, no. 11 (2011): 1366-1370.
22. Mao, X., Sun, L., Wu, T., Chu, T., Deng, W. and Han, K. "First-principles screening of all-inorganic lead-free ABX_3 perovskites." *The Journal of Physical Chemistry C* 122, no. 14 (2018): 7670-7675.

23. Gou, G., Young, J., Liu, X. and Rondinelli, J.M. “Interplay of Cation Ordering and Ferroelectricity in Perovskite Tin Iodides: Designing a Polar Halide Perovskite for Photovoltaic Applications.” *Inorganic Chemistry*, 56, no. 1 ((2016): 26-32.
24. Jung, Young-Kwang, Ji-Hwan Lee, Aron Walsh, and Aloysius Soon. "Influence of Rb/Cs cation-exchange on inorganic Sn halide perovskites: from chemical structure to physical properties." Chemistry of Materials 29, no. 7 (2017): 3181-3188.
25. Li, Y., Xu, G., Zhang, P., and Shao, X. "Structural, electronic and optical properties of $RbSnCl_3$: A first-principles calculation." *Chemical Physics Letters* 716 (2019): 76-82.
26. Jiang, J., Onwudinanti, C.K., Hatton, R.A., Bobbert, P.A. and Tao, S. “Stabilizing Lead-Free All-Inorganic Tin Halide Perovskites by Ion Exchange.” *The Journal of Physical Chemistry C* 122, no. 31 (2018): 17660-17667.
27. Rai, D.P., Shankar, A., Ghimire, M.P., Khenata, R., Omran, S.B., Syrotyuk, S.V., and Thapa, R.K. "Investigation of the structural, electronic and optical properties of the cubic $RbMF_3$ perovskites (M= Be, Mg, Ca, Sr and Ba) using modified Becke-Johnson exchange potential." *Materials Chemistry and Physics* 192 (2017): 282-290.
28. Khan, I., Shehzad, N., Ahmad, I., Ali, Z., & Jalali-Asadabadi, S. “First-principle studies of the optoelectronic properties of $ASnF_3$ (A = Na, K, Rb and Cs).” *International Journal of Modern Physics B* 31, no. 21 (2017): 1750148.
29. Khan, K., Sahariya, J. and Soni, A. “Structural, electronic and optical modeling of perovskite solar materials $ASnX_3$ (A= Rb, K; X= Cl, Br): First principle investigations.” *Materials Chemistry and Physics* 262 (2021): 124284.
30. Al-Qaisi, S., Mushtaq, M., Alomairy, S., Vu, T.V., Rached, H., Haq, B.U., Mahmood, Q. and Al-Buriahi, M.S. "First-principles investigations of Na_2CuMCl_6 (M= Bi, Sb) double perovskite semiconductors: Materials for green technology." *Materials Science in Semiconductor Processing* 150 (2022): 106947.
31. Bourachid, I., Caid, M., Cheref, O., Rached, D., Heireche, H., Abidri, B., Rached, H., and Benkhettou, N. "Insight into the structural, electronic, mechanical and

optical properties of inorganic lead bromide perovskite $APbBr_3$ (A= Li, Na, K, Rb, and Cs)." *Computational Condensed Matter* 24 (2020): e00478.

32. Hocine, K., Cheref, O., Bettine, K., Rached, D., Benalia, S., Rabah, M., Benkhettou, N., and Rached, H. "The structural, electronic, optical and thermo-electric properties of oxynitride perovskite $CaTaO_2N$." *In Spin*, vol. 10, no. 01, p. 2050007. World Scientific Publishing Company, 2020.
33. Benmhidi, H., Rached, H., Rached, D., and Benkabou, M. "Ab initio study of electronic structure, elastic and transport properties of fluoroperovskite $LiBeF_3$." *Journal of Electronic Materials* 46, no. 4 (2017): 2205-2210.
34. Rached, H., Rached, D., Rabah, M., Khenata, R. and Reshak, A.H. "Full-potential calculation of the structural, elastic, electronic and magnetic properties of $XFeO_3$ (X= Sr and Ba) perovskite." *Physica B: Condensed Matter* 405, no. 17 (2010): 3515-3519.
35. Rached, H., Bendaoudia, S., and Rached, D. "Investigation of Iron-based double perovskite oxides on the magnetic phase stability, mechanical, electronic and optical properties via first-principles calculation." *Materials Chemistry and Physics* 193 (2017): 453-469.
36. Sholl, D. and Steckel, J.A. “Density functional theory: a practical introduction” (John Wiley & Sons, Hoboken, New Jersey) (2011).
37. Perdew, J.P., Burke, K., and Ernzerhof, M. "Generalized gradient approximation made simple." *Physical Review Letters* 77, no. 18 (1996): 3865.
38. Wu, Z., and Cohen, R. E. “More accurate gradient approximation for solids”, *Phys. Rev. B* 73, 235116 (2006).
39. Csonka, G.I., Ruzsinszky, A., Perdew, J.P. and Grimme, S. "Improved description of stereoelectronic effects in hydrocarbons using semilocal density functional theory." *Journal of Chemical Theory and Computation* 4, no. 6 (2008): 888-891.
40. Birch, F. "The effect of pressure upon the elastic parameters of isotropic solids, according to Murnaghan's theory of finite strain." *Journal of Applied Physics* 9, no. 4 (1938): 279-288.

41. Tran, F. and Blaha, P. “Accurate band gaps of semiconductors and insulators with a semilocal exchange-correlation potential.” *Physical review letters* 102, no. 22 (2009): 226401.
42. Blaha, P., Schwarz, K., Tran, F., Laskowski, R., Madsen, G.K. and Marks, L.D. "WIEN2k: An APW+ lo program for calculating the properties of solids." The Journal of Chemical Physics 152, no. 7 (2020): 074101.
43. Monkhorst, H.J., and Pack J.D. “Special points for Brillouin-zone integrations.” *Physical review B* 13, no. 12 (1976): 5188.
44. Jamal, M., Asadabadi, S.J., Ahmad, I. and Aliabad, H.R. "Elastic constants of cubic crystals." *Computational Materials Science* 95 (2014): 592-599.
45. Blanco, M.A., Francisco, E. and Luana, V., 2004. "GIBBS: isothermal-isobaric thermodynamics of solids from energy curves using a quasi-harmonic Debye model." *Computer Physics Communications* 158, no. 1 (2004): 57-72.
46. Otero-de-la-Roza, A., Abbasi-Pérez, D. and Luaña, V. "Gibbs2: A new version of the quasiharmonic model code. II. Models for solid-state thermodynamics, features and implementation." *Computer Physics Communications* 182, no. 10 (2011): 2232-2248.
47. Otero-de-la-Roza, Alberto, and Luaña, V. "Gibbs2: A new version of the quasi-harmonic model code. I. Robust treatment of the static data." *Computer Physics Communications* 182, no. 8 (2011): 1708-1720.
48. Allen, P. “Boltzmann theory and resistivity of metals.” Kluwer International Series in Engineering and Computer Science. 1996: 219-250.
49. Ziman, J.M. “Electrons and phonons: the theory of transport phenomena in solids.” *Oxford university press* 2001.
50. Hurd, C. “The Hall Effect in Metals and Alloys.” *Plenum Press*. 1972.
51. Madsen, G.K.H., Singh, D.J. “BoltzTraP. A code for calculating band-structure dependent quantities.” *Computer Physics Communications* 175, no. 1 (2006): 67-71.
52. Madsen, G.K.H., Carrete, J., and Verstraete, M.J. "BoltzTraP2, a program for interpolating band structures and calculating semi-classical transport coefficients." *Computer Physics Communications* 231 (2018): 140-145.

53. Jain, D., Chaube, S., Khullar, P., Srinivasan, S.G., and Rai, B. "Bulk and surface DFT investigations of inorganic halide perovskites screened using machine learning and materials property databases." *Physical Chemistry Chemical Physics* 21, no. 35 (2019): 19423-19436.
54. Rahman, M.H., Jubair, M., Rahaman, M.Z., Ahasan, M.S., Ostrikov, K.K. and Roknuzzaman, M., 2022. $RbSnX_3$ (X= Cl, Br, I): promising lead-free metal halide perovskites for photovoltaics and optoelectronics. *RSC Advances*, 12(12), pp.7497-7505
55. Ubic, R. "Revised method for the prediction of lattice constants in cubic and pseudocubic perovskites." *Journal of the American Ceramic Society* 90, no. 10 (2007): 3326-3330.
56. Li, C., Lu, X., Ding, W., Feng, L., Gao, Y. and Guo, Z. "Formability of abx_3 (x= F, Cl, Br, I) halide perovskites." *Acta Crystallographica Section B: Structural Science* 64, no. 6 (2008): 702-707.
57. Giorgi, G., and Yamashita, K. eds. "Theoretical Modeling of Organohalide Perovskites for Photovoltaic Applications." *CRC Press* (2017).
58. Miao, M.S., Botana, J., Zurek, E., Hu, T., Liu, J. and Yang, W. "Electron counting and a large family of two-dimensional semiconductors." *Chemistry of Materials* 28, no. 7 (2016): 1994-1999.
59. Benyahia, J., Bouchikhi, S. and Bekhechi, S. "First principle calculations of phases stability and electronic structure of the trihalide perovskite $RbSnBr_3$." *Phy Sci Biophy J* 3 (2019): 1-6.
60. Körbel, S., Marques, M.A. and Botti, S. "Stability and electronic properties of new inorganic perovskites from high-throughput ab initio calculations." *Journal of Materials Chemistry C* 4, no. 15 (2016): 3157-3167.
61. Bhat, T.M. and Gupta, D.C. "Robust thermoelectric performance and high spin polarisation in CoMnTiAl and FeMnTiAl compounds." *RSC Advances* 6, no. 83 (2016): 80302-80309.
62. Sin'Ko, G.V., and Smirnov, N.A. "Ab initio calculations of elastic constants and thermodynamic properties of bcc, fcc, and hcp Al crystals under pressure." *Journal of Physics: Condensed Matter* 14, no. 29 (2002): 6989.

63. Mehl, M.J., Klein, B.M. and Papaconstantopoulos, D.A. "Intermetallic compounds: principle and practice." *Principles* 1 (1995): 195-210.
64. Voigt, W. "Lehrbuch der Kristallphysik (Textbook of crystal physics)." *BG Teubner, Leipzig und Berlin* (1928).
65. Schreiber, E., Anderson, O.L., Soga, N. and Bell, J.F. "Elastic constants and their measurement." (1975): 747-748.
66. Hill, R. "The elastic behaviour of a crystalline aggregate." *Proceedings of the Physical Society. Section A* 65, no. 5 (1952): 349.
67. Reuss, A.J.Z.A.M.M. "Calculation of the flow limits of mixed crystals on the basis of the plasticity of monocrystals." *Z. Angew. Math. Mech* 9 (1929): 49-58.
68. Dar, S.A., Srivastava, V., Sakalle, U.K., and Parey. V. "Ferromagnetic Phase Stability, Magnetic, Electronic, Elasto-Mechanical and Thermodynamic Properties of $BaCmO_3$ Perovskite Oxide." *Journal of Electronic Materials* 47, no. 7 (2018): 3809-3816.
69. Mayer, B., Anton, H., Bott, E., Methfessel, M., Sticht, J., Harris, J. and Schmidt, P. C. "Ab-initio calculation of the elastic constants and thermal expansion coefficients of Laves phases." *Intermetallics* 11, no. 1 (2003): 23-32
70. Haines, J., Leger, J. M. and Bocquillon, G. "Synthesis and design of superhard materials." *Annual Review of Materials Research* 31, no. 1 (2001): 1-23.
71. Pugh, S. F. "XCII. Relations between the elastic moduli and the plastic properties of polycrystalline pure metals." *The London, Edinburgh, and Dublin Philosophical Magazine and Journal of Science* 45, no. 367 (1954): 823-843.
72. Liu, Xing, Jia Fu, and Guangming Chen. "First-principles calculations of electronic structure and optical and elastic properties of the novel ABX_3-type $LaWN_3$ perovskite structure." RSC Advances 10, no. 29 (2020): 17317-17326.
73. Bouldiab, Y., S. Terkhi, Z. Aziz, F. Bendahma, M. A. Bennani, R. Bentata, and M. A. Boudjeltia. "DFT study of structural, elastic, electronic, magnetic, thermal and transport properties of new multifunctional NiVSn half-Heusler for spintronic and thermoelectric applications." International Journal of Modern Physics B 35, no. 19 (2021): 2150202.
74. Slater, J. C. "Introduction to Chemical Physics." (McGraw-Hill Book Company) (1939).

75. Petit, A.T., Dulong, P.L. “Study on the measurement of specific heat of solids.” *Ann Chim Phys* 10 (1819):395.
76. Forman, C., Muritala, I.K., Pardemann, R. and Meyer, B. "Estimating the global waste heat potential." *Renewable and Sustainable Energy Reviews* 57 (2016): 1568-1579.
77. Pei, Y., Wang, H., Snyder, G.J. “Band engineering of thermoelectric materials.” *Adv Mater* 24, no. 46 (2012): 6125-6135.
78. Pei, Y., Wang, H., Gibbs, Z.M., LaLonde, A.D., Snyder, G.J. “Thermopower enhancement in $Pb_{1-x}Mn_xTe$ alloys and its effect on thermoelectric efficiency.” *NPG Asia Mater* 4, no. 9 (2012): e28-e28.
79. Morelli, D.T., Slack, G.A. “High lattice thermal conductivity solids. High Thermal Conductivity Materials.” *New York: Springer* (2006):37-68.
80. Julian, C.L. “Theory of heat conduction in rare-gas crystals.” *Phys Rev* 137, no. 1A (1965): A128.
81. Bjerg, L., Iversen, B.B., Madsen, G.K.H. “Modeling the thermal conductivities of the zinc antimonides ZnSb and Zn_4Sb_3.” *Phys Rev B* 89, no. 2 (2014): 024304.
82. Leibfried, G. and Schlömann, E. Nachr. Akad. Wiss. Göttingen II a (4), 71 (1954).

CHAPTER 6

SUMMARY AND FUTURE SCOPE

6.1 SUMMARY

The thesis entitled "**First principles calculations on diverse properties of some Perovskite compounds**" presents the inclusive information about the structural, electronic, elastic, mechanical, thermodynamic and thermoelectric properties of $XCeO_3$ (X=Mg, Ca, Sr, Ba), $RFeO_3$ (R=Nd, Pr) and $RbSnX_3$ (X=F, Cl, Br, I) by implication of density functional theory. Certain approximations such as LDA, GGA-PBE, PBEsol, WC and mBJ (as exchange potential/function, XC) have been implemented to calculated aforesaid properties with more accuracy. WIEN2K package, based on FORTAN90 and FPLAPW as basis set are unified together for calculations. We have investigated the total of 10 perovskite compounds which include oxide as well as halide. The whole of the thesis is partitioned into six chapters.

Chapter one began with a general introduction and some information on the Perovskite structure and its numerous types. Also explored are perovskite uses in solar cells, TEGs, and spintronics. In addition, a review of the literature, the purpose and goal of the current project, and the driving force behind it are all discussed.

Chapter two covers density functional theory and exchange-correlation functions including LDA, GGA, and mBJ. Hubbard approximation LDA/GGA/mBJ+U is also included to consider correlated effects. For systems with lots of electrons, we have discussed various basis sets for solving the Schrödinger equation. Ab initio techniques to determine thermoelectric, elastic, mechanical, and thermodynamic properties are discussed.

Chapter three, four and five provides information regarding electrical, structural, elasto-mechanical, thermodynamic, and TE properties for Ce-based: $MgCeO_3$, $CaCeO_3$, $SrCeO_3$, $BaCeO_3$, Fe-based: $NdFeO_3$, $PrFeO_3$ and Rb-Sn-based: $RbSnCl_3$, $RbSnI_3$, $RbSnF_3$, and $RbSnBr_3$ perovskites, respectively.

To accomplish the objectives of the research work, firstly the structures of Ce, Fe and Rb-Sn based perovskites have been optimized under non-magnetic as well as ferromagnetic phase using different exchange potentials. Energy-volume curve analyse the stability of the structures and their corresponding data are fitted using Birch Murnaghan equation. With this analysis, we found that $XCeO_3$ (X=Mg, Ca, Sr, Ba) and $RbSnX_3$ (X=F, Cl, Br, I) are stable in non-magnetic phase while $RFeO_3$ (R=Nd, Pr) is stable in ferromagnetic phase. This means that for Fe based perovskites two electronic states behave differently. The value of formation energies shows all considered perovskites can be manufactured in laboratory under ambient conditions.

Second objective is about the study of electronic profile of these structures. In this regard, band structures, combined and partial density of states are examined. Electronic properties of $MgCeO_3$ (MCO), $CaCeO_3$ (CCO), $SrCeO_3$ (SCO), and $BaCeO_3$ (BCO) are evaluated using exchange corrleation LDA, PBE, PBEsol, mBJ. Electronic states of $XCeO_3$ show semi-conducting nature with band gap values in case of mBJ for MCO, CCO SCO, and BCO are 2.26 eV, 2.6, 2.56, and 2.4 eV, respectively. Similarly, electronic properties of $PrFeO_3$ (PFO) and $NdFeO_3$ (NFO) have been evaluated using GGA, mBJ, and mBJ+U potential. These materials have shown half-metallic behavior in mBJ+U potential i.e., showing metallic character in spin up while semiconductor in spin-down case with a bandgap of 2.0eV (PFO) and 1.8eV (NFO). The electronic structures of $RbSnF_3$ (RSF), $RbSnCl_3$ (RSC), $RbSnBr_3$ (RSB), $RbSnI_3$ (RSI) compounds reveal that considered compounds are semiconducting with the band gap values of RSF, RSC, RSB and RSI are 3.65, 1.5 eV, 0.65 eV, respectively.

Third objective includes mechanical and thermodynamic performances of the above said perovskites. The Quasi Harmonic Debye model is used for thermodynamic calculations and the IR elast package/ Thomas Charpin for elastic and mechanical calculations. The considered materials have been tested for their performances on unit cell volume, entropy, Debye temperature, thermal expansion coefficient, and their variation w.r.t temperature (0-1200 K) and pressure (0-50 GPa). Thermodynamic and mechanical stability are satisfied by all considered compounds.

Finally, the last objective for examination of thermoelectric parameters like Seebeck coefficient, thermal conductivity, the figure of merit, electrical conductivity, and power factor has been fulfilled using Boltztrap code based on semiclassical Boltzmann transport theory. Thermoelectric efficiency is found to increase with temperature. The compounds like RSI, BCO with higher value of figure of merit are significant for thermoelectric applications.

Finally, Chapter six summarize the entire work of the thesis, along with the future applications of the research work.

6.2 FUTURE SCOPE

The investigated materials in this thesis have shown remarkable properties which make them suitable for various applications. Thermoelectric applications such as thermoelectric power generators required a high value of the figure of merit. Investigated compounds such as Rb-Sn halide and Ce-based oxide family of perovskites have shown a high value of the figure of merit which makes them suitable for usage as thermoelectric material. Our research provides information that experimentalists can use to manufacture these compounds and use them in energy-related applications.

LIST OF PUBLICATIONS

1. Preeti Kumari, Vipul Srivastava, Rabah Khenata, Sajad Ahmad Dar, and Saleh H. Naqib. "A first-principles prediction of thermophysical and thermoelectric performances of $SrCeO_3$ perovskite." *International Journal of Energy Research* 46, no. 3 (2022): 2934-2946.
2. Preeti Kumari, Sajad Ahmad Dar, Ramesh Sharma, and Vipul Srivastava. "Quantum mechanical calculations on mechanical and elastic properties of cubic $SrCeO_3$ perovskite." *The European Physical Journal Plus* 137, no. 3 (2022): 313.
3. Preeti Kumari, Ramesh Sharma, Umesh Lilhore, Rabah Khenata, and Vipul Srivastava. "First-principles study on structural, electronic, elastic, mechanical, thermodynamic, and thermoelectric properties of $RbSnX_3$ (X= F, Cl, and Br) perovskites." *International Journal of Energy Research* 46, no. 15 (2022): 23893-23907.
4. Preeti Kumari, and Vipul Srivastava. "Study of Thermoelectrical Behavior of $BaXO_3$ Perovskites (X= Pu, Am, Cm)." In *Advances in Functional and Smart Materials: Select Proceedings of ICFMMP 2021*, pp. 143-154. Singapore: Springer Nature Singapore, 2022.
5. Preeti Kumari, Ramesh Sharma, Y. Al-Douri, Vipul Srivastava. “Electronic, thermodynamical and thermoelectric performances of $RbSnI_3$ halide perovskite for Photovoltaic cell and UV absorber applications, *Material Today Communications* 36 (2023): 106752.
6. Preeti Kumari, Ramesh Sharma, Vipul Srivastava. “Quantum mechanical calculations of opto-electronic, thermodynamic, and transport properties of $XCeO_3$ (X= Mg, Ca, and Ba) perovskite, *The Journal of Chemical Thermodynamics* 184 (2023): 107071.
7. Preeti Kumari and Vipul Sivastava. “DFT Calculations on Heat capacity and Debye temperature of Cs_2GeF_6 perovskite under high temperature and pressure” *AIP Conference Proceedings* 2800 (2023): 020315.
8. Preeti Kumari and Vipul Sivastava. “Abinitio Calculations of Structural, Electronic, and Thermodynamic Performance of Cs_2GeF_6 Perovskite” *AIP Conference Proceedings* 2800 (2023): 020010.

LIST OF COMMUNICATED PAPERS

1. Preeti Kumari, Ramesh Sharma, Vipul Srivastava. "Exploration of optoelectronic, thermophysical, and thermoelectric properties of $RFeO_3$ (R=Pr, Nd) perovskites", *Material Science and Engineering: B.*

LIST OF CONFERENCES

1. International Conference on "Emerging Trends in Science and Technology, ICETST-2021" held on 2-4 April 2021.
2. International Conference on "Recent advances in Fundamental and applied sciences, RAFAS 2021" held on 25-26 June 2021.
3. ICMET-2021 Conference on "International Conference on Materials Emerging Technologies-2021 (ICMET-21)" held on 18-19 Feb 2022.
4. 3rd International Conference on "Functional Materials, Manufacturing and Performances (ICFMMP-2022)" held on July29-30th, 2022.
5. IMURS-ICMAT 2023 11th International conference on Materials for Advanced Technologies, organized at Suntec City, Singapore, held on 26-30 June 2023.

LIST OF WORKSHOPS/WEBINARS

1. Karyashala (High-end Workshop) on "Renewable Energy: Production and Storage" held at IIT Ropar on 24-30Sep 2022.
2. Li-ion batteries and beyond: driving Next Generation Energy Storage with Mede Aheld on 19 Jan 2021.
3. IPR & Technology Transfer: IIC innovation Ambassador training series held on 16-17 January 2020.
4. Awareness Program to Introduce Giloy in Routine Life for The Promotion of Health" held on 26th March 2022.
5. IPA-Young Physicist Meet - 02, organized at Department of Physics, Panjab University held on 9-10 Dec 2022.